

Characterization of Nonlinearity Parameters in an Elastic Material with Quadratic Nonlinearity with a Complex Wave Field

A Thesis
Presented to
The Academic Faculty

by

Michael Rainer Braun

In Partial Fulfillment
of the Requirements for the Degree
Master of Science in Engineering Science and Mechanics

School of Civil and Environmental Engineering
Georgia Institute of Technology
December 2008

Copyright © 2008 by Michael Rainer Braun

Characterization of Nonlinearity Parameters in an Elastic Material with Quadratic Nonlinearity with a Complex Wave Field

Approved by:

Dr. Laurence J. Jacobs, Advisor
School of Civil and Environmental
Engineering
Georgia Institute of Technology

Dr. Jianmin Qu
George W. Woodruff School of Mechanical
Engineering
Georgia Institute of Technology

Dr. Reginald DesRoches
School of Civil and Environmental
Engineering
Georgia Institute of Technology

Date Approved: November 10, 2008

ACKNOWLEDGEMENTS

My sincere gratitude is expressed towards everyone who has supported me in doing the research presented in this thesis and my studies at the Georgia Institute of Technology.

First of all, I would like to thank Prof. Laurence J. Jacobs for being an outstanding advisor and teacher as well as good friend; his efforts made my stay at Georgia Tech possible in the first place. I want to thank him for his invaluable academic and organizational support but also for his steady encouragement during all stages of my research.

My gratefulness goes also to Prof. Jianmin Qu. I would like to thank him for his priceless advice and help in all stages of this research and particularly in the derivation of the analytical solutions presented in this thesis.

Moreover, I appreciate Prof. Reginald DesRoches' help and support, especially in the last steps of my research.

Of course, I have to thank Dipl.-Ing. Sebastian K  chler for making his simulation code and his data available to me. Without his explanations and his introductory help, it would have been impossible for me to run and understand the simulation code in this frame of time efficiently.

Special thanks go to Prof. Thorsten St   er for granting me access to his computer cluster. In particular, I appreciate his support with the parallelization and the respective software that has had to be applied. The extensive use of his computer cluster in combination with parallelized computing has been essential for gaining the amount of numerical data that has been necessary for my research.

My thankfulness goes also to Prof. Karim Sabra who has given me advice especially

in the investigation of the refraction effects. He inspired me to have a closer look at this interesting topic and provided me with the necessary background knowledge.

I would particularly like to thank Prof. Jin-Yeon Kim. His advice and his path-breaking suggestions have been an invaluable help in all stages of this research, but especially in the field of the reflection effects investigated where his experience has been an important help.

I also want to express my gratitude towards Prof. Lothar Gaul from the University of Stuttgart who gave me this unique chance to study at the Georgia Institute of Technology in the frame of an ISAP-program. Of course, my thanks go also to Helge Sprenger for organizing and supervising this exchange program. Furthermore, I thank the DAAD (German Academic Exchange Service) for providing the generous financial background that has been necessary for my studies abroad.

Finally, I would like to express my deepest gratitude towards my parents and my sister who have supported me in every respect before and during my time in the United States. Their unlimited confidence and encouragement have been the most important contribution that has been necessary to ensure the success of my year in America.

TABLE OF CONTENTS

ACKNOWLEDGEMENTS	iii
LIST OF TABLES	vii
LIST OF FIGURES	viii
LIST OF SYMBOLS OR ABBREVIATIONS	xiii
SUMMARY	xvii
I INTRODUCTION	1
II WAVE PROPAGATION	5
2.1 Equations of Motion	5
2.2 Constitutive Equations	7
2.2.1 Linearly Elastic Solids	7
2.2.2 Elastic Solids with Quadratic Nonlinearity	7
2.3 Compatibility Equations	8
2.4 Governing Equations for Wave Propagation in a Linearly Elastic Solid	8
2.5 Displacement Potentials	9
III WAVE PROPAGATION IN AN ELASTIC HALF-SPACE	11
3.1 Half-Space Subjected to a Uniform Surface Traction	12
3.1.1 Linear Stress-Strain Relationship	12
3.1.2 Nonlinear Stress-Strain Relationship	21
3.2 Half-Space Subjected to a Uniform Line Load	29
3.2.1 Linear Stress-Strain Relationship	29
3.2.2 Transformed Solution	32
3.2.3 Cagniard-deHoop Inversion of the Transformed Solution	36
3.2.4 Nonlinear Stress-Strain Relationship	54
3.3 Normal Reflection of a Plane Wave Generated by a Uniform Surface Traction in a Plate	56
3.3.1 Incident Wave	57

3.3.2	Reflection at a Rigid Boundary	60
3.3.3	Reflection at a Stress-Free Boundary	62
IV	NUMERICAL SIMULATION OF NONLINEAR WAVE PROPAGATION	66
4.1	Description of the Simulation Model	66
4.1.1	Numerical Scheme	66
4.1.2	Implementation	67
4.1.3	Evaluation	70
4.2	Description of the Simulation Procedure	71
V	NUMERICAL RESULTS	74
5.1	Half-Space Subjected to a Uniform Surface Traction	76
5.1.1	Pure Pressure Traction	77
5.1.2	Pure Shear Traction	86
5.1.3	Mixed Traction	97
5.1.4	Conclusion	103
5.2	Half-Space Subjected to a Uniform Line Load	104
5.2.1	Pure Pressure Traction Line Load	106
5.2.2	Pure Shear Traction Line Load	110
5.2.3	Conclusion	111
5.3	Simulation of a Finite-Size Transducer	115
5.3.1	Conclusion	118
5.4	Simulation of Reflection Effects	118
5.4.1	Plate with Two Stress-Free Sides	119
5.4.2	Plate with Two Rigidly Clamped Sides	122
5.4.3	Plate with One Stress-Free and One Rigidly Clamped Side	124
5.4.4	Conclusion	125
VI	CONCLUSION AND OUTLOOK	126
	REFERENCES	130

LIST OF TABLES

Table 5.1	Material parameters of Aluminum D54S.	76
Table 5.2	Simulation parameters used for the one-dimensional problems. .	77
Table 5.3	Simulation parameters used for the two-dimensional problems. .	105
Table 5.4	Simulation parameters used for the reflection problems.	119

LIST OF FIGURES

Figure 2.1	Balance of linear momentum.	6
Figure 3.1	Half-space subjected to a uniform pressure and shear load. . . .	12
Figure 3.2	Half-space subjected to uniform pressure load (left) and half-space subjected to uniform shear load (right).	13
Figure 3.3	Nonlinear half-space subjected to a uniform harmonic pressure and shear load.	22
Figure 3.4	Half-space subjected to line load.	30
Figure 3.5	Paths of integration used in the Cagniard-deHoop method. . . .	39
Figure 3.6	Definition of the introduced polar coordinates r and θ	40
Figure 3.7	Equivalent path of integration for the longitudinal part.	41
Figure 3.8	Equivalent path of integration for the transverse part (second case).	44
Figure 3.9	Equivalent paths of integration for $\theta = \frac{\pi}{2}$, longitudinal part (left) and transverse part (right).	47
Figure 3.10	Paths of integration around the Rayleigh pole at $\eta = is_r$	48
Figure 3.11	Nature of the arising displacement field in a half-space due to a line load $\sigma_{yy}(x, y = 0, t) = -QF(t)\delta(x)$ at a fixed time $t = t_0$	53
Figure 3.12	Plate subjected to a surface pressure at one side and clamped rigidly at the opposite side.	58
Figure 3.13	Plate subjected to a surface pressure at one side and a stress-free opposite side.	58
Figure 4.1	Numerical domain representing a half-space with a traction boundary condition at its surface.	69
Figure 4.2	Numerical domain representing a plate with different boundary conditions applied at its surfaces.	70
Figure 5.1	Particle velocity in y -direction at $\bar{y} = 2$ mm.	77
Figure 5.2	FFT of the particle velocity in y -direction at $\bar{y} = 2$ mm. The magnitude is normalized to its peak value.	78
Figure 5.3	Normalized ratio $\frac{A_2}{A_1^2}$ over the propagation distance y for different values of the third-order elastic constants.	80

Figure 5.4	Ratio $\frac{A_2}{A_1^2}$ over the propagation distance y for different values of the third-order elastic constants, normalized to the specific ratio obtained for the TOEC of Aluminum D54S.	81
Figure 5.5	Normalized ratio $\frac{A_2}{A_1^2}$ over the propagation distance y for different values of the third-order elastic constants, focused on small y . .	82
Figure 5.6	Normalized ratio $\frac{A_2}{A_1^2}$ over the propagation distance y for different values of the third-order elastic constants.	83
Figure 5.7	Ratio $\frac{A_2}{A_1^2}$ over the propagation distance y for different values of the third-order elastic constants, normalized to the specific ratio obtained for the TOEC of Aluminum D54S.	83
Figure 5.8	Normalized ratio $\frac{A_2}{A_1^2}$ over the propagation distance y for different values of the third-order elastic constants.	84
Figure 5.9	Ratio $\frac{A_2}{A_1^2}$ over the propagation distance y for different values of the third-order elastic constants, normalized to the specific ratio obtained for the TOEC of Aluminum D54S.	84
Figure 5.10	Normalized ratio $\frac{A_0}{A_1^2}$ over the propagation distance y for different values of the third-order elastic constants.	85
Figure 5.11	Ratio $\frac{A_0}{A_1^2}$ over the propagation distance y for different values of the third-order elastic constants, normalized to the specific ratio obtained for the TOEC of Aluminum D54S.	85
Figure 5.12	Normalized ratio $\frac{A_0}{A_1^2}$ over the propagation distance y for different values of the third-order elastic constants.	87
Figure 5.13	Ratio $\frac{A_0}{A_1^2}$ over the propagation distance y for different values of the third-order elastic constants, normalized to the specific ratio obtained for the TOEC of Aluminum D54S.	87
Figure 5.14	Normalized ratio $\frac{A_0}{A_1^2}$ over the propagation distance y for different values of the third-order elastic constants.	88
Figure 5.15	Ratio $\frac{A_0}{A_1^2}$ over the propagation distance y for different values of the third-order elastic constants, normalized to the specific ratio obtained for the TOEC of Aluminum D54S.	88
Figure 5.16	Normalized ratio $\frac{A_2}{B_1^2}$ over the propagation distance y for different values of the third-order elastic constants.	90
Figure 5.17	Ratio $\frac{A_2}{B_1^2}$ over the propagation distance y for different values of the third-order elastic constants, normalized to the specific ratio obtained for the TOEC of Aluminum D54S.	91

Figure 5.18	Normalized ratio $\frac{A_2}{B_1^2}$ over the propagation distance y for different values of the third-order elastic constants.	92
Figure 5.19	Ratio $\frac{A_2}{B_1^2}$ over the propagation distance y for different values of the third-order elastic constants, normalized to the specific ratio obtained for the TOEC of Aluminum D54S.	92
Figure 5.20	Normalized ratio $\frac{A_2}{B_1^2}$ over the propagation distance y for different values of the third-order elastic constants.	93
Figure 5.21	Ratio $\frac{A_2}{B_1^2}$ over the propagation distance y for different values of the third-order elastic constants, normalized to the specific ratio obtained for the TOEC of Aluminum D54S.	93
Figure 5.22	Normalized ratio $\frac{A_0}{B_1^2}$ over the propagation distance y for different values of the third-order elastic constants.	94
Figure 5.23	Ratio $\frac{A_0}{B_1^2}$ over the propagation distance y for different values of the third-order elastic constants, normalized to the specific ratio obtained for the TOEC of Aluminum D54S.	95
Figure 5.24	Normalized ratio $\frac{A_0}{B_1^2}$ over the propagation distance y for different values of the third-order elastic constants.	95
Figure 5.25	Ratio $\frac{A_0}{B_1^2}$ over the propagation distance y for different values of the third-order elastic constants, normalized to the specific ratio obtained for the TOEC of Aluminum D54S.	96
Figure 5.26	Normalized ratio $\frac{A_0}{B_1^2}$ over the propagation distance y for different values of the third-order elastic constants.	96
Figure 5.27	Ratio $\frac{A_0}{B_1^2}$ over the propagation distance y for different values of the third-order elastic constants, normalized to the specific ratio obtained for the TOEC of Aluminum D54S.	97
Figure 5.28	Normalized ratio $\frac{B_2}{A_1 B_1}$ over the propagation distance y for different values of the third-order elastic constants.	99
Figure 5.29	Ratio $\frac{B_2}{A_1 B_1}$ over the propagation distance y for different values of the third-order elastic constants, normalized to the specific ratio obtained for the TOEC of Aluminum D54S.	100
Figure 5.30	Normalized ratio $\frac{B_2}{A_1 B_1}$ over the propagation distance y for different values of the third-order elastic constants.	100
Figure 5.31	Ratio $\frac{B_2}{A_1 B_1}$ over the propagation distance y for different values of the third-order elastic constants, normalized to the specific ratio obtained for the TOEC of Aluminum D54S.	101

Figure 5.32	Normalized ratio $\frac{B_2}{A_1 B_1}$ over the propagation distance y for different values of the third-order elastic constants.	101
Figure 5.33	Ratio $\frac{B_2}{A_1 B_1}$ over the propagation distance y for different values of the third-order elastic constants, normalized to the specific ratio obtained for the TOEC of Aluminum D54S.	102
Figure 5.34	Normalized amplitudes A_2 and $10 A_0$ over the propagation distance y for the TOEC of Aluminum D54S. The point of intersection is approximately at $y_{10} = 1.97$ mm.	105
Figure 5.35	Particle velocity field \dot{u}_r over the entire domain at $t = 1.68 \mu\text{s}$. .	107
Figure 5.36	Particle velocity field \dot{u}_θ over the entire domain at $t = 1.68 \mu\text{s}$. .	107
Figure 5.37	Normalized ratio $\frac{A_2}{A_1^2}$ over the propagation distance r at $\theta = 0^\circ$ for different values of the third-order elastic constants.	108
Figure 5.38	Ratio $\frac{A_2}{A_1^2}$ over the propagation distance r at $\theta = 0^\circ$ for different values of the third-order elastic constants, normalized to the specific ratio obtained for the TOEC of Aluminum D54S. . . .	109
Figure 5.39	Normalized ratio $\frac{A_2}{A_1^2}$ over the propagation distance r at $\theta = 0^\circ$ for different values of the third-order elastic constants.	109
Figure 5.40	Ratio $\frac{A_2}{A_1^2}$ over the propagation distance r at $\theta = 0^\circ$ for different values of the third-order elastic constants, normalized to the specific ratio obtained for the TOEC of Aluminum D54S. . . .	110
Figure 5.41	Normalized ratio $\frac{A_2}{B_1^2}$ over the propagation distance r at $\theta = 0^\circ$ for different values of the third-order elastic constants.	111
Figure 5.42	Ratio $\frac{A_2}{B_1^2}$ over the propagation distance r at $\theta = 0^\circ$ for different values of the third-order elastic constants, normalized to the specific ratio obtained for the TOEC of Aluminum D54S. . . .	112
Figure 5.43	Normalized ratio $\frac{A_2}{B_1^2}$ over the propagation distance r at $\theta = 0^\circ$ for different values of the third-order elastic constants.	112
Figure 5.44	Ratio $\frac{A_2}{B_1^2}$ over the propagation distance r at $\theta = 0^\circ$ for different values of the third-order elastic constants, normalized to the specific ratio obtained for the TOEC of Aluminum D54S. . . .	113
Figure 5.45	Normalized ratio $\frac{A_0}{B_1^2}$ over the propagation distance r at $\theta = 0^\circ$ for different values of the third-order elastic constants.	113
Figure 5.46	Ratio $\frac{A_0}{B_1^2}$ over the propagation distance r at $\theta = 0^\circ$ for different values of the third-order elastic constants, normalized to the specific ratio obtained for the TOEC of Aluminum D54S. . . .	114

Figure 5.47	Normalized ratio $\frac{A_0}{B_1^2}$ over the propagation distance r at $\theta = 0^\circ$ for different values of the third-order elastic constants.	114
Figure 5.48	Ratio $\frac{A_0}{B_1^2}$ over the propagation distance r at $\theta = 0^\circ$ for different values of the third-order elastic constants, normalized to the specific ratio obtained for the TOEC of Aluminum D54S. . . .	115
Figure 5.49	Spatial distribution of the pressure traction Q_1 applied at the half-space's surface which is used to model a transducer with length b	116
Figure 5.50	Directivity pattern at a propagation distance $r_0 = 1.6b$ obtained for the transducer model and for a line load, expressed by the ratio $\frac{A_1(\theta)}{A_1(0^\circ)}$ over the angle θ	117
Figure 5.51	Directivity pattern of Fig. 5.50 expressed in a semi-logarithmic scale.	118
Figure 5.52	Normalized ratio $\frac{A_2}{A_1^2}$ over the accumulated propagation distance r which is expressed in multiples of the plate's thickness L . Both sides of the plate are stress-free.	120
Figure 5.53	Normalized ratio $\frac{A_0}{A_1^2}$ over the accumulated propagation distance r which is expressed in multiples of the plate's thickness L . Both sides of the plate are stress-free.	121
Figure 5.54	Normalized ratio $\frac{A_2}{A_1^2}$ over the accumulated propagation distance r which is expressed in multiples of the plate's thickness L . Both sides of the plate are rigidly clamped.	122
Figure 5.55	Normalized ratio $\frac{A_0}{A_1^2}$ over the accumulated propagation distance r which is expressed in multiples of the plate's thickness L . Both sides of the plate are rigidly clamped.	123
Figure 5.56	Normalized ratio $\frac{A_2}{A_1^2}$ over the accumulated propagation distance r which is expressed in multiples of the plate's thickness L	124
Figure 5.57	Normalized ratio $\frac{A_0}{A_1^2}$ over the accumulated propagation distance r which is expressed in multiples of the plate's thickness L . The side of the transducer is stress-free, the opposite side is rigidly clamped.	125

LIST OF SYMBOLS OR ABBREVIATIONS

BC	boundary condition
FFT	fast Fourier transform
ODE / PDE	ordinary / partial differential equation
NDE	nondestructive evaluation
TOEC	third-order elastic constants (Murnaghan coefficients)
OpenMP	Open Multi-Processing
$x, y, z; x_i$	spatial coordinates
t	time coordinate
f	frequency
ω	$2\pi f$, angular frequency
c_l, c_t, c_r	longitudinal, transverse and Rayleigh wave speed
s_l, s_t, s_r	longitudinal, transverse and Rayleigh wave slowness
k_l, k_t	longitudinal and transverse wavenumber
V	volume
S	∂V , surface
$\mathbf{n}; n_i$	outward unit normal vector
$\mathbf{b}; b_i$	body force per unit mass
$\mathbf{t}; t_i$	traction per unit area
$\boldsymbol{\sigma}; \sigma_{ij}$	stress tensor

$\boldsymbol{\varepsilon}; \varepsilon_{ij}$	strain tensor
$\boldsymbol{u}; u_i; u, v, w$	particle displacement vector
$\boldsymbol{v}; v_i; \dot{u}, \dot{v}, \dot{w}$	particle velocity vector
φ	scalar potential
$\boldsymbol{\psi}; \psi_i$	vector potential
ρ	density
λ, μ	second-order elastic constants (Lamé constants)
l, m, n	third-order elastic constants (Murnaghan coefficients)
Γ	internal energy density
I_i	invariants of the strain tensor
$F(t)$	shape function of the excitation signal
Q	reference stress amplitude
Q_1	pressure stress amplitude of the excitation signal
Q_2	shear stress amplitude of the excitation signal
f_f	frequency of the excitation signal
Δt	duration of the excitation signal
L	thickness of the plate
r	accumulated propagation distance
b	width of the transducer
f_i	frequency of the i th-harmonic
A_i	magnitude of the particle velocity in the direction of wave propagation (i th-harmonic)

B_i	magnitude of the particle velocity normal to the direction of wave propagation (i th-harmonic)
β, γ	acoustical nonlinearity parameters
$\delta(\cdot)$	Dirac delta impulse function
$H(\cdot)$	Heaviside step function
\mathbf{I}	identity matrix
δ_{ij}	Kronecker delta symbol
ξ	real coordinate used for the Fourier transform
p	complex coordinate used for the Laplace transform
η	$\frac{\xi}{p}$, characteristic coordinate
r, θ	polar coordinates
u_r, u_θ	displacements in polar coordinates
θ_{cr}	critical angle
$\bar{f}(p)$	Laplace transform of $f(t)$
$\hat{f}(\xi)$	Fourier transform of $f(x)$
$\Delta x, \Delta y$	lengths of a grid cell
$\mathbf{v}(x, y, t)$	state vector
$\mathbf{f}(\mathbf{v}), \mathbf{g}(\mathbf{v})$	flux function vectors
$\mathbf{q}(x, y, t); q^i(x, y, t)$	numerical approximation of the state vector
$\boldsymbol{\omega}$	$[\omega_x, \omega_y]$, unit direction vector in the (x, y) -domain
$\mathbf{H}(\mathbf{v}, \boldsymbol{\omega})$	matrix used to determine hyperbolicity
S_p	speedup on a system with p processors

$\nabla \cdot \mathbf{a}$	divergence of vector field \mathbf{a}
∇b	gradient of scalar field b
$\nabla^2 \mathbf{a}$	Laplace operator of vector field \mathbf{a}
$\nabla \wedge \mathbf{a}$	curl of vector field \mathbf{a}

SUMMARY

This research investigates wave propagation in an elastic half-space with a quadratic nonlinearity in its stress-strain relationship. Different boundary conditions on the surface are considered that result in both one- and two-dimensional wave propagation problems. The goal of the research is to examine the generation of second-order frequency effects and static effects which may be used to determine the nonlinearity present in the material. This is accomplished by extracting the amplitudes of those effects in the frequency domain and analyzing their dependency on the third-order elastic constants (TOEC). For the one-dimensional problems, both analytical approximate solutions as well as numerical simulations are presented. For the two-dimensional problems, numerical solutions are presented whose dependency on the material's nonlinearity is compared to the one-dimensional problems. The numerical solutions are obtained by first formulating the problem as a hyperbolic system of conservation laws, which is then solved numerically using a semi-discrete central scheme. The numerical method is implemented using the package CentPack. In the one-dimensional cases, it is shown that the analytical and numerical solutions are in good agreement with each other, as well as how different boundary conditions may be used to measure the TOEC. In the two-dimensional cases, it is shown that there exist comparable dependencies of the second-order frequency effects and static effects on the TOEC. Finally, it is analytically and numerically investigated how multiple reflections in a plate can be used to simplify measurements of the material nonlinearity in an experiment.

CHAPTER I

INTRODUCTION

Ultrasonic measurement techniques have evolved into important tools for the nondestructive evaluation (NDE) of components in many fields of engineering. A recent, significant application is the determination of a component's remaining structural life by quantitatively measuring its current damage-state.

While linear ultrasonic measurement techniques are usually applied to detect macroscopic damage such as cracks, they are not appropriate for measuring microscopic damage; mainly because damage does not have a strong influence on a component's linear material properties as, for example, the Lamé constants. Thus, another measurement technique is needed to detect microscopic fatigue damage that can develop before any macroscopic damage arises. Such an early detection method is particularly important for fatigue critical components. Therefore, nonlinear ultrasonic methods have been considered to detect such fatigue damage. Here, the generation of “additional” harmonics whose frequencies are integer multiples of the input signal's frequency is used to gain information on the damage-state of a component [10], [6]. This generation of harmonics is in general due to a nonlinearity both in the stress-strain relationship and the displacement-strain relationship of the material. A quadratic nonlinearity in the stress-strain relationship can be expressed by the third-order elastic constants (TOEC) which are also known as Murnaghan coefficients. In the recent past, both experimental studies [10], [6], [8] and physical models [11] have shown that fatigue damage is directly correlated to a nonlinearity parameter β which is a specific function of the TOEC. Therefore, an experimental determination of a material's nonlinearity from the additional harmonics generated can be used to measure the

microscopic fatigue damage in a quantitative fashion. It should also be mentioned that fatigue damage is not the only source for the presence of nonlinearity in a material; there exist, for example, materials being naturally nonlinear such as rock or sandstone.

An important prerequisite in any procedure to use nonlinear ultrasound to quantify remaining structural life is the ability to determine the TOEC of an in situ component which will often result in the excitation of a complicated ultrasonic wave field. Therefore, the focus of this research is on the analytical and numerical examination of the relation between the TOEC and the nonlinear effects appearing in certain wave fields in elastic solids.

The basic experimental approach that shall be reproduced with analytical and numerical models looks as follows – a transducer is applied to the free surface of a component and the particle velocity emerging at a certain position is measured. The measured time signal is then analyzed in the frequency domain with an appropriate signal processing in order to determine the amplitudes of the harmonics generated. Note that the position selected for detection has a significant influence on the signal measured. Since these amplitudes are correlated to the TOEC, it is possible to compute the TOEC of the material which carry the information about the current damage-state of the material. Throughout this research, the geometry chosen as the “component” is a half-space. Clearly, this is a relatively unrealistic scenario for an experiment, but it is applied here in order to keep the analytical considerations and numerical simulations as straightforward as possible. However, at the end of this thesis, a plate-like geometry is also considered which is closer to an experimentally realizable scenario. The transducer that is applied at the surface is modeled in different ways which differ in their complexity. On the one hand, the transducer generates either a pure pressure, a pure shear or a mixed traction. On the other hand, different

shapes of the transducer are examined which correspond to different boundary conditions at the surface which vary in their spatial dependency. Note that the transducer is always modeled as a traction boundary condition because this approach is closer to reality than prescribing the boundary condition in terms of the particle displacement or the particle velocity.

The spatial form of the boundary condition determines the spatial dependency of the wave field arising. In this research, only boundary conditions leading to one- or two-dimensional wave fields are considered. However, only the one-dimensional ones are investigated analytically for nonlinear materials because, to the author's best knowledge, no solution to the nonlinear two-dimensional problem is currently available. These nonlinear approximate solutions have been derived by making use of the perturbation theory. It is shown that for an elastic material with quadratic nonlinearity in its constitutive equation not only components with the frequency of the harmonic excitation appear in the particle velocity field but also double-frequency and static terms. Similar analytical derivations were presented in [22], [24], [26] or [5]. There, the appearance of second-harmonic effects in the particle displacement due to a displacement or velocity boundary condition is explained. Another analytical derivation with a special focus on static effects occurring in nonlinear wave propagation is given in [7]. Moreover, since such static effects are an important aspect of this research, it shall be pointed out that experiments investigating them have been conducted [25], [9], [20], partly in recent past. Another aspect of this research is the reflection of an incident plane wave at both a rigid and a stress-free boundary in a nonlinear material. An analytical consideration of a reflection at a stress-free boundary is presented in [3].

The numerical investigation has been carried out with a simulation code that is based on a numerical solver, CentPack [2], that has been adapted to the field of nonlinear wave propagation in an elastic half-space by Küchler [12], [13]. CentPack is used here to solve a hyperbolic system of conservation laws with a semi-discrete central scheme

for a two-dimensional domain. A similar study on the numerical investigation of one-dimensional nonlinear wave propagation has been previously presented in [18]. In addition to the problems that have also been solved analytically as mentioned above, two-dimensional problems are solved, including simulations where the traction applied to the half-space's surface is either a uniform load, a line load or a transducer model with a finite dimension.

This thesis is organized as follows – in Chapter 2, a brief survey of wave propagation is given that shall introduce some general technical terms and explain general wave phenomena. This is essential to understanding all of the subsequent chapters. In Chapter 3, analytical (approximate) solutions to the one-dimensional problems investigated in this thesis are presented as well as a solution to the linear two-dimensional problem. The latter one is given here because it is fundamental for the understanding of the nonlinear two-dimensional problem. Chapter 4 gives an overview of the simulation code that has been applied in order to obtain the numerical results presented in this work. A short description of the numerical model and its computational implementation is presented there. Additionally, major changes made to the original code are outlined briefly. In Chapter 5, the results of the numerical simulations are provided. Furthermore, they are discussed and compared to the analytical models presented in Chapter 3. The last part of this thesis is Chapter 6 where final conclusions are given.

CHAPTER II

WAVE PROPAGATION IN ELASTIC SOLIDS

In this chapter, some fundamentals of wave propagation in elastic solids are provided. These are important for the understanding of the subsequent chapters where the theory of linear and nonlinear wave propagation in an elastic half-space will be presented. At first, the governing differential equations describing dynamic elasticity are derived. Therefore, several types of equations relating different field variables are presented in the following. These will be combined in such a way that the resulting system of partial differential equations is formulated only in terms of the displacement field.

2.1 Equations of Motion

The equations of motion for wave propagation in an elastic solid can be derived by application of the principle of linear momentum to a three-dimensional free body. This free body with volume V and surface S is supposed to be continuous. Its density ρ may be a function of space and time. Here, both body forces \mathbf{b} per unit mass and traction \mathbf{t} per unit area are considered. The situation is shown in Fig. 2.1. Thus, the principle of linear momentum can be stated as

$$\int_S \mathbf{t} dS + \int_V \rho \mathbf{b} dV = \frac{d}{dt} \int_V \rho \mathbf{v} dV \quad (2.1)$$

where \mathbf{v} is the body's velocity field. Introducing rectangular coordinates and index notation, this can be restated as

$$\int_S t_i dS + \int_V \rho b_i dV = \frac{d}{dt} \int_V \rho v_i dV. \quad (2.2)$$

In Eq. (2.2), the traction can be expressed as

$$t_i = \sigma_{ji} n_j \quad (2.3)$$

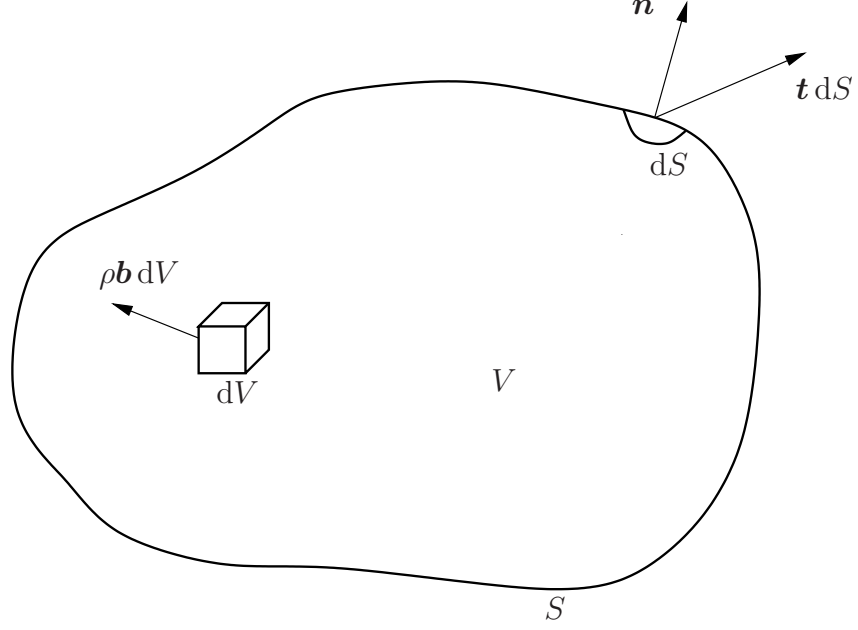


Figure 2.1: Balance of linear momentum.

where σ_{ji} denotes the components of the stress tensor $\boldsymbol{\sigma}$ and n_j represents the components of the outward normal unit vector \mathbf{n} of the body's surface S . Application of the divergence theorem to the surface integral and rearranging of all terms to the left side, the momentum balance takes then the form

$$\int_V \left[\frac{\partial \sigma_{ji}}{\partial x_j} + \rho b_i - \rho \frac{d^2 u_i}{dt^2} \right] dV = 0 \quad (2.4)$$

where the components of the displacement field \mathbf{u} are related to the velocity field by $v_i = \frac{du_i}{dt}$. Since Eq. (2.4) is true for any arbitrary volume V , it can be stated for each point that

$$\frac{\partial \sigma_{ji}}{\partial x_j} + \rho b_i - \rho \frac{d^2 u_i}{dt^2} = 0. \quad (2.5)$$

This formulation in index notation can be rewritten in a more compact form

$$\sigma_{ji,j} + \rho b_i = \rho \ddot{u}_i \quad (2.6)$$

or in vector notation

$$\nabla \cdot \boldsymbol{\sigma} + \rho \mathbf{b} = \rho \ddot{\mathbf{u}}. \quad (2.7)$$

Equations (2.6) are known as *Cauchy's Equations of Motion*. It shall be pointed out that, in a similar way, the symmetry of the stress tensor $\boldsymbol{\sigma}$ can be derived from the moment of momentum principle. The derivation can be found in [16] or in [1].

2.2 Constitutive Equations

2.2.1 Linearly Elastic Solids

For a material with a linear relationship between stress and strain, the components of the stress tensor $\boldsymbol{\sigma}$ are given by

$$\sigma_{ij} = C_{ijkl} \varepsilon_{kl} \quad (2.8)$$

where ε_{kl} represents the components of the strain tensor that will be presented in the following section. The components of the fourth-order tensor C_{ijkl} are constant for a homogeneous material, and according to [1], they can be expressed as

$$C_{ijkl} = \lambda \delta_{ij} \delta_{kl} + \mu (\delta_{ik} \delta_{jl} + \delta_{il} \delta_{jk}) \quad (2.9)$$

for an isotropic material. The material constants λ and μ are the second-order elastic constants (or Lamé's elastic constants). In this research, only homogeneous and isotropic materials will be considered. Plugging Eq. (2.9) in Eq. (2.8) yields

$$\sigma_{ij} = \lambda \varepsilon_{kk} \delta_{ij} + 2\mu \varepsilon_{ij}. \quad (2.10)$$

2.2.2 Elastic Solids with Quadratic Nonlinearity

If third-order terms are to be considered in the relationship between the stress and the strain, the internal energy density Γ can be used for the derivation since it is

$$\sigma_{ij} = \frac{\partial \Gamma}{\partial u_{i,j}}. \quad (2.11)$$

In this case, according to [17], the internal energy density is given by

$$\Gamma = \frac{\lambda + 2\mu}{2} I_1^2 - 2\mu I_2 + \frac{l + 2m}{3} I_1^3 - 2m I_1 I_2 + n I_3 \quad (2.12)$$

where l , m and n represent the third-order elastic constants which are also known as Murnaghan coefficients. The terms I_1 , I_2 and I_3 denote the three invariants of the strain tensor. They are defined as

$$\begin{aligned} I_1 &= \varepsilon_{ii}, \\ I_2 &= \begin{vmatrix} \varepsilon_{22} & \varepsilon_{23} \\ \varepsilon_{32} & \varepsilon_{33} \end{vmatrix} + \begin{vmatrix} \varepsilon_{33} & \varepsilon_{31} \\ \varepsilon_{13} & \varepsilon_{11} \end{vmatrix} + \begin{vmatrix} \varepsilon_{11} & \varepsilon_{12} \\ \varepsilon_{21} & \varepsilon_{22} \end{vmatrix}, \\ I_3 &= \det \varepsilon_{ij}. \end{aligned} \tag{2.13}$$

The strain tensor ε itself will be presented in more detail in the subsequent section.

2.3 Compatibility Equations

Finally, a relationship connecting the strain and the displacement in an elastic body is needed. Since only small deformations and deformation gradients shall be considered in this research, it is justified to use the so-called small strain in which geometric nonlinearities are ignored. The small strain tensor ε is given by

$$\varepsilon = \frac{1}{2}(\mathbf{u}\nabla + \nabla\mathbf{u}) \tag{2.14}$$

where higher-order terms are neglected and where \mathbf{u} again is the displacement vector field. In index notation, this is

$$\varepsilon_{ij} = \frac{1}{2}(u_{i,j} + u_{j,i}). \tag{2.15}$$

2.4 Governing Equations for Wave Propagation in a Linearly Elastic Solid

Now, Eqs. (2.6), (2.10) and (2.15) describe the problem of dynamic elasticity for an linearly elastic material if geometric nonlinearity is neglected. They are formulated in terms of the dependent field variables \mathbf{u} , ε and $\boldsymbol{\sigma}$. By plugging Eqs. (2.10) and (2.15) in Eq. (2.6), the problem can be stated just in terms of the displacement \mathbf{u} . In

index notation, this is

$$\mu u_{i,jj} + (\lambda + \mu) u_{j,ji} + \rho f_i = \rho \ddot{u}_i. \quad (2.16)$$

Alternatively, this system of three coupled partial differential equations may be expressed in vector notation as

$$\mu \nabla^2 \mathbf{u} + (\lambda + \mu) \nabla \nabla \cdot \mathbf{u} + \rho \mathbf{f} = \rho \ddot{\mathbf{u}}. \quad (2.17)$$

Thus, Eq. (2.16), completed by an appropriate set of boundary conditions and initial conditions, describes the problem of wave propagation in linearly elastic solids.

2.5 *Displacement Potentials*

Equations (2.16) and (2.17) have the considerable disadvantage that its three components are coupled. A convenient approach to avoid this circumstance is to express the components of the displacement vector in terms of the derivatives of some potential functions. If body forces are not considered, Eq. (2.17) will become

$$\mu \nabla^2 \mathbf{u} + (\lambda + \mu) \nabla \nabla \cdot \mathbf{u} = \rho \ddot{\mathbf{u}}. \quad (2.18)$$

In [1], it is suggested to apply the so-called Helmholtz decomposition to the displacement vector. This decomposition has the form

$$\mathbf{u} = \nabla \varphi + \nabla \times \boldsymbol{\psi}, \quad (2.19)$$

where φ is a scalar function and $\boldsymbol{\psi}$ is a vector function. Plugging Eq. (2.19) in Eq. (2.18) yields

$$\begin{aligned} & \mu \nabla^2 [\nabla \varphi + \nabla \times \boldsymbol{\psi}] + (\lambda + \mu) \nabla \nabla \cdot [\nabla \varphi + \nabla \times \boldsymbol{\psi}] \\ &= \rho \frac{\partial^2}{\partial t^2} [\nabla \varphi + \nabla \times \boldsymbol{\psi}]. \end{aligned} \quad (2.20)$$

With the vector identities $\nabla \cdot \nabla \varphi = \nabla^2 \varphi$ and $\nabla \cdot \nabla \times \boldsymbol{\psi} = 0$, this can be rearranged so that

$$\nabla [(\lambda + 2\mu) \nabla^2 \varphi - \rho \ddot{\varphi}] + \nabla \times [\mu \nabla^2 \boldsymbol{\psi} - \rho \ddot{\boldsymbol{\psi}}] = 0. \quad (2.21)$$

Obviously, this means that Eq. (2.18) is satisfied if the equations

$$\nabla^2 \varphi = \frac{1}{c_l^2} \ddot{\varphi} \quad (2.22)$$

and

$$\nabla^2 \boldsymbol{\psi} = \frac{1}{c_t^2} \ddot{\boldsymbol{\psi}} \quad (2.23)$$

hold, where c_l and c_t are defined as

$$c_l = \sqrt{\frac{\lambda + 2\mu}{\rho}} \quad \text{and} \quad c_t = \sqrt{\frac{\mu}{\rho}}. \quad (2.24)$$

It should be mentioned that the Helmholtz decomposition in Eq. (2.19) relates the three components of the displacement vector u_i to one scalar potential φ and the three components of the vector potential ψ_i . Clearly, an additional constraint to these potentials has to be established in order to make the decomposition unique. In [1], it is justified why the condition $\boldsymbol{\nabla} \cdot \boldsymbol{\psi} = 0$ is used in many cases.

CHAPTER III

WAVE PROPAGATION IN AN ELASTIC HALF-SPACE

In this chapter, analytical solutions for the wave fields arising in an elastic half-space due to different boundary conditions are presented. A half-space is a half-infinite domain that has one boundary plane. In this research, all of the given presentations are limited to both homogeneous and isotropic materials. Moreover, only small strain is considered here, meaning that the relationship between displacement and strain is assumed to be linear. However, the subsequent derivations are provided for two different types of constitutive equations: a linear stress-strain relationship, and a stress-strain relationship with quadratic nonlinearity. The boundary conditions applied can also be divided into two different cases. The first case is a uniform traction on the entire boundary plane; both pressure and shear traction are considered. Since the developing wave field will only depend on one spatial coordinate, this situation may be considered as a one-dimensional problem. The second type of boundary condition investigated is a uniform line traction on the surface of the half-space. Here, the arising displacement field will depend on two spatial coordinates so that this represents a two-dimensional problem. Note that, for the case of nonlinear constitutive equations, analytical solutions may not be available in a closed form without some restrictions.

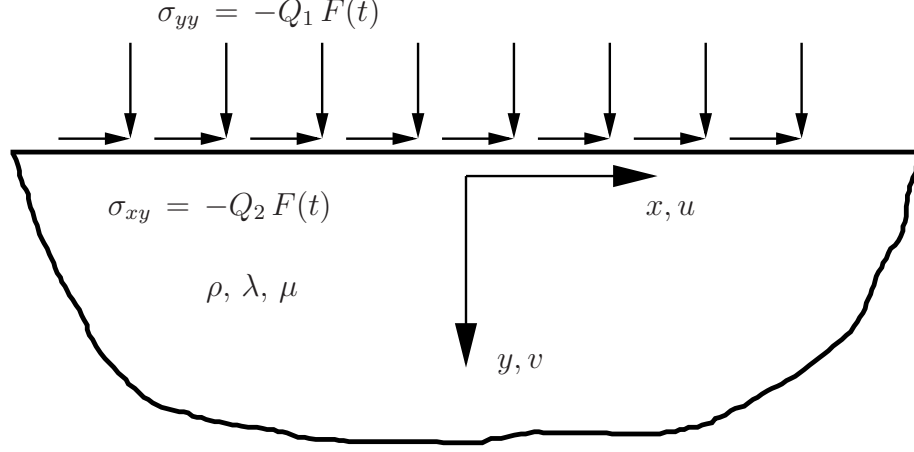


Figure 3.1: Half-space subjected to a uniform pressure and shear load.

3.1 *Half-Space Subjected to a Uniform Surface Traction*

3.1.1 Linear Stress-Strain Relationship

The first and simplest case considered in this chapter is a half-space $y \geq 0$ subjected to a uniform surface traction. Here, the more general case of both pressure and shear traction applied to the surface is considered. For now, the stress-strain relationship of the half-space's material is chosen to be linear, as given by Eq. (2.8). This situation is shown in Fig. 3.1 where, for convenience, the notation u and v for the displacements and x and y for the coordinates was introduced instead of the more general notation u_i and x_i that was used in the previous chapter. The boundary condition for this case can be formulated as

$$\sigma_{yy}(x, y = 0, t) = -Q_1 F(t) \quad (3.1)$$

$$\sigma_{xy}(x, y = 0, t) = -Q_2 F(t) \quad (3.2)$$

where Q_1 and Q_2 are the traction amplitudes and $F(t)$ is a dimensionless shape function of time with $F(t) = 0$ for $t < 0$. Since it is always possible to orient the coordinate system in a way that the uniform shear traction is directed to one of the axial directions (x -direction in this case), it is assumed without loss of generality

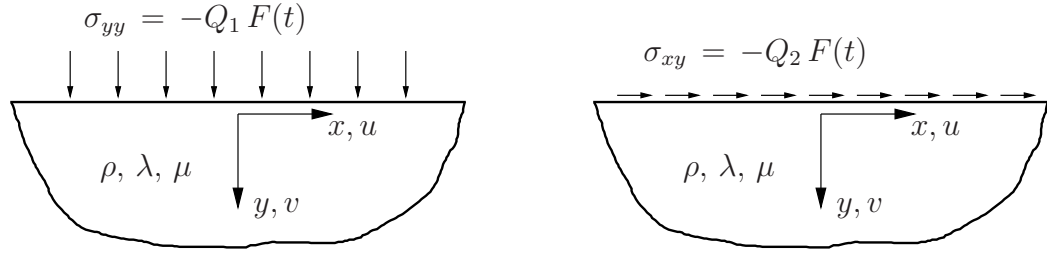


Figure 3.2: Half-space subjected to uniform pressure load (left) and half-space subjected to uniform shear load (right).

that the second shear traction on the surface vanishes. The initial condition for this problem is that the half-space is assumed to be initially at rest.

However, for the derivation of the analytical solution to the developing wave field, the problem is divided into two simpler problems. These problems will be solved separately and the solutions found will be superposed what is possible because of the linearity of the entire problem presented in this section. Note that this approach would be inappropriate for the problems including a nonlinear stress-strain relationship that will be considered later on. Here, linearity means that the equations of motion, the compatibility equations and the constitutive equations are all linear. Figure 3.2 shows how the initial problem is split into the two simpler problems.

3.1.1.1 Half-Space Subjected to a Uniform Pressure Load

At first, only the pressure boundary condition is considered, as shown on the left side of Fig. (3.2). The solution to this problem is based on that one given by [1]. According to Eq. (3.1), the boundary condition is given by

$$\sigma_{yy}(x, y = 0, t) = -Q_1 F(t) \quad (3.3)$$

$$\sigma_{xy}(x, y = 0, t) = 0 \quad (3.4)$$

where $F(t) = 0$ for $t < 0$. Obviously, every plane that is parallel to the y -axis has to be a plane of symmetry because the boundary condition has no spatial dependency. However, this means that displacements u in x -direction and w in z -direction vanish

and only displacements v in the y -direction are possible. Moreover, since this a one-dimensional problem, it is $v = v(y, t)$. Equivalently, all of the other field variables can only be functions of y and t . Using this insight, the equations of motion (2.6) reduce to one equation for the displacement v (equivalent to u_2) that can be written in the absence of body forces as

$$\rho \frac{\partial^2 v}{\partial t^2} = \frac{\partial \sigma_{yy}}{\partial y}. \quad (3.5)$$

Accordingly, the linear compatibility equations (2.15) reduce to

$$\varepsilon_{yy} = \frac{\partial v}{\partial y} \quad (3.6)$$

and the only stress component needed here, σ_{yy} , can be stated from (2.10) as

$$\sigma_{yy} = (\lambda + 2\mu) \varepsilon_{yy}. \quad (3.7)$$

Plugging Eqs. (3.6) and (3.7) in Eq. (3.5) yields the equation of motion in terms of the displacement v

$$\frac{\partial^2 v}{\partial y^2} = \frac{1}{c_1^2} \frac{\partial^2 v}{\partial t^2} \quad (3.8)$$

where c_1 is defined as in Eq. (2.24).

The initial conditions may be expressed in terms of the displacement v in the bulk of the half-space as

$$\left. \begin{aligned} v(y, t = 0) &= 0 \\ \dot{v}(y, t = 0) &= 0 \end{aligned} \right\} \quad \text{for } y > 0. \quad (3.9)$$

The general solution to the partial differential equation (3.8) is derived in [1] and can easily be verified by inserting to be

$$v(y, t) = f\left(t - \frac{y}{c_1}\right) + g\left(t + \frac{y}{c_1}\right) \quad (3.10)$$

where $f(\cdot)$ and $g(\cdot)$ are two arbitrary functions which can be determined for a specific problem by the application of both the initial and the boundary conditions. Thus,

inserting in (3.9) yields

$$\left. \begin{aligned} f\left(-\frac{y}{c_1}\right) + g\left(\frac{y}{c_1}\right) &= 0 \\ f'\left(-\frac{y}{c_1}\right) + g'\left(\frac{y}{c_1}\right) &= 0 \end{aligned} \right\} \quad \text{for } y > 0. \quad (3.11)$$

Here, primes mean differentiations with respect to the argument of the respective function. Now, differentiation of the first equation in (3.11) with respect to the argument $\frac{y}{c_1}$ yields a system of equations that is linear in f' and g' , that is

$$\left. \begin{aligned} -f'\left(-\frac{y}{c_1}\right) + g'\left(\frac{y}{c_1}\right) &= 0 \\ f'\left(-\frac{y}{c_1}\right) + g'\left(\frac{y}{c_1}\right) &= 0 \end{aligned} \right\} \quad \text{for } y > 0. \quad (3.12)$$

Clearly, solving (3.12) leads to

$$\left. \begin{aligned} f'\left(-\frac{y}{c_1}\right) &= 0 \\ g'\left(\frac{y}{c_1}\right) &= 0 \end{aligned} \right\} \quad \text{for } y > 0. \quad (3.13)$$

Integrating these expressions with respect to their arguments and making use of the first equation in (3.11) yields the result

$$f\left(-\frac{y}{c_1}\right) = -g\left(\frac{y}{c_1}\right) = A \quad \text{for } y > 0 \quad (3.14)$$

where A is a constant that still has to be determined from the boundary condition. Now, considering only the situation $t \geq 0$ and $y > 0$, the general solution to the displacement v given by Eq. (3.10) may be split into two time intervals $t > \frac{y}{c_1}$ and $t < \frac{y}{c_1}$ as

$$v(y, t) = \begin{cases} f\left(t - \frac{y}{c_1}\right) - A & \text{for } t > \frac{y}{c_1} \\ 0 & \text{for } t < \frac{y}{c_1}. \end{cases} \quad (3.15)$$

This is possible since, here, the term $t + \frac{y}{c_1}$ is always positive and thus, the term $g\left(t + \frac{y}{c_1}\right)$ is always equal to $-A$ according to Eq. (3.14). Beyond that, the argument

$t - \frac{y}{c_1}$ is negative for $t < \frac{y}{c_1}$ so that $f\left(t - \frac{y}{c_1}\right)$ is equal to A , also according to Eq. (3.14). It is already possible to conclude from this intermediate result that any material particle located at $y = \bar{y}$ remains in its undisturbed position until the wavefront traveling with the wave speed c_1 arrives at the time $\bar{t} = \frac{\bar{y}}{c_1}$.

Using Eq. (3.15) for times $t > \frac{y}{c_1}$ to evaluate the boundary condition (3.3) at $y = 0$ yields

$$-\frac{\lambda + 2\mu}{c_1} f'(t) = -Q_1 F(t). \quad (3.16)$$

From this, it can be found by integration that

$$f\left(t - \frac{y}{c_1}\right) - \underbrace{f(0)}_B = \frac{c_1 Q_1}{\lambda + 2\mu} \int_{s=0}^{s=t-\frac{y}{c_1}} F(s) ds. \quad (3.17)$$

The unknown constant B can be determined by a comparison to Eq. (3.14). Considering $t = 0$, the integral in the equation above vanishes since the integrand $F(s)$ is zero for $s < 0$ (according to the definition of the boundary condition) and obviously, it has to be $B = A$. This result can now be plugged into Eq. (3.15), yielding

$$v(y, t) = \frac{c_1 Q_1}{\lambda + 2\mu} \int_{s=0}^{s=t-\frac{y}{c_1}} F(s) ds. \quad (3.18)$$

It shall be mentioned that the case differentiation of Eq. (3.15) is no longer needed because the integral vanishes automatically for the case $t < \frac{y}{c_1}$.

The corresponding particle velocity $\dot{v}(y, t)$ is easily found by differentiation of the particle displacement v with respect to time to be

$$\dot{v}(y, t) = \frac{c_1 Q_1}{\lambda + 2\mu} F\left(t - \frac{y}{c_1}\right). \quad (3.19)$$

3.1.1.2 Half-Space Subjected to a Uniform Shear Load

Now, only the shear boundary condition is considered, as shown on the right side of Fig. 3.2. The solution to this problem is very similar to that one shown for the

pressure load. Thus, only an abbreviated derivation will be presented in the following. According to Eq. (3.1), the boundary condition is now given by

$$\sigma_{yy}(x, y = 0, t) = 0 \quad (3.20)$$

$$\sigma_{xy}(x, y = 0, t) = -Q_2 F(t) \quad (3.21)$$

where $F(t)$ is the same time signal as for the pressure load. Again, it is $F(t) = 0$ for $t < 0$. Obviously, for this specific case, every plane that is parallel to the xy -plane is a plane of symmetry. This implies that the displacement w in the z -direction has to vanish.

Again, as in the above case for the pressure load, this problem is a one-dimensional problem since the stated boundary condition does not depend on the coordinates x or z . This means that every field variable can only be a function of y and t , including the displacements $u = u(y, t)$ and $v = v(y, t)$. Application of this knowledge reduces the displacement equations of motion (2.16) in the absence of body forces to the two uncoupled partial differential equations, one for each considered displacement

$$\frac{\partial^2 v}{\partial y^2} = \frac{1}{c_1^2} \frac{\partial^2 v}{\partial t^2} \quad (3.22)$$

$$\frac{\partial^2 u}{\partial y^2} = \frac{1}{c_t^2} \frac{\partial^2 u}{\partial t^2} \quad (3.23)$$

where c_1 and c_t are defined as in Eq. (2.24). Again, for $t < 0$, the half-space shall be at rest so that the respective initial conditions can be formulated as

$$\left. \begin{aligned} v(y, t = 0) &= \dot{v}(y, t = 0) = 0 \\ u(y, t = 0) &= \dot{u}(y, t = 0) = 0 \end{aligned} \right\} \quad \text{for } y > 0. \quad (3.24)$$

The solution for the displacement v in the y -direction follows exactly the derivation given in Section 3.1.1.1 until the boundary condition is applied in Eq. (3.16). Of course, in the present case, the new boundary condition (3.20) has to be used instead.

Its evaluation for times $t > \frac{y}{c_1}$ at $y = 0$ yields

$$\begin{aligned} -\frac{\lambda + 2\mu}{c_1} f'(t) &= 0 \quad \text{or} \\ f'(t) &= 0. \end{aligned} \tag{3.25}$$

Integration with fixed boundaries provides

$$f\left(t - \frac{y}{c_1}\right) - \underbrace{f(0)}_B = \int_{s=0}^{s=t-\frac{y}{c_1}} 0 \, ds = 0. \tag{3.26}$$

If this term is evaluated for $t = 0$ and compared to Eq. (3.14) which still applies since the initial conditions have remained unchanged, it becomes obvious that $B = A$. Thus, plugging $f\left(t - \frac{y}{c_1}\right) = A$ in Eq. (3.15) yields the final result

$$v(y, t) = 0 \quad \text{for } y > 0 \tag{3.27}$$

meaning that the shear boundary condition does not create any displacement in the direction of the propagation which is not very surprising. Moreover, it is of course

$$\dot{v}(y, t) = 0 \quad \text{for } y > 0. \tag{3.28}$$

Now, the displacement u parallel to the free surface which is described by the partial differential equation (3.23) shall be investigated. It shall be mentioned that the same approach used above may be chosen to derive the solution to the other displacement u . However, this problem is very similar to the case of the pressure load on the surface. Actually, there are only some minor differences in the problem statement compared to the case of the pressure boundary condition:

1. The field variable in Eq. (3.23) is the displacement u instead of the displacement v in Eq. (3.8).
2. The transverse wave speed c_t in Eq. (3.23) replaces the longitudinal wave speed c_1 which was used in Eq. (3.8).

3. The boundary condition is now formulated in terms of σ_{xy} instead of σ_{yy} . The stress σ_{xy} is related to the displacement u by $\sigma_{xy} = \mu \frac{\partial u}{\partial y}$ (compare to Eqs. (3.6) and (3.7)).
4. The stress amplitude factor of the shear boundary condition is called Q_2 , while the respective factor corresponding to the pressure boundary condition was denoted as Q_1 .

Thus, the solution to the partial differential equation can be directly written by analogy to Eq. (3.18). This is

$$u(y, t) = \frac{c_t Q_2}{\mu} \int_{s=0}^{s=t-\frac{y}{c_t}} F(s) ds \quad (3.29)$$

$$\dot{u}(y, t) = \frac{c_t Q_2}{\mu} F\left(t - \frac{y}{c_t}\right). \quad (3.30)$$

3.1.1.3 Half-Space Subjected to a Uniform Pressure and a Uniform Shear Load

As mentioned earlier, the solution to the initial problem including both pressure and shear traction on the surface of the half-space (see Fig. 3.1) can be obtained by the superposition of the results for the two separated boundary conditions. This is possible because of the linearity of the investigated problem. Thus, the entire solution to the particle displacement field arising in a linear elastic half-space that is subjected to the boundary conditions (3.1) and (3.2) and that is initially at rest is given by

$$u(y, t) = \frac{c_t Q_2}{\mu} \int_{s=0}^{s=t-\frac{y}{c_t}} F(s) ds \quad (3.31)$$

$$v(y, t) = \frac{c_1 Q_1}{\lambda + 2\mu} \int_{s=0}^{s=t-\frac{y}{c_1}} F(s) ds \quad (3.32)$$

$$w(y, t) = 0. \quad (3.33)$$

The corresponding particle velocity field is

$$\dot{u}(y, t) = \frac{c_t Q_2}{\mu} F\left(t - \frac{y}{c_t}\right) \quad (3.34)$$

$$\dot{v}(y, t) = \frac{c_1 Q_1}{\lambda + 2\mu} F\left(t - \frac{y}{c_1}\right) \quad (3.35)$$

$$\dot{w}(y, t) = 0. \quad (3.36)$$

Clearly, this solution represents a plane elastic wave traveling in the positive y -direction. All field variables depend spatially only on the y -position. Exemplarily, these formulae are evaluated for a sinusoidal input signal $F(t)$ starting at $t = 0$, as given by

$$F(t) = \begin{cases} \sin(\omega t) & \text{for } t \geq 0 \\ 0 & \text{for } t < 0 \end{cases} \quad (3.37)$$

where $\omega = 2\pi f$ and f is the excitation frequency. Then, the expressions for the non-vanishing particle displacements and velocities become

$$u(y, t) = \begin{cases} \frac{Q_2}{k_t \mu} [1 - \cos(\omega t - k_t y)] & \text{for } t \geq \frac{y}{c_t} \\ 0 & \text{for } t < \frac{y}{c_t} \end{cases} \quad (3.38)$$

$$v(y, t) = \begin{cases} \frac{Q_1}{k_1(\lambda + 2\mu)} [1 - \cos(\omega t - k_1 y)] & \text{for } t \geq \frac{y}{c_1} \\ 0 & \text{for } t < \frac{y}{c_1} \end{cases} \quad (3.39)$$

$$\dot{u}(y, t) = \begin{cases} \frac{c_t Q_2}{\mu} \sin(\omega t - k_t y) & \text{for } t \geq \frac{y}{c_t} \\ 0 & \text{for } t < \frac{y}{c_t} \end{cases} \quad (3.40)$$

$$\dot{v}(y, t) = \begin{cases} \frac{c_1 Q_1}{\lambda + 2\mu} \sin(\omega t - k_1 y) & \text{for } t \geq \frac{y}{c_1} \\ 0 & \text{for } t < \frac{y}{c_1} \end{cases} \quad (3.41)$$

where k_1 and k_t denote the longitudinal and the transverse wavenumber.

Finally, the solution to the corresponding steady-state problem is presented here. Although this problem is more trivial than the transient one solved above and although the numerical solutions presented later in this thesis are transient, it is justified to show these solutions because they will be the base for the nonlinear steady-state solution derived in the next section.

Now, the boundary conditions applying are given by

$$\sigma_{yy}(x, y = 0, t) = -Q_1 \sin(\omega t) \quad (3.42)$$

$$\sigma_{xy}(x, y = 0, t) = -Q_2 \sin(\omega t) \quad (3.43)$$

for all t and the initial condition is that a steady-state has been reached. It is easy to show that the solutions to the displacement become

$$u_1(y, t) = -\frac{Q_2}{k_t \mu} \cos(\omega t - k_t y) + U_1 \quad (3.44)$$

$$v_1(y, t) = -\frac{Q_1}{k_1(\lambda + 2\mu)} \cos(\omega t - k_1 y) + V_1 \quad (3.45)$$

and the solutions to the particle velocity are

$$\dot{u}_1(y, t) = \frac{c_t Q_2}{\mu} \sin(\omega t - k_t y) \quad (3.46)$$

$$\dot{v}_1(y, t) = \frac{c_1 Q_1}{\lambda + 2\mu} \sin(\omega t - k_1 y). \quad (3.47)$$

The difference compared to the transient solution is that there is no effect of wave fronts traveling and that the displacements include arbitrary constant terms U_1 and V_1 , respectively.

3.1.2 Stress-Strain Relationship Including a Quadratic Nonlinearity

In this section, the half-space is subjected to the same boundary conditions (3.42) and (3.43) as above, but now, the constitutive equations describing the half-space's material are assumed to be nonlinear. More specifically, the quadratic terms occurring in the stress-strain relationship shall be taken into account in this section. The situation is depicted in Fig. 3.3. It has to be mentioned that the subsequent derivation will be limited to the steady-state solution in order to keep the nonlinear solution as simple as possible. The derivation presented in the following is based on [22]. The solution to the present nonlinear problem will have some similarities with the solution to the linear problem presented in the previous section. At first, the solution has to be again a plane wave traveling in the y -direction because the problem statement is

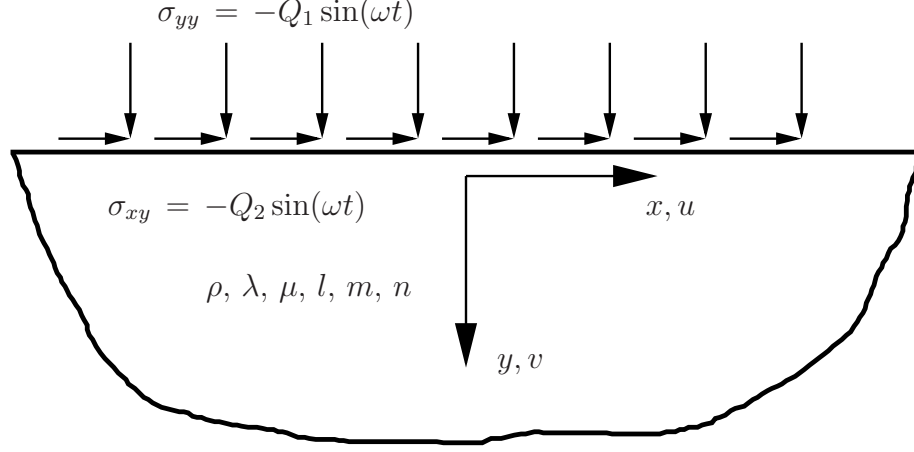


Figure 3.3: Nonlinear half-space subjected to a uniform harmonic pressure and shear load.

independent on the spatial coordinates x and z . This is the result of the boundary condition that is uniform on the whole surface of the half-space. Moreover, because of the symmetry of the half-space and the boundary conditions applied, there cannot be any particle displacement in the z -direction, this is $w(y, t) = 0$. It shall be pointed out that the displacement-strain relationship is still linear as given by Eq. (2.15). However, the nonlinear constitutive equations have to be derived according to (2.11) from the expression for the internal elastic energy density (2.12) which accounts for terms up to cubic order. In the present case, this expression can be simplified because some of the terms $u_{i,j}$ vanish because of the relatively simple geometry of this problem. Being more specific, this is because the displacement w vanishes as depicted above and because this is a one-dimensional problem what means that only the spatial derivatives with respect to y do not vanish. Thus, only the terms $\frac{\partial u}{\partial y}$ and $\frac{\partial v}{\partial y}$ in $u_{i,j}$ remain. Moreover, it can now be recognized from the compatibility equations (2.15) that ε_{xy} and ε_{yy} are the only strains that do not disappear. With this knowledge, the internal elastic energy density can be rewritten as

$$\Gamma = \frac{\lambda + 2\mu}{2} \varepsilon_{yy}^2 + 2\mu \varepsilon_{xy}^2 + \frac{l + 2m}{3} \varepsilon_{yy}^3 + 2m \varepsilon_{yy} \varepsilon_{xy}^2. \quad (3.48)$$

Plugging in the applying displacement-strain relationships (2.15) yields

$$\Gamma = \frac{\lambda + 2\mu}{2} \left(\frac{\partial v}{\partial y} \right)^2 + \frac{\mu}{2} \left(\frac{\partial u}{\partial y} \right)^2 + \frac{l + 2m}{3} \left(\frac{\partial v}{\partial y} \right)^3 + \frac{m}{2} \frac{\partial v}{\partial y} \left(\frac{\partial u}{\partial y} \right)^2. \quad (3.49)$$

The governing equations for this problem are the same ones as for the linear problem (2.6). For the two non-vanishing displacements u and v , they reduce in the absence of body forces to

$$\rho \frac{\partial^2 u}{\partial t^2} = \frac{\partial \sigma_{xy}}{\partial y} \quad (3.50)$$

$$\rho \frac{\partial^2 v}{\partial t^2} = \frac{\partial \sigma_{yy}}{\partial y}. \quad (3.51)$$

Therefore, the stresses σ_{xy} and σ_{yy} have to be computed now from (3.49) using Eq. (2.12). This yields

$$\sigma_{xy} = \frac{\partial \Gamma}{\partial \left(\frac{\partial u}{\partial y} \right)} = \mu \frac{\partial u}{\partial y} + m \frac{\partial u}{\partial y} \frac{\partial v}{\partial y} \quad (3.52)$$

$$\sigma_{yy} = \frac{\partial \Gamma}{\partial \left(\frac{\partial v}{\partial y} \right)} = (\lambda + 2\mu) \frac{\partial v}{\partial y} + (l + 2m) \left(\frac{\partial v}{\partial y} \right)^2 + \frac{m}{2} \left(\frac{\partial u}{\partial y} \right)^2. \quad (3.53)$$

These nonlinear constitutive equations are inserted into Eqs. (3.50) and (3.51) what results in the nonlinear displacement equations of motion

$$\frac{\partial^2 u}{\partial t^2} - c_t^2 \frac{\partial^2 u}{\partial y^2} = \gamma \frac{\partial}{\partial y} \left(\frac{\partial u}{\partial y} \frac{\partial v}{\partial y} \right) \quad (3.54)$$

$$\frac{\partial^2 v}{\partial t^2} - c_1^2 \frac{\partial^2 v}{\partial y^2} = \beta \frac{\partial v}{\partial y} \frac{\partial^2 v}{\partial y^2} + \frac{\gamma}{2} \frac{\partial}{\partial y} \left(\frac{\partial u}{\partial y} \right)^2 \quad (3.55)$$

where c_1 and c_t are defined as usual and the constants β and γ are given by

$$\beta = \frac{2(l + 2m)}{\rho} \quad (3.56)$$

$$\gamma = \frac{m}{\rho}. \quad (3.57)$$

Clearly, Eqs. (3.54) and (3.55) reduce to the linear displacement equations of motion (3.22) and (3.23) for $\beta = \gamma = 0$. Thus, the right sides may be considered as nonlinear correction terms that distinguish between the linear and the nonlinear

problem. An important difference between (3.54) and (3.55) shall be pointed out here: the right side of (3.54) differs from the linear problem only if both longitudinal and transverse displacements exist what means, for example, that the solution to the transverse displacement u for a plane wave created by a pure shear boundary condition would be identical in the linear and the nonlinear case. On the other hand, the nonlinear contribution on the right side of (3.55) contains a longitudinal and transverse term which are independent of each other.

An approximate solution to the partial differential equations (3.54) and (3.55) can be derived making use of the perturbation theory. This means that the nonlinear solution to the displacements u and v is assumed to have the following form,

$$u(y, t) = u_1(y, t) + u_2(y, t) \quad (3.58)$$

$$v(y, t) = v_1(y, t) + v_2(y, t) \quad (3.59)$$

where u_1 and v_1 are the solutions to the corresponding linear problem, while u_2 and v_2 are additive nonlinear corrections. The linear solutions to the displacements have been derived in the previous section and are stated by Eqs. (3.44) and (3.45). The approach (3.58), (3.59) can now be inserted into the displacement equations of motion

$$\begin{aligned} & \frac{\partial^2 u_1}{\partial t^2} + \frac{\partial^2 u_2}{\partial t^2} - c_t^2 \frac{\partial^2 u_1}{\partial y^2} - c_t^2 \frac{\partial^2 u_2}{\partial y^2} \\ = & \gamma \frac{\partial}{\partial y} \left[\left(\frac{\partial u_1}{\partial y} + \frac{\partial u_2}{\partial y} \right) \left(\frac{\partial v_1}{\partial y} + \frac{\partial v_2}{\partial y} \right) \right] \end{aligned} \quad (3.60)$$

$$\begin{aligned} & \frac{\partial^2 v_1}{\partial t^2} + \frac{\partial^2 v_2}{\partial t^2} - c_l^2 \frac{\partial^2 v_1}{\partial y^2} - c_l^2 \frac{\partial^2 v_2}{\partial y^2} \\ = & \beta \left(\frac{\partial v_1}{\partial y} + \frac{\partial v_2}{\partial y} \right) \left(\frac{\partial^2 v_1}{\partial y^2} + \frac{\partial^2 v_2}{\partial y^2} \right) + \frac{\gamma}{2} \frac{\partial}{\partial y} \left(\frac{\partial u_1}{\partial y} + \frac{\partial u_2}{\partial y} \right)^2. \end{aligned} \quad (3.61)$$

These longish equations can be rewritten in a simplified form. First, all terms on the left sides containing the partial solution u_1 (or v_1 , respectively) cancel out each other according to Eq. (3.23) (or (3.22), respectively). Furthermore, since small

displacements are assumed throughout this research, it is a reasonable approximation to neglect the small nonlinear correction terms u_2 and v_2 on the right sides that appear in a sum with the remaining much larger terms u_1 and v_1 . This yields the simplified displacement equations of motion

$$\frac{\partial^2 u_2}{\partial t^2} - c_t^2 \frac{\partial^2 u_2}{\partial y^2} = \gamma \frac{\partial}{\partial y} \left(\frac{\partial u_1}{\partial y} \frac{\partial v_1}{\partial y} \right) \quad (3.62)$$

$$\frac{\partial^2 v_2}{\partial t^2} - c_l^2 \frac{\partial^2 v_2}{\partial y^2} = \frac{\beta}{2} \frac{\partial}{\partial y} \left(\frac{\partial v_1}{\partial y} \right)^2 + \frac{\gamma}{2} \frac{\partial}{\partial y} \left(\frac{\partial u_1}{\partial y} \right)^2. \quad (3.63)$$

In this simpler form, the two partial differential equations for u_2 and v_2 , respectively, are independent of each other. The right sides turn out to be perturbation functions which are known since they contain only the solutions to the corresponding linear problem u_1 and v_1 . The neglecting of the correction terms on the right sides mentioned is equivalent to using the subsequent simplified constitutive equations,

$$\sigma_{xy} = \mu \frac{\partial u_1}{\partial y} + \mu \frac{\partial u_2}{\partial y} + m \frac{\partial u_1}{\partial y} \frac{\partial v_1}{\partial y} \quad (3.64)$$

$$\begin{aligned} \sigma_{yy} = & (\lambda + 2\mu) \frac{\partial v_1}{\partial y} + (\lambda + 2\mu) \frac{\partial v_2}{\partial y} \\ & + (l + 2m) \left(\frac{\partial v_1}{\partial y} \right)^2 + \frac{m}{2} \left(\frac{\partial u_1}{\partial y} \right)^2, \end{aligned} \quad (3.65)$$

where the expressions combining the third-order elastic constants and the higher-order displacement correction terms are disregarded. Equations (3.62) and (3.63) can be solved if the boundary conditions given by Eqs. (3.42) and (3.43). Note that only the steady-state problem is considered in this nonlinear case. In contrast to the different solutions to the linear problem in the previous section where it has been distinguished whether the wave fronts have already arrived at a specific point of the domain or not, the solution derived here will be only valid for the so-called steady state. More specifically, this means that all of the waves appearing are supposed to have already arrived at a respective point of consideration. The reason for this proceeding is to keep the derivation following as simple and clear as possible.

The complete solution to each of the two considered partial differential equations (3.62) and (3.63) is the superposition of the respective general solution to the homogeneous partial differential equation and a particular solution fulfilling the inhomogeneous equation. The general solution to the homogeneous one-dimensional wave equation has been already presented in Eq. (3.10). However, its second term describing waves traveling in negative direction is discarded here a priori for reasons of plausibility. The complete solution is presented without a more detailed mathematical derivation as

$$u_2(y, t) = f_1 \left(t - \frac{y}{c_t} \right) + C_1 \sin(2\omega t - (k_1 + k_t)y) - C_2 \sin((k_t - k_1)y) \quad (3.66)$$

$$C_1 = \frac{\gamma Q_1 Q_2 (k_1 + k_t)}{6 (\lambda + 2\mu) \mu k_1^2 \left(\frac{c_t}{3} + c_1 \right) (c_1 - c_t)} \quad (3.67)$$

$$C_2 = \frac{\gamma Q_1 Q_2 (k_t - k_1)}{2 (\lambda + 2\mu) \mu k_1^2 (c_1 - c_t)^2} \quad (3.68)$$

$$v_2(y, t) = f_2 \left(t - \frac{y}{c_1} \right) + C_3 y \cos(2(\omega t - k_1 y)) + C_4 \sin((k_t - k_1)y) \cos(2\omega t - (k_t + k_1)y) \quad (3.69)$$

$$C_3 = \frac{\beta Q_1^2}{8 c_1^2 (\lambda + 2\mu)^2} \quad (3.70)$$

$$C_4 = \frac{\gamma Q_2^2}{4 k_t \mu^2 (c_1^2 - c_t^2)}. \quad (3.71)$$

Clearly, the arbitrary functions f_1 and f_2 still have to be determined from the boundary conditions. Using Eqs. (3.64) and (3.65), these can be stated as

$$\left[\mu \frac{\partial u_1}{\partial y} + \mu \frac{\partial u_2}{\partial y} + m \frac{\partial u_1}{\partial y} \frac{\partial v_1}{\partial y} \right]_{y=0} = -Q_2 \sin(\omega t) \quad (3.72)$$

$$\left[(\lambda + 2\mu) \frac{\partial v_1}{\partial y} + (\lambda + 2\mu) \frac{\partial v_2}{\partial y} + (l + 2m) \left(\frac{\partial v_1}{\partial y} \right)^2 + \frac{m}{2} \left(\frac{\partial u_1}{\partial y} \right)^2 \right]_{y=0} = -Q_1 \sin(\omega t). \quad (3.73)$$

However, the linear solutions u_1 and v_1 have been already required in the previous derivation to fulfill the boundary conditions considered what means

$$\left[\mu \frac{\partial u_1}{\partial y} \right]_{y=0} = -Q_2 \sin(\omega t) \quad (3.74)$$

$$\left[(\lambda + 2\mu) \frac{\partial v_1}{\partial y} \right]_{y=0} = -Q_1 \sin(\omega t). \quad (3.75)$$

Thus, the nonlinear boundary conditions can be reduced by plugging in the linear boundary conditions to

$$\left[\mu \frac{\partial u_2}{\partial y} + m \frac{\partial u_1}{\partial y} \frac{\partial v_1}{\partial y} \right]_{y=0} = 0 \quad (3.76)$$

$$\left[(\lambda + 2\mu) \frac{\partial v_2}{\partial y} + (l + 2m) \left(\frac{\partial v_1}{\partial y} \right)^2 + \frac{m}{2} \left(\frac{\partial u_1}{\partial y} \right)^2 \right]_{y=0} = 0. \quad (3.77)$$

The unknown functions f_1 and f_2 can now be determined from these boundary conditions by inserting the complete solutions (3.66) and (3.69). The results are

$$f_1 \left(t - \frac{y}{c_t} \right) = -C_5 \sin(2(\omega t - k_t y)) + U_2 \quad (3.78)$$

$$C_5 = \frac{\gamma Q_1 Q_2 k_t}{3k_1^2 \mu (\lambda + 2\mu) \left(\frac{c_t}{3} + c_1 \right) (c_1 - c_t)} \quad (3.79)$$

$$f_2 \left(t - \frac{y}{c_1} \right) = -C_7 \sin(2(\omega t - k_1 y)) + C_8 \left(t - \frac{y}{c_1} \right) + V_2 \quad (3.80)$$

$$C_7 = \frac{\beta Q_1^2}{16k_1 c_1^2 (\lambda + 2\mu)^2} + \frac{\gamma Q_2^2 (k_t - k_1)}{8\mu^2 k_t^2 (c_1^2 - c_t^2)} \quad (3.81)$$

$$C_8 = \frac{\beta Q_1^2}{4c_1 (\lambda + 2\mu)^2} + \frac{\gamma Q_2^2}{4c_1 \mu^2} \quad (3.82)$$

where U_2 and V_2 are arbitrary constant displacements. The total steady-state solution to the displacements in the nonlinear half-space considered arising due to the harmonic traction boundary condition is according to the approximation given by

Eqs. (3.58) and (3.59)

$$u(y, t) = -\frac{Q_2}{k_t \mu} \cos(\omega t - k_t y) - C_5 \sin(2(\omega t - k_t y)) \\ + C_1 \sin(2\omega t - (k_1 + k_t)y) - C_2 \sin((k_t - k_1)y) + U \quad (3.83)$$

$$v(y, t) = -\frac{Q_1}{k_1(\lambda + 2\mu)} \cos(\omega t - k_1 y) - C_7 \sin(2(\omega t - k_1 y)) \\ + C_8 \left(t - \frac{y}{c_1}\right) + C_3 y \cos(2(\omega t - k_1 y)) \\ + C_4 \sin((k_t - k_1)y) \cos(2\omega t - (k_t + k_1)y) + V \quad (3.84)$$

where the arbitrary constant displacement terms $U = U_1 + U_2$ and $V = V_1 + V_2$ have been introduced. To conclude this derivation, the corresponding particle velocities are stated as

$$\dot{u}(y, t) = \frac{c_t Q_2}{\mu} \sin(\omega t - k_t y) - 2\omega C_5 \cos(2(\omega t - k_t y)) \\ + 2\omega C_1 \cos(2\omega t - (k_1 + k_t)y) \quad (3.85)$$

$$\dot{v}(y, t) = \frac{c_1 Q_1}{\lambda + 2\mu} \sin(\omega t - k_1 y) - 2\omega C_7 \cos(2(\omega t - k_1 y)) \\ + C_8 - 2\omega C_3 y \sin(2(\omega t - k_1 y)) \\ - 2\omega C_4 \sin((k_t - k_1)y) \sin(2\omega t - (k_t + k_1)y). \quad (3.86)$$

Finally, some remarks concerning the validity of the analytical solutions derived shall be given. Unfortunately, there are some restrictions since several assumptions have been made in the process of the derivation. First of all, the solutions presented represent only the relatively easy case of an steady state. This means that it is only valid at a specific point of the domain considered if all of the waves involved have arrived this point and the respective wave fronts have already reached a sufficiently large distance from it. Clearly, one has to consider this fact if the analytical solutions stated are to be used to interpret wave fields arising due to an input signal that has not infinite length. Another point that should be recalled is the circumstance that only the small strain tensor has been applied instead of the finite strain tensor. As described in Section 2.3, this approach is, of course, only valid if only sufficiently

small strains occur in the domain considered. This can be made sure if the traction amplitudes Q_1 and Q_2 applied at the boundary are limited to an appropriate value. Another restriction has been imposed on the solutions derived by making use of the perturbation approach in Eqs. (3.58) and (3.59). This approach inherently implies that the nonlinear solution is basically close to the linear one except of specific correction terms which are assumed to be small compared to the linear solution. Thus, it has to be concluded that the approximate solutions derived are only close to the actual wave field developing as long as the correction terms u_2 and v_2 are actually very small compared to u_1 and v_1 , respectively. However, if the correction terms reach orders of magnitude that cannot be considered small compared to the linear solutions anymore, the perturbation solution will probably be a bad approximation to the actual wave field. This problem can be avoided if the input traction amplitudes Q_1 and Q_2 are chosen to be sufficiently small because all of the terms occurring in u_2 and v_2 depend quadratically on the traction amplitudes. Thus, it can always be guaranteed that the correction terms are small compared to the linear solution by an appropriate choice of the input parameters but clearly, in a practical problem, it will not be possible to decrease Q_1 and Q_2 arbitrarily because this would lead to low signal-to-noise ratios both in experiments and simulations. Thus, it has to be kept in mind that the nonlinear solutions derived in this section are just approximate solutions that are only valid for certain circumstances.

3.2 Half-Space Subjected to a Uniform Line Load

3.2.1 Linear Stress-Strain Relationship

In this section, wave propagation in an elastic half-space is investigated that is excited by a line load as depicted in Fig. 3.4, where $F(t)$ may be an arbitrary dimensionless function of time and Q an amplitude stress. In this case, the line load generates a deformation in plane strain. Therefore, this is a two-dimensional problem and the

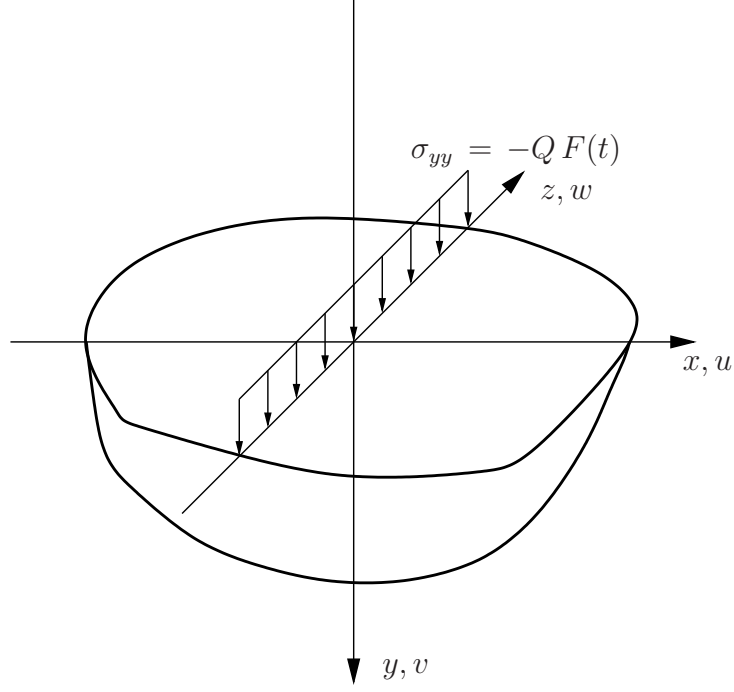


Figure 3.4: Half-space subjected to line load.

solution will not depend on the coordinate z . For convenience, the notation will be adapted to the coordinate system shown in Fig. 3.4 which was also done in the previous sections. Thus, the displacements in x - and y -direction will be denoted again $u(x, y, t)$ and $v(x, y, t)$, respectively, instead of $u_1(x_1, x_2, t)$ and $u_2(x_1, x_2, t)$. Corresponding notation is applied to the other field variables. Obviously, the boundary conditions for this problem are given by

$$\sigma_{yy}(x, y = 0, t) = -QF(t)\delta(x) \quad (3.87)$$

$$\sigma_{xy}(x, y = 0, t) = \sigma_{yx}(x, y = 0, t) = 0. \quad (3.88)$$

The half-space is assumed to be initially at rest which means that the initial conditions can be stated as

$$u(x, y, t = 0) = v(x, y, t = 0) = 0 \quad (3.89)$$

$$\dot{u}(x, y, t = 0) = \dot{v}(x, y, t = 0) = 0. \quad (3.90)$$

In the linear case, that is, if both material and geometric nonlinearities are neglected, this problem was analytically solved by H. Lamb in a very detailed manner [15]. Thus, it is also known as *Lamb's problem* and its solution can be also found in [19] or [1]. A short version of that solution will be given in the following part of this chapter. The analytical solution to the linear case begins with the governing equations (2.7) that can be rewritten for the two-dimensional case in absence of body forces as

$$\frac{\partial \sigma_{xx}}{\partial x} + \frac{\partial \sigma_{yx}}{\partial y} = \rho \ddot{u} \quad (3.91)$$

$$\frac{\partial \sigma_{xy}}{\partial x} + \frac{\partial \sigma_{yy}}{\partial y} = \rho \ddot{v} \quad (3.92)$$

Plugging in Hooke's law (2.10) and the linear strain-displacement relationship (2.14) yields

$$\mu \left(\frac{\partial^2 u}{\partial x^2} + \frac{\partial^2 u}{\partial y^2} \right) + (\lambda + \mu) \left(\frac{\partial^2 u}{\partial x^2} + \frac{\partial^2 v}{\partial x \partial y} \right) = \rho \ddot{u} \quad (3.93)$$

$$\mu \left(\frac{\partial^2 v}{\partial x^2} + \frac{\partial^2 v}{\partial y^2} \right) + (\lambda + \mu) \left(\frac{\partial^2 u}{\partial x \partial y} + \frac{\partial^2 v}{\partial y^2} \right) = \rho \ddot{v}. \quad (3.94)$$

These two coupled partial differential equations can now be separated by applying the Helmholtz decomposition presented in Eq. (2.19). In this case of plane strain, the displacement potentials take the simpler form

$$\varphi = \varphi(x, y, t) \quad \text{and} \quad \boldsymbol{\psi} = \begin{bmatrix} 0 \\ 0 \\ \psi(x, y, t) \end{bmatrix} \quad (3.95)$$

so that no additional constraint is necessary (see Section 2.5). The result yields the two uncoupled partial differential equations in terms of the displacement potentials

$$\frac{\partial^2 \varphi}{\partial x^2} + \frac{\partial^2 \varphi}{\partial y^2} = \frac{1}{c_1^2} \frac{\partial^2 \varphi}{\partial t^2} \quad (3.96)$$

$$\frac{\partial^2 \psi}{\partial x^2} + \frac{\partial^2 \psi}{\partial y^2} = \frac{1}{c_t^2} \frac{\partial^2 \psi}{\partial t^2}. \quad (3.97)$$

The goal of this chapter is a relatively quick solution to these differential equations using the initial and boundary conditions stated above. This solution is based on that one given in [19] where additional information may be found.

3.2.2 Transformed Solution

The first step of the presented solution is the application of the one-sided Laplace transformation to Eqs. (3.96) and (3.97) with respect to the time variable t . The Laplace transform and its inverse are given by

$$\bar{f}(p) = \int_0^{\infty} f(t) e^{-pt} dt \quad (3.98a)$$

$$f(t) = \frac{1}{2\pi i} \int_{\gamma-i\infty}^{\gamma+i\infty} \bar{f}(p) e^{pt} dp. \quad (3.98b)$$

It should be mentioned that p is a complex variable in general. This yields

$$\frac{\partial^2 \bar{\varphi}}{\partial x^2} + \frac{\partial^2 \bar{\varphi}}{\partial y^2} = \frac{1}{c_1^2} p^2 \bar{\varphi} \quad (3.99)$$

$$\frac{\partial^2 \bar{\psi}}{\partial x^2} + \frac{\partial^2 \bar{\psi}}{\partial y^2} = \frac{1}{c_t^2} p^2 \bar{\psi}, \quad (3.100)$$

where $\bar{\varphi} = \bar{\varphi}(x, y, p)$ and $\bar{\psi} = \bar{\psi}(x, y, p)$. It was used that $\varphi(x, y, t = 0) = \dot{\varphi}(x, y, t = 0) = 0$ and $\psi(x, y, t = 0) = \dot{\psi}(x, y, t = 0) = 0$ what is true since the initial conditions (3.89) have to be satisfied.

Now, the exponential Fourier transform is applied to the obtained result with respect to the spatial coordinate x . The definition of the Fourier transform used here and its inverse are given by

$$\hat{f}(\xi) = \int_{-\infty}^{\infty} f(x) e^{-i\xi x} dx \quad (3.101a)$$

$$f(x) = \frac{1}{2\pi} \int_{-\infty}^{\infty} \hat{f}(\xi) e^{i\xi x} d\xi \quad (3.101b)$$

where the transformation variable ξ is real. The double-transformed equations

$$-\xi^2 \hat{\hat{\varphi}} + \frac{\partial^2 \hat{\hat{\varphi}}}{\partial y^2} = \frac{1}{c_1^2} p^2 \hat{\hat{\varphi}} \quad (3.102)$$

$$-\xi^2 \hat{\hat{\psi}} + \frac{\partial^2 \hat{\hat{\psi}}}{\partial y^2} = \frac{1}{c_t^2} p^2 \hat{\hat{\psi}}, \quad (3.103)$$

where $\hat{\bar{\varphi}} = \hat{\bar{\varphi}}(\xi, y, p)$ and $\hat{\bar{\psi}} = \hat{\bar{\psi}}(\xi, y, p)$ are obtained using the fact that

$$\begin{aligned} \lim_{x \rightarrow \infty} \bar{\varphi} &\rightarrow 0, & \lim_{x \rightarrow \infty} \frac{\partial \bar{\varphi}}{\partial x} &\rightarrow 0 \\ \text{and} \quad \lim_{x \rightarrow \infty} \bar{\psi} &\rightarrow 0, & \lim_{x \rightarrow \infty} \frac{\partial \bar{\psi}}{\partial x} &\rightarrow 0. \end{aligned}$$

Equations (3.102) and (3.103) represent two ordinary linear differential equations and can be rewritten as

$$\frac{\partial^2 \hat{\bar{\varphi}}}{\partial y^2} - \overbrace{\left(\xi^2 + \frac{p^2}{c_1^2} \right)}^{\alpha_1^2} \hat{\bar{\varphi}} = 0 \quad (3.104)$$

$$\frac{\partial^2 \hat{\bar{\psi}}}{\partial y^2} - \underbrace{\left(\xi^2 + \frac{p^2}{c_t^2} \right)}_{\alpha_t^2} \hat{\bar{\psi}} = 0. \quad (3.105)$$

The complete solutions to these two differential equations can be easily found to be

$$\hat{\bar{\varphi}}(\xi, y, p) = A(\xi, p) e^{-\alpha_1 y} + C(\xi, p) e^{\alpha_1 y} \quad (3.106)$$

$$\hat{\bar{\psi}}(\xi, y, p) = B(\xi, p) e^{-\alpha_t y} + D(\xi, p) e^{\alpha_t y} \quad (3.107)$$

where the terms $A(\xi, p)$, $B(\xi, p)$, $C(\xi, p)$ and $D(\xi, p)$ still have to be determined from the boundary conditions. From here on, for convenience, these terms will be just denoted as A, B, C and D .

However, in this case, it is sufficient to consider only real and positive values for the Laplace transformation variable p so that it is possible to select only the real and positive branches of α_1 and α_t . Specific explanation and links to the mathematical proofs are given in [19]. Therefore, since the displacement potentials have to vanish for $y \rightarrow \infty$, it can be concluded that $C = D = 0$. Thus, they can be rewritten here as

$$\hat{\bar{\varphi}}(\xi, y, p) = A e^{-\alpha_1 y} \quad (3.108)$$

$$\hat{\bar{\psi}}(\xi, y, p) = B e^{-\alpha_t y}. \quad (3.109)$$

Before the boundary conditions (3.87), given in terms of stresses, can be used for the determination of A and B , they have to be transformed in the same way as the displacement potentials,

$$\hat{\hat{\sigma}}_{yy}(\xi, y=0, p) = -Q\bar{F}(p) \quad (3.110)$$

$$\hat{\hat{\sigma}}_{xy}(\xi, y=0, p) = 0. \quad (3.111)$$

Formulas for the stresses σ_{yy} and σ_{xy} in dependence of the displacement potentials can be found by inserting the Helmholtz decomposition (2.19) in Eq. (2.10),

$$\begin{aligned} \sigma_{yy}(x, y, t) &= \lambda \nabla^2 \varphi + 2\mu \left[\frac{\partial^2 \varphi}{\partial y^2} - \frac{\partial}{\partial y} \left(\frac{\partial \psi}{\partial x} \right) \right] \\ &= \frac{\lambda}{c_1^2} \frac{\partial^2 \varphi}{\partial t^2} + 2\mu \left[\frac{\partial^2 \varphi}{\partial y^2} - \frac{\partial^2 \psi}{\partial x \partial y} \right] \end{aligned} \quad (3.112)$$

$$\begin{aligned} \sigma_{xy}(x, y, t) &= \mu \left[2 \frac{\partial^2 \varphi}{\partial x \partial y} + \frac{\partial}{\partial y} \left(\frac{\partial \psi}{\partial y} \right) - \frac{\partial}{\partial x} \left(\frac{\partial \psi}{\partial x} \right) \right] \\ &= \mu \left[2 \frac{\partial^2 \varphi}{\partial x \partial y} + 2 \frac{\partial^2 \psi}{\partial y^2} - \frac{1}{c_t^2} \frac{\partial^2 \psi}{\partial t^2} \right] \end{aligned} \quad (3.113)$$

where Eqs. (3.96) and (3.97) have been used. If both the Laplace transform and the Fourier transform are applied as above, the double-transformed stresses $\hat{\hat{\sigma}}_{yy}$ and $\hat{\hat{\sigma}}_{xy}$ become

$$\hat{\hat{\sigma}}_{yy}(\xi, y, p) = \frac{\lambda p^2}{c_1^2} \hat{\hat{\varphi}} + 2\mu \left[\frac{\partial^2 \hat{\hat{\varphi}}}{\partial y^2} - i\xi \frac{\partial \hat{\hat{\psi}}}{\partial y} \right] \quad (3.114)$$

$$\hat{\hat{\sigma}}_{xy}(\xi, y, p) = \mu \left[2i\xi \frac{\partial \hat{\hat{\varphi}}}{\partial y} + 2 \frac{\partial^2 \hat{\hat{\psi}}}{\partial y^2} - \frac{p^2}{c_t^2} \hat{\hat{\psi}} \right]. \quad (3.115)$$

Now, Eqs. (3.110) and (3.111) can be evaluated by inserting the stress-potential relationships (3.114), (3.115) and the general solution for the double-transformed potentials (3.108), (3.109) which yields the two equations

$$\frac{\lambda p^2}{c_1^2} A + 2\mu [\alpha_1^2 A + i\xi \alpha_t B] = -Q\bar{F}(p) \quad (3.116)$$

$$-2i\xi \alpha_1 A + 2\alpha_t^2 B - \frac{p^2}{c_t^2} B = 0. \quad (3.117)$$

This system of equations which is linear in A and B can be solved as usual. The result is

$$A(\xi, p) = -\frac{Q\bar{F}(p)}{\mu} \frac{\frac{p^2}{c_t^2} + 2\xi^2}{R(\xi, p)} \quad (3.118)$$

$$B(\xi, p) = -\frac{Q\bar{F}(p)}{\mu} \frac{2i\xi\alpha_1}{R(\xi, p)}, \quad (3.119)$$

where

$$R(\xi, p) = \xi^4 \left[\left(\frac{p^2}{c_t^2 \xi^2} + 2 \right)^2 - 4 \sqrt{1 + \frac{p^2}{c_1^2 \xi^2}} \sqrt{1 + \frac{p^2}{c_t^2 \xi^2}} \right]. \quad (3.120)$$

Obviously, the term $R(\xi, p)$ has a considerable similarity to the so-called Rayleigh equation. It is stated in [1] or [19] as

$$\left(2 - \frac{c^2}{c_t^2} \right)^2 - 4 \sqrt{1 - \frac{c^2}{c_1^2}} \sqrt{1 - \frac{c^2}{c_t^2}} = 0 \quad (3.121)$$

and is satisfied for $c = \pm c_r$, where c_r is the speed of propagation of the Rayleigh surface wave. By inspection, it can be concluded now that Eq. (3.120) has zeros if

$$\frac{p^2}{\xi^2} = -c_r^2. \quad (3.122)$$

Thus, the double-transformed solution to this problem is now completely determined in terms of the displacement potentials. However, it is more convenient to present it in terms of displacements, so the relevant components of Eq. (2.19) are also subjected to both a Laplace and a Fourier transform, resulting in

$$\hat{u}(\xi, y, p) = i\xi \hat{\varphi} + \frac{\partial \hat{\psi}}{\partial y} \quad (3.123)$$

$$\hat{v}(\xi, y, p) = \frac{\partial \hat{\varphi}}{\partial y} - i\xi \hat{\psi} \quad (3.124)$$

or, with the double-transformed displacement potentials (3.108) and (3.109), in

$$\hat{u}(\xi, y, p) = i\xi A e^{-\alpha_1 y} - \alpha_t B e^{-\alpha_t y} \quad (3.125)$$

$$\hat{v}(\xi, y, p) = -\alpha_1 A e^{-\alpha_1 y} - i\xi B e^{-\alpha_t y}. \quad (3.126)$$

3.2.3 Cagniard-deHoop Inversion of the Transformed Solution

The evaluation of the inverse transformations that have to be applied to Eqs. (3.125) and (3.126) in order to obtain a solution $u(x, y, t)$ and $v(x, y, t)$ is a major part of the approach presented here. Formal application of the inverse Fourier transform (3.101b) yields

$$\begin{aligned} \begin{bmatrix} \bar{u}(x, y, p) \\ \bar{v}(x, y, p) \end{bmatrix} &= \frac{1}{2\pi} \int_{-\infty}^{\infty} \begin{bmatrix} \hat{u}(x, y, p) \\ \hat{v}(x, y, p) \end{bmatrix} e^{-i\xi x} d\xi \\ &= \frac{Q\bar{F}(p)}{2\pi\mu} \int_{-\infty}^{\infty} \begin{bmatrix} \frac{-i\xi \left(2\xi^2 + \frac{p^2}{c_t^2}\right) e^{-\alpha_1 y} e^{i\xi x}}{R(\xi, p)} + \frac{2i\xi \alpha_1 \alpha_t e^{-\alpha_t y} e^{i\xi x}}{R(\xi, p)} \\ \frac{\alpha_1 \left(2\xi^2 + \frac{p^2}{c_t^2}\right) e^{-\alpha_1 y} e^{i\xi x}}{R(\xi, p)} - \frac{2\xi^2 \alpha_1 e^{-\alpha_t y} e^{i\xi x}}{R(\xi, p)} \end{bmatrix} d\xi. \end{aligned} \quad (3.127)$$

The next step is the introduction of a new variable

$$\eta = \frac{\xi}{p}, \quad (3.128)$$

which is real since ξ is real and p has been considered as real and positive. Additionally, for an easier notation, the slownesses s_1 and s_t will be used which are defined as

$$s_1 = \frac{1}{c_1} \quad \text{and} \quad s_t = \frac{1}{c_t}.$$

Then, after some mathematical manipulation, Eq. (3.127) may be written in terms of the new variable η as

$$\begin{bmatrix} \bar{u}(x, y, p) \\ \bar{v}(x, y, p) \end{bmatrix} = \frac{Q\bar{F}(p)}{2\pi\mu} \int_{-\infty}^{\infty} \begin{bmatrix} f_1(\eta) e^{-pg_1(\eta)} + f_t(\eta) e^{-pg_t(\eta)} \\ h_1(\eta) e^{-pg_1(\eta)} + h_t(\eta) e^{-pg_t(\eta)} \end{bmatrix} d\eta \quad (3.129)$$

where the definitions for the newly introduced terms are given by

$$g_1(\eta) = \sqrt{\eta^2 + s_1^2} y - i\eta x, \quad (3.130)$$

$$g_t(\eta) = \sqrt{\eta^2 + s_t^2} y - i\eta x, \quad (3.131)$$

$$f_1(\eta) = -\frac{i\eta(2\eta^2 + s_t^2)}{\tilde{R}(\eta)}, \quad (3.132)$$

$$f_t(\eta) = \frac{2i\eta\sqrt{\eta^2 + s_1^2}\sqrt{\eta^2 + s_t^2}}{\tilde{R}(\eta)}, \quad (3.133)$$

$$h_1(\eta) = \frac{\sqrt{\eta^2 + s_1^2}(2\eta^2 + s_t^2)}{\tilde{R}(\eta)}, \quad (3.134)$$

$$h_t(\eta) = -\frac{2\eta^2\sqrt{\eta^2 + s_1^2}}{\tilde{R}(\eta)} \quad (3.135)$$

and

$$\tilde{R}(\eta) = (2\eta^2 + s_t^2)^2 - 4\eta^2\sqrt{\eta^2 + s_1^2}\sqrt{\eta^2 + s_t^2}. \quad (3.136)$$

With the same argument as before, $\tilde{R}(\eta)$ becomes zero if

$$\eta^2 = -c_r^2. \quad (3.137)$$

The evaluation of Eq. (3.129) can be done by the application of the Cagniard-deHoop method. Its basic idea is to separate the integral in Eq. (3.129) into a part that has the term $g_1(\eta)$ in its exponent and a part that has the term $g_t(\eta)$ in its exponent. Then, separately for both parts, the path of integration will be deformed off the real axis (from $-\infty$ to ∞) by setting $g_1(\eta) = t$ and $g_t(\eta) = t$, respectively, where the variable t is real and positive. This separation can be stated as

$$\begin{bmatrix} \bar{u}(x, y, p) \\ \bar{v}(x, y, p) \end{bmatrix} = \int_{-\infty}^{\infty} [\mathbf{f}_1(\eta) + \mathbf{f}_t(\eta)] d\eta \quad (3.138)$$

where

$$\mathbf{f}_1(\eta) = \frac{Q\bar{F}(p)}{2\pi\mu} \begin{bmatrix} f_1(\eta) \\ h_1(\eta) \end{bmatrix} e^{-pg_1(\eta)} \quad \text{and} \quad \mathbf{f}_t(\eta) = \frac{Q\bar{F}(p)}{2\pi\mu} \begin{bmatrix} f_t(\eta) \\ h_t(\eta) \end{bmatrix} e^{-pg_t(\eta)}.$$

For the integration along those deformed paths in the complex plane, branch cuts and poles of the functions $f_1(\eta)$, $h_1(\eta)$, $g_1(\eta)$ or $f_t(\eta)$, $h_t(\eta)$, $g_t(\eta)$, respectively, have

to be considered. The functions $f_l(\eta)$, $h_l(\eta)$, $f_t(\eta)$ and $h_t(\eta)$ have branch points at $\eta = \pm is_l$ and $\eta = \pm is_t$ as well as simple poles at $\eta = \pm is_r$ where the slowness of the Rayleigh surface wave s_r is defined as

$$s_r = \frac{1}{c_r}.$$

On the other hand, the term $g_l(\eta)$ has branch points at $\eta = \pm is_l$, while $g_t(\eta)$ has those at $\eta = \pm is_t$. Both the branch cuts and the poles are marked in the complex η -plane in Fig. 3.5. Additionally, a closed path of integration is shown there. This path does neither surround or touch any pole nor cross one of the depicted branch cuts. Thus, it can be stated

$$\int_{C_1} \mathbf{f}(\eta) d\eta + \int_{C_2} \mathbf{f}(\eta) d\eta - \int_{C_4} \mathbf{f}(\eta) d\eta + \int_{C_5} \mathbf{f}(\eta) d\eta - \int_{C_3} \mathbf{f}(\eta) d\eta = 0 \quad (3.139)$$

where $\mathbf{f}(\eta)$ represents either one of the two summands of the integrand in Eq. (3.138). However, it is shown in [19] that, for $x > 0$ and $y \geq 0$, Jordan's lemma may be applied to the integrals over the circular paths C_2 and C_3 . Specifically, this means that these integrals will vanish if $R \rightarrow \infty$. From this fact, it follows that Eq. (3.139) becomes

$$\int_{-\infty}^{\infty} \mathbf{f}(\eta) d\eta = \int_{C_4} \mathbf{f}(\eta) d\eta - \int_{C_5} \mathbf{f}(\eta) d\eta = \int_{C_4 - C_5} \mathbf{f}(\eta) d\eta \quad (3.140)$$

where the path $C_4 - C_5$ is basically arbitrary but has to satisfy certain conditions. First, it has to start at infinity in the second quadrant and end at infinity in the first quadrant. Moreover, as shown in Fig. 3.5, it has to cross the imaginary axis at any point between $\eta = 0$ and $\eta = is_l$, where the last one is excluded. As mentioned before, the evaluation of the integrals over the two summands in Eq. (3.129) is done by separating the integral into two parts. Thus, the first term which is given by

$$\begin{bmatrix} \bar{u}_l(x, y, p) \\ \bar{v}_l(x, y, p) \end{bmatrix} = \frac{Q\bar{F}(p)}{2\pi\mu} \int_{-\infty}^{\infty} \begin{bmatrix} f_l(\eta) \\ h_l(\eta) \end{bmatrix} e^{-pg_l(\eta)} d\eta \quad (3.141)$$

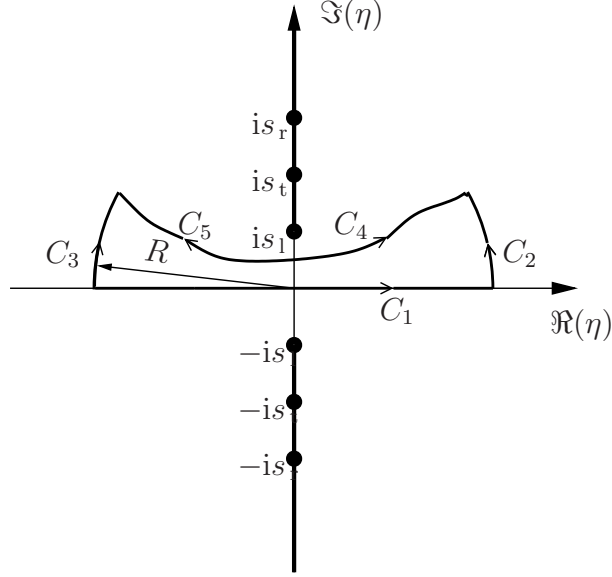


Figure 3.5: Paths of integration used in the Cagniard-deHoop method.

will be analyzed in the following. At first, as already stated, the term in the exponent $g_1(\eta)$ will be set equal to t which is real and positive. As it be seen later, doing so corresponds to a deformation of the original path to an equivalent path $-C_5 + C_4$ as shown in Fig. 3.5. Plugging in the definition of $g_1(\eta)$ leads to

$$t = \sqrt{\eta^2 + s_1^2} y - i\eta x. \quad (3.142)$$

Because of the cylindrical nature of Lamb's problem, polar coordinates are introduced now in order to accomplish a simpler statement of the following equations. The polar coordinates that shall be used here are shown in Fig. 3.6 and can be obtained from the Cartesian coordinates used so far by

$$\begin{aligned} r &= \sqrt{x^2 + y^2} & 0 \leq r < \infty \\ \theta &= \arctan\left(\frac{x}{y}\right) & -\frac{\pi}{2} \leq \theta \leq \frac{\pi}{2}. \end{aligned}$$

This yields

$$t = \sqrt{\eta^2 + s_1^2} r \cos(\theta) - i\eta r \sin(\theta) \quad (3.143)$$

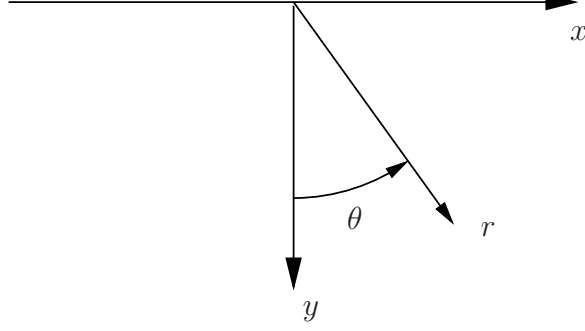


Figure 3.6: Definition of the introduced polar coordinates r and θ .

what can be solved for $\eta_{1\pm}$, the new path of integration in the complex η -plane,

$$\eta_{1\pm}(t) = \pm \sqrt{\frac{t^2}{r^2} - s_1^2} \cos(\theta) + \frac{it}{r} \sin(\theta) \quad s_1 \leq \frac{t}{r} \leq \infty. \quad (3.144)$$

However, the angle θ can be limited to the range $0 \leq \theta \leq \frac{\pi}{2}$ because the physical problem is symmetrical with respect to the y -axis. This limitation means that the hyperbola given by Eq. (3.144) is always located in the upper half of the complex η -plane; for negative values of θ , it would lie in the lower half. This path of integration satisfies the conditions stated above, i.e. it goes to infinity in both the first and the second quadrant. Moreover, as it can be seen in Fig. 3.7 it cuts the imaginary axis at $\eta_1(t = rs_1) = i s_1 \sin(\theta)$ what fulfills $\Im(\eta) \geq 0$ and $\Im(\eta) < s_1$ except for $\theta = \pi/2$. Thus, positions on the free surface of the half-space are excluded for the subsequent investigation and will be considered separately later on.

The next step after this preparatory work is rewriting the integral (3.141) with the help of (3.140) which yields

$$\begin{aligned} \begin{bmatrix} \bar{u}_1(x, y, p) \\ \bar{v}_1(x, y, p) \end{bmatrix} = & \frac{Q\bar{F}(p)}{2\pi\mu} \int_{\eta_{1+}} \begin{bmatrix} f_1(\eta) \\ h_1(\eta) \end{bmatrix} e^{-pg_1(\eta)} d\eta \\ & - \frac{Q\bar{F}(p)}{2\pi\mu} \int_{\eta_{1-}} \begin{bmatrix} f_1(\eta) \\ h_1(\eta) \end{bmatrix} e^{-pg_1(\eta)} d\eta \end{aligned} \quad (3.145)$$

where the new paths of integration given by (3.144) were used. Now, the variable of integration η in the second integral term is replaced by $-\bar{\eta}$, where $\bar{\eta}$ shall denote the

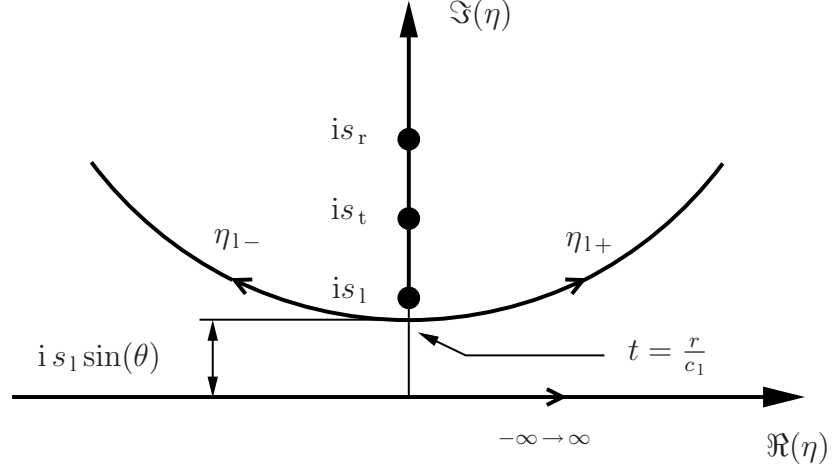


Figure 3.7: Equivalent path of integration for the longitudinal part.

complex conjugate of η ,

$$\begin{aligned} \begin{bmatrix} \bar{u}_1(x, y, p) \\ \bar{v}_1(x, y, p) \end{bmatrix} &= \frac{Q\bar{F}(p)}{2\pi\mu} \int_{\eta_{1+}} \begin{bmatrix} f_1(\eta) \\ h_1(\eta) \end{bmatrix} e^{-pg_1(\eta)} d\eta \\ &+ \frac{Q\bar{F}(p)}{2\pi\mu} \int_{\eta_{1-}} \begin{bmatrix} f_1(-\bar{\eta}) \\ h_1(-\bar{\eta}) \end{bmatrix} e^{-pg_1(-\bar{\eta})} d\bar{\eta}. \end{aligned} \quad (3.146)$$

Now, simple inserting shows that the following relations hold,

$$\begin{aligned} g_1(-\bar{\eta}) &= \overline{g_1(\eta)} \\ f_1(-\bar{\eta}) &= \overline{f_1(\eta)} \\ h_1(-\bar{\eta}) &= \overline{h_1(\eta)} \end{aligned} \quad (3.147)$$

where the bar again denotes the complex conjugate. Using these relations, it is possible to express the second integral in (3.146) also in terms of the path η_{1+} ,

yielding

$$\begin{aligned}
\begin{bmatrix} \bar{u}_1(x, y, p) \\ \bar{v}_1(x, y, p) \end{bmatrix} &= \frac{Q\bar{F}(p)}{2\pi\mu} \int_{\eta_{1+}} \begin{bmatrix} f_1(\eta) \\ h_1(\eta) \end{bmatrix} e^{-pg_1(\eta)} d\eta \\
&+ \frac{Q\bar{F}(p)}{2\pi\mu} \int_{\eta_{1-}} \begin{bmatrix} \overline{f_1(\eta)} \\ \overline{h_1(\eta)} \end{bmatrix} e^{-p\overline{g_1(\eta)}} d\bar{\eta} \\
&= \frac{Q\bar{F}(p)}{2\pi\mu} \int_{\eta_{1+}} \begin{bmatrix} f_1(\eta) \\ h_1(\eta) \end{bmatrix} e^{-pg_1(\eta)} d\eta \\
&+ \frac{Q\bar{F}(p)}{2\pi\mu} \int_{\eta_{1+}} \begin{bmatrix} \overline{f_1(\eta)} \\ \overline{h_1(\eta)} \end{bmatrix} e^{-p\overline{g_1(\eta)}} d\eta \\
&= \frac{Q\bar{F}(p)}{\pi\mu} \int_{\eta_{1+}} \Re \left\{ \begin{bmatrix} f_1(\eta) \\ h_1(\eta) \end{bmatrix} e^{-pg_1(\eta)} d\eta \right\}. \tag{3.148}
\end{aligned}$$

The next step is to replace the variable of integration η by t which can be reached by plugging in both the relation $g_1(\eta) = t$ that was chosen earlier and the relation between t and η_{1+} that is given by (3.144). The result is

$$\begin{bmatrix} \bar{u}_1(x, y, p) \\ \bar{v}_1(x, y, p) \end{bmatrix} = \frac{Q\bar{F}(p)}{\pi\mu} \int_{r s_1}^{\infty} \Re \left\{ \begin{bmatrix} f_1(\eta_{1+}(t)) \\ h_1(\eta_{1+}(t)) \end{bmatrix} \frac{d\eta_{1+}}{dt} \right\} e^{-pt} dt. \tag{3.149}$$

This process will now be repeated for the second summand in the integrand of Eq. (3.129). Since some steps will be very similar to the corresponding steps for the first summand, an abbreviated approach is presented in the following.

In this case, again, the term appearing in the exponent g_t is set equal to t what yields the two relations for t and η

$$t = \sqrt{\eta^2 + s_1^2} r \cos(\theta) - i\eta r \sin(\theta) \tag{3.150}$$

$$\eta_{t\pm}(t) = \pm \sqrt{\frac{t^2}{r^2} - s_t^2} \cos(\theta) + \frac{it}{r} \sin(\theta) \quad s_t \leq \frac{t}{r} \leq \infty. \tag{3.151}$$

For reasons of symmetry, as above, the domain investigated here can be restricted to angles $0 \leq \theta < \frac{\pi}{2}$. The free surface is again excluded. Then, (3.151) represents the

branch of a hyperbola lying in the upper half of the complex η -plane. However, in this case, the new path of integration cuts the imaginary axis at $\eta = is_t \sin(\theta)$. This means that for some of the considered angles θ the path intersects the branch cut. Thus, the further investigation has to be split into two cases. In the first one, the path $\eta_{t+} - \eta_{t-}$ passes the imaginary axes below the branch cut, exactly as the the path $\eta_{1+} - \eta_{1-}$ does in Fig. 3.7. The condition for this case to occur is $s_t \sin(\theta) < s_1$, or

$$\theta < \theta_{\text{cr}} \quad \text{where} \quad \theta_{\text{cr}} = \arcsin\left(\frac{s_1}{s_t}\right). \quad (3.152)$$

Clearly, this case for the range $0 \leq \theta < \theta_{\text{cr}}$ will be somewhat similar to the solution to the first summand in Eq. (3.138). The second case is then obviously given by the range $\theta_{\text{cr}} \leq \theta < \frac{\pi}{2}$ and will be more complex because there, the path of integration intersects a branch cut.

As already mentioned above, the solution process for the case $0 \leq \theta < \theta_{\text{cr}}$ is very similar to the solution process for the first part of the integral in Eq. (3.138). Thus, with the help of Eq. (3.151), the solution is directly stated here as

$$\begin{bmatrix} \bar{u}_t(x, y, p) \\ \bar{v}_t(x, y, p) \end{bmatrix} = \frac{Q\bar{F}(p)}{2\pi\mu} \int_{-\infty}^{\infty} \begin{bmatrix} f_t(\eta) \\ h_t(\eta) \end{bmatrix} e^{-pg_t(\eta)} d\eta \quad (3.153)$$

$$= \frac{Q\bar{F}(p)}{\pi\mu} \int_{rs_t}^{\infty} \Re \left\{ \begin{bmatrix} f_t(\eta_{t+}(t)) \\ h_t(\eta_{t+}(t)) \end{bmatrix} \frac{d\eta_{t+}}{dt} \right\} e^{-pt} dt. \quad (3.154)$$

The situation in the complex η -plane for the second possible case, that is $\theta_{\text{cr}} \leq \theta < \frac{\pi}{2}$, is shown in Fig. 3.8. In order to avoid that the path of integration actually intersects the branch cut, an additional piece of path around the branch cut is introduced. It is denoted $\eta_{t1+} - \eta_{t1-}$ and has to be taken into account if the second part of the integral (3.129) shall be evaluated. Its basic features are that it approaches but does not touch the cut and opens out in the known contour path $\eta_{t+} - \eta_{t-}$. Thus, in the limit, the values for η on those additional paths are always pure imaginary. The

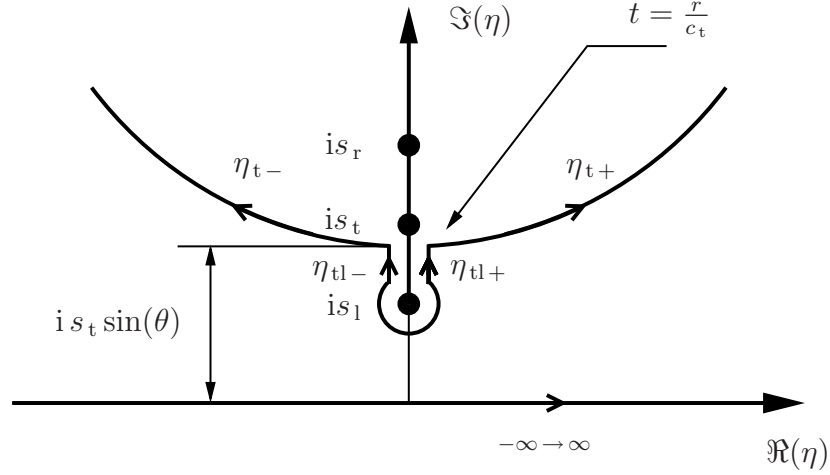


Figure 3.8: Equivalent path of integration for the transverse part (second case).

linear parts of both new paths start at $\eta = is_1$ and open out in the known paths η_{t+} and η_{t-} at $\eta = is_t \sin(\theta)$. It can be recognized from Eq. (3.151) that the two lineal parts are represented by

$$\begin{aligned} \eta_{t\pm}(t) &= -i \sqrt{s_t^2 - \frac{t^2}{r^2}} \cos(\theta) + \frac{it}{r} \sin(\theta) \\ &= i \left[\frac{t}{r} \sin(\theta) - \sqrt{s_t^2 - \frac{t^2}{r^2}} \cos(\theta) \right] \end{aligned} \quad (3.155)$$

if situations $\frac{t}{r} \leq s_t$ are considered. The minimum time t_{tl} that is reached at the branch point $\eta = is_1$ can be determined by plugging in this point into Eq. (3.155), yielding

$$t_{tl} = rs_1 \left[\sin(\theta) + \sqrt{\left(\frac{s_t}{s_1}\right)^2 - 1} \cos(\theta) \right] \quad (3.156)$$

which gives the interval of time $t_{tl} \leq t \leq s_t r$ for which the paths η_{t+} and η_{t-} are represented by Eq. (3.155).

The small circular path around the branch point $\eta = is_1$ shown in Fig. 3.8 has also to be investigated. However, it can be shown that the integral along this path vanishes as the radius of the circle goes to zero. A detailed proof for this circumstance is given in [19]. Thus, only the lineal paths have to be considered in terms of the evaluation

of Eq. (3.153) for the case $\theta_{\text{cr}} \leq \theta < \frac{\pi}{2}$. The solution is obtained by adding the corresponding integrals along the path $\eta_{\text{tl}+} - \eta_{\text{tl}-}$ to the solution to the first case $0 \leq \theta < \theta_{\text{cr}}$. Starting from Eq. (3.153), the additional contributions from the lineal paths to the Laplace transformed displacements \bar{u}_{tl} and \bar{v}_{tl} can be written as

$$\begin{bmatrix} \bar{u}_{\text{tl}}(x, y, p) \\ \bar{v}_{\text{tl}}(x, y, p) \end{bmatrix} = \frac{Q\bar{F}(p)}{2\pi\mu} \int_{\eta_{\text{tl}+}} \begin{bmatrix} f_{\text{t}}(\eta) \\ h_{\text{t}}(\eta) \end{bmatrix} e^{-pg_{\text{t}}(\eta)} d\eta \quad (3.157)$$

$$- \frac{Q\bar{F}(p)}{2\pi\mu} \int_{\eta_{\text{tl}-}} \begin{bmatrix} f_{\text{t}}(\eta) \\ h_{\text{t}}(\eta) \end{bmatrix} e^{-pg_{\text{t}}(\eta)} d\eta. \quad (3.158)$$

These integrals are now evaluated with the help of (3.155) in the same way as the corresponding integrals for the paths $\eta_{\text{t}+}$ and $\eta_{\text{t}-}$. This yields the displacement contributions

$$\begin{bmatrix} \bar{u}_{\text{tl}}(x, y, p) \\ \bar{v}_{\text{tl}}(x, y, p) \end{bmatrix} = = \frac{Q\bar{F}(p)}{\pi\mu} \int_{t_{\text{tl}}}^{r s_{\text{t}}} \Re \left\{ \begin{bmatrix} f_{\text{t}}(\eta_{\text{tl}+}(t)) \\ h_{\text{t}}(\eta_{\text{tl}+}(t)) \end{bmatrix} \frac{d\eta_{\text{tl}+}}{dt} \right\} e^{-pt} dt \quad (3.159)$$

that have to be added to the solution (3.154) if the case $\theta_{\text{cr}} \leq \theta < \frac{\pi}{2}$ is considered. Clearly, the wave field developing in the current problem will have a more cylindrical nature. Therefore, the displacement components

$$u_r = \sin(\theta) u + \cos(\theta) v \quad (3.160)$$

$$u_\theta = -\cos(\theta) u + \sin(\theta) v \quad (3.161)$$

corresponding to polar coordinates are introduced. Then, the Laplace transformed solution to Eq. (3.129) that has been derived can be expressed in polar coordinates

as

$$\bar{u}_{r,1} = \frac{Q\bar{F}(p)}{\pi\mu} \int_{rs_1}^{\infty} \frac{t}{r} \Re \left\{ \frac{(s_t^2 + 2\eta_{1+}^2) d\eta_{1+}}{\tilde{R}(\eta_{1+})} \frac{d\eta_{1+}}{dt} \right\} e^{-pt} dt \quad (3.162)$$

$$\bar{u}_{\theta,1} = \frac{Q\bar{F}(p)}{\pi\mu} \int_{rs_1}^{\infty} \sqrt{\frac{t^2}{r^2} - s_1^2} \Re \left\{ \frac{i(s_t^2 + 2\eta_{1+}^2) d\eta_{1+}}{\tilde{R}(\eta_{1+})} \frac{d\eta_{1+}}{dt} \right\} e^{-pt} dt \quad (3.163)$$

$$\bar{u}_{r,t} = \frac{Q\bar{F}(p)}{\pi\mu} \int_{rs_t}^{\infty} \sqrt{\frac{t^2}{r^2} - s_t^2} \Re \left\{ \frac{-2\eta_{t+} \sqrt{s_1^2 + \eta_{t+}^2} d\eta_{t+}}{\tilde{R}(\eta_{t+})} \frac{d\eta_{t+}}{dt} \right\} e^{-pt} dt \quad (3.164)$$

$$\bar{u}_{\theta,t} = -\frac{Q\bar{F}(p)}{\pi\mu} \int_{rs_t}^{\infty} \frac{t}{r} \Re \left\{ \frac{i(s_t^2 + 2\eta_{1+}^2) d\eta_{t+}}{\tilde{R}(\eta_{t+})} \frac{d\eta_{t+}}{dt} \right\} e^{-pt} dt \quad (3.165)$$

$$\bar{u}_{r,t1} = \frac{Q\bar{F}(p)}{\pi\mu} \int_{t_{t1}}^{rs_t} \sqrt{s_t^2 - \frac{t^2}{r^2}} \Re \left\{ \frac{2i\eta_{t1+} \sqrt{s_1^2 + \eta_{t1+}^2} d\eta_{t1+}}{\tilde{R}(\eta_{t1+})} \frac{d\eta_{t1+}}{dt} \right\} e^{-pt} dt \quad (3.166)$$

$$\bar{u}_{\theta,t1} = -\frac{Q\bar{F}(p)}{\pi\mu} \int_{t_{t1}}^{rs_t} \frac{t}{r} \Re \left\{ \frac{2i\eta_{t1+} \sqrt{s_1^2 + \eta_{t1+}^2} d\eta_{t1+}}{\tilde{R}(\eta_{t1+})} \frac{d\eta_{t1+}}{dt} \right\} e^{-pt} dt \quad (3.167)$$

where Eqs. (3.144), (3.151) and (3.155) have been used. The entire solution for the transformed displacements in the half-space are thus given for positions $0 < r < \infty$ and $0 \leq \theta < \frac{\pi}{2}$ by

$$\bar{u}_r(r, \theta, p) = \bar{u}_{r,1} + \bar{u}_{r,t} + \bar{u}_{r,t1} \quad (3.168)$$

$$\bar{u}_{\theta}(r, \theta, p) = \bar{u}_{\theta,1} + \bar{u}_{\theta,t} + \bar{u}_{\theta,t1} \quad (3.169)$$

where the last term in each displacement applies only in the case $\theta_{cr} \leq \theta < \frac{\pi}{2}$ as it was explained above.

Finally, the case $\theta = \frac{\pi}{2}$ (or $y = 0$, in Cartesian coordinates) shall be examined. According to Eq. (3.160), the displacements in polar coordinates at the surface are given by

$$\bar{u}_r\left(r, \frac{\pi}{2}, p\right) = \bar{u}\left(r, \frac{\pi}{2}, p\right) \quad (3.170)$$

$$\bar{u}_{\theta}\left(r, \frac{\pi}{2}, p\right) = \bar{v}\left(r, \frac{\pi}{2}, p\right). \quad (3.171)$$

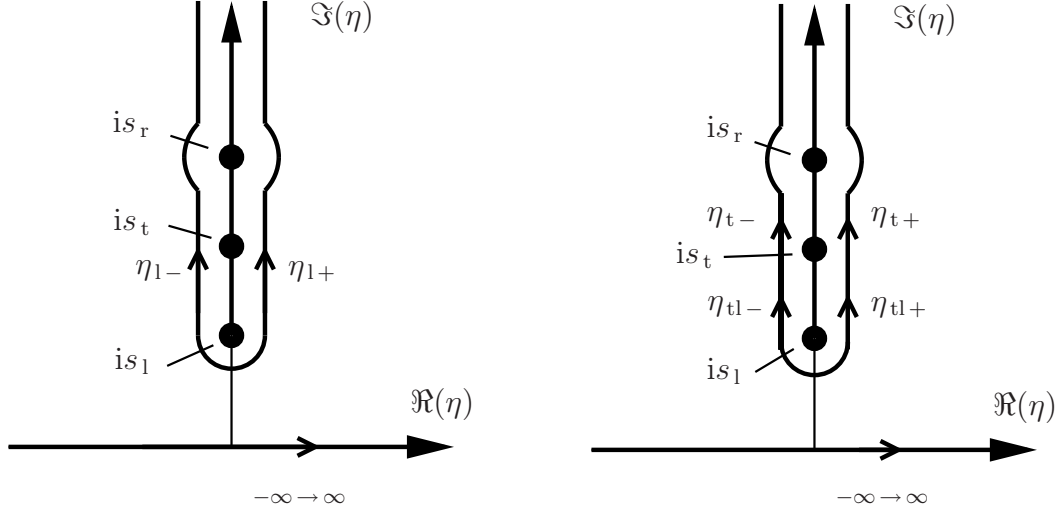


Figure 3.9: Equivalent paths of integration for $\theta = \frac{\pi}{2}$, longitudinal part (left) and transverse part (right).

Basically, the solution to the displacements in Eqs. (3.170) and (3.171) is obtained by just plugging in $\theta = \frac{\pi}{2}$ in the derivation following Eq. (3.138). However, special consideration has to be given to the specific paths of integration in the complex η -plane arising for the given situation. This is also why this situation was excluded from the general derivation for the interior of the half-space. The paths of integration applying now are shown in Fig. 3.9. Of course, for the transverse part, the case $\theta \geq \theta_{\text{cr}}$ has to be considered. The paths can be determined by inserting $\theta = \frac{\pi}{2}$ into Eqs. (3.144), (3.151) and (3.155). This yields

$$\eta_{l\pm}(t) = \frac{it}{r} \quad s_1 \leq \frac{t}{r} \leq \infty \quad (3.172)$$

$$\eta_{t\pm}(t) = \frac{it}{r} \quad s_t \leq \frac{t}{r} \leq \infty \quad (3.173)$$

$$\eta_{tl\pm}(t) = \frac{it}{r} \quad \frac{t_{tl}}{r} \leq \frac{t}{r} \leq s_t \quad (3.174)$$

where $t_{tl} = rs_1$ in the case considered. Obviously, the paths of integration are identical for both terms in the integrand of Eq. (3.138). This makes sense because the terms $g_l(\eta)$ and $g_t(\eta)$ appearing in the exponents happen to be identical in this

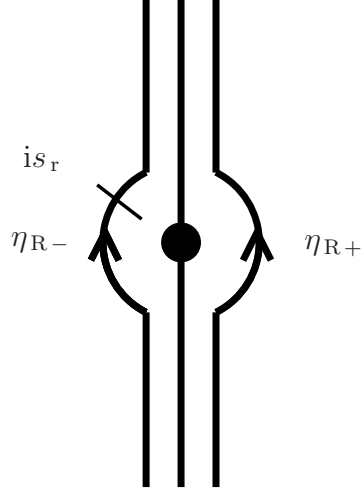


Figure 3.10: Paths of integration around the Rayleigh pole at $\eta = is_r$.

specific case, that is

$$g_l(\eta) = g_t(\eta) = -i\eta r. \quad (3.175)$$

As mentioned earlier in this derivation, it can be shown that the integrals along the small circular paths around the branch point $\eta = is_1$ vanish if their radius goes to zero. Thus, only the integrals along the paths stated above have to be taken into account. However, this means that, so far, there is no difference between the derivation of the solution to the displacements on the surface and the derivation of the solution in the interior of the half-space for the specific case $\theta = \frac{\pi}{2}$ what would mean that the displacement solutions should be identical. However, there is one fact that is different for the solution on the surface: here, the paths of integration $\eta_{l\pm}$ and $\eta_{t\pm}$ shown in Fig. 3.9 touch the Rayleigh simple pole which is located at $\eta = is_r$. This means that the integrals along those paths exist only as Cauchy principal values and additional contributions to the integrals due to integration “around” the Rayleigh pole have to be considered. The situation is shown in Fig. 3.2.3. The additional circular paths are called η_{R-} and η_{R+} . They may be expressed as

$$\eta = is_r + r_R e^{i\varphi_R}. \quad (3.176)$$

Then, the additional contribution $\bar{u}_{r,R}$ of the Rayleigh simple pole is computed by repeating the derivation beginning at Eq. (3.138) for the circular path mentioned. The separation into two terms is not necessary anymore since the terms in the exponentials and thus, also the paths of integration, are identical. This yields the Laplace transformed displacement $\bar{u}_{r,R}$ in radial direction as

$$\begin{aligned}\bar{u}_{r,R}\left(r, \frac{\pi}{2}, p\right) &= \bar{u}_R\left(r, \frac{\pi}{2}, p\right) \\ &= \frac{Q\bar{F}(p)}{2\pi\mu} \lim_{r_R \rightarrow 0} \int_{\eta_{R+} - \eta_{R-}} [f_1(\eta) + f_t(\eta)] e^{ip\eta r} d\eta \\ &= \frac{Q\bar{F}(p)}{\pi\mu} \lim_{r_R \rightarrow 0} \int_{\eta_{R+}} \Re \{ [f_1(\eta) + f_t(\eta)] e^{ip\eta r} d\eta \}.\end{aligned}\quad (3.177)$$

In the last step, the conjugate properties of the functions $f_1(\eta)$ and $f_t(\eta)$ have been used to rewrite the integral in a similar way as it was done with the integral in Eqs. (3.146) - (3.148). Plugging in the definitions of $f_1(\eta)$ and $f_t(\eta)$ which are given by Eqs. (3.132) and (3.133) yields

$$\dots = \frac{Q\bar{F}(p)}{\pi\mu} \lim_{r_R \rightarrow 0} \int_{\eta_{R+}} \Re \left\{ \frac{i\eta \left[2\sqrt{\eta^2 + s_1^2} \sqrt{\eta^2 + s_t^2} - (2\eta^2 + s_t^2) \right]}{\tilde{R}(\eta)} e^{ip\eta r} d\eta \right\}.\quad (3.178)$$

Now, the approximation

$$\tilde{R}(\eta) \simeq r_R e^{i\varphi_R} \tilde{R}'(is_r) \quad \text{where} \quad \tilde{R}'(is_r) = \left[\frac{d\tilde{R}}{d\eta} \right]_{\eta=is_r} \quad (3.179)$$

which is valid near $\eta = is_r$ is introduced. It can be used to reformulate Eq. (3.178) as

$$\bar{u}_{r,R}\left(r, \frac{\pi}{2}, p\right) = -\frac{Q\bar{F}(p)}{4\mu} \frac{s_t^2 (2s_r^2 - s_t^2)^3}{8(s_t^2 - s_1^2) s_r^6 - 4s_t^6 s_r^2 + s_t^8} e^{-ps_r r} \quad (3.180)$$

where the definition of $\tilde{R}(\eta)$ in Eq. (3.136) has been used.

The Laplace transformed displacement $\bar{u}_{\theta,R}$ in tangential direction can be obtained in an easier way. Consideration of the numerator in the integrand of Eq. (3.178) shows

that it becomes pure real in the vicinity of $\eta = is_r$. More specifically, it is

$$\begin{aligned} & \left[i\eta \left(2\sqrt{\eta^2 + s_1^2} \sqrt{\eta^2 + s_t^2} - (2\eta^2 + s_t^2) \right) \right]_{\eta=is_r} \\ &= s_r \left[2\sqrt{s_r^2 - s_1^2} \sqrt{s_r^2 - s_t^2} + s_t^2 - 2s_r^2 \right]. \end{aligned} \quad (3.181)$$

Here, the fact that $s_r > s_1$ and $s_r > s_t$ hold for real materials was used. Now, the additional contribution $\bar{u}_{\theta R}$ of the Rayleigh simple pole to the Laplace transformed tangential displacement is written according to Eqs. (3.177) and (3.178) as

$$\begin{aligned} \bar{u}_{\theta, R} \left(r, \frac{\pi}{2}, p \right) &= \bar{v}_R \left(r, \frac{\pi}{2}, p \right) \\ &= \frac{Q\bar{F}(p)}{2\pi\mu} \lim_{r_R \rightarrow 0} \int_{\eta_{R+} - \eta_{R-}} [h_l(\eta) + h_t(\eta)] e^{ip\eta r} d\eta \\ &= \frac{Q\bar{F}(p)}{\pi\mu} \lim_{r_R \rightarrow 0} \int_{\eta_{R+}} \Re \{ [h_l(\eta) + h_t(\eta)] e^{ip\eta r} d\eta \} \end{aligned} \quad (3.182)$$

$$= \frac{Q\bar{F}(p)}{\pi\mu} \lim_{r_R \rightarrow 0} \int_{\eta_{R+}} \Re \left\{ \frac{s_t^2 \sqrt{\eta^2 + s_1^2}}{\tilde{R}(\eta)} e^{ip\eta r} d\eta \right\}. \quad (3.183)$$

Now, considering the numerator of the integrand in Eq. (3.183) in the vicinity of $\eta = is_r$ yields

$$\left[s_t^2 \sqrt{\eta^2 + s_1^2} \right]_{\eta=is_r} = is_t^2 \sqrt{s_r^2 - s_1^2}. \quad (3.184)$$

Here, the numerator of the integrand becomes pure imaginary since it is $s_r > s_1$. Since it can be shown [19] that $\tilde{R}'(is_r)$ is also pure imaginary, the value of the integral in Eq. (3.183) will be pure imaginary, too, if $r_R \rightarrow 0$. Thus, it can be concluded that

$$\bar{u}_{\theta, R} \left(r, \frac{\pi}{2}, p \right) = 0 \quad (3.185)$$

because only the real part of the integral mentioned is taken into account in Eq. (3.183). Therefore, the Laplace transformed solutions to the displacements on the surface of the half-space are given by

$$\bar{u}_r \left(r, \frac{\pi}{2}, p \right) = [\bar{u}_{r, l} + \bar{u}_{r, t} + \bar{u}_{r, tl}]_{\theta=\frac{\pi}{2}} + \bar{u}_{r, R} \left(r, \frac{\pi}{2}, p \right) \quad (3.186)$$

$$\bar{u}_{\theta} \left(r, \frac{\pi}{2}, p \right) = [\bar{u}_{\theta, l} + \bar{u}_{\theta, t} + \bar{u}_{\theta, tl}]_{\theta=\frac{\pi}{2}}. \quad (3.187)$$

The very last step of this derivation is the inversion of the Laplace transformed solutions to the displacements. In [19], it is described why the inversion of the displacements to the time domain is unique if the transform variable p is real and greater than some fixed positive value. Recalling that p was indeed required to be real and positive in order to select only the real and positive branches of α_1 and α_t before Eqs. (3.108) and (3.109), it is clear that the inversion of Eqs. (3.186) and (3.187) has to be unique.

At first, the input time signal $F(t)$ will be restricted to be a unit impulse $F(t) = \delta(t)$. Later on, it will be shown that it is relatively easy to expand this specific solution to a general input time signal. These specific solutions to the radial and the tangential displacements for the input described are denoted $u_r^\delta(r, \theta, t)$ and $u_\theta^\delta(r, \theta, t)$, respectively. Then, the corresponding Laplace transformed input signal is $\bar{F}(p) = 1$.

Having a closer look at the form of the solutions (Eqs. (3.168) and (3.169) in combination with Eqs. (3.162) - (3.167)) to the displacements in the interior of the half-space and comparing them to the definition of the Laplace transform (3.98a) shows immediately that

$$\begin{aligned} u_r^\delta(r, \theta, t) = & \frac{Q}{\pi\mu} \left\{ \frac{t}{r} \Re \left[\frac{(s_t^2 + 2\eta_{1+}^2) d\eta_{1+}}{\tilde{R}(\eta_{1+}) dt} \right] H \left(t - \frac{r}{c_1} \right) \right. \\ & + \sqrt{\frac{t^2}{r^2} - s_t^2} \Re \left[\frac{-2\eta_{t+} \sqrt{s_1^2 + \eta_{t+}^2} d\eta_{t+}}{\tilde{R}(\eta_{t+}) dt} \right] H \left(t - \frac{r}{c_t} \right) \\ & \left. + \sqrt{s_t^2 - \frac{t^2}{r^2}} \Re \left[\frac{2i\eta_{tl+} \sqrt{s_1^2 + \eta_{tl+}^2} d\eta_{tl+}}{\tilde{R}(\eta_{tl+}) dt} \right] \left[H(t - t_{tl}) - H \left(t - \frac{r}{c_t} \right) \right] \right\} \end{aligned} \quad (3.188)$$

and

$$\begin{aligned} u_\theta^\delta(r, \theta, t) = & \frac{Q}{\pi\mu} \left\{ \sqrt{\frac{t^2}{r^2} - s_1^2} \Re \left[\frac{i(s_t^2 + 2\eta_{1+}^2) d\eta_{1+}}{\tilde{R}(\eta_{1+}) dt} \right] H \left(t - \frac{r}{c_1} \right) \right. \\ & + \frac{t}{r} \Re \left[\frac{i(s_t^2 + 2\eta_{1+}^2) d\eta_{t+}}{\tilde{R}(\eta_{t+}) dt} \right] H \left(t - \frac{r}{c_t} \right) \\ & \left. + \frac{t}{r} \Re \left[\frac{2i\eta_{tl+} \sqrt{s_1^2 + \eta_{tl+}^2} d\eta_{tl+}}{\tilde{R}(\eta_{tl+}) dt} \right] \left[H(t - t_{tl}) - H \left(t - \frac{r}{c_t} \right) \right] \right\} \end{aligned} \quad (3.189)$$

are valid inversions of the Laplace transformed solutions which have been derived if $H(\cdot)$ denotes the Heaviside step function. Since, as mentioned above, the inversion has to be unique in the present case, it follows that Eqs. (3.188) and (3.189) are the only time-domain solutions to the displacement field in the interior of the half-space investigated.

The appearance of the Heaviside step functions in Eqs. (3.188) and (3.189) can be explained by the fact that the limits of the integrals in Eqs. (3.162) - (3.167) deviate from those in the definition of the Laplace transform (3.98a). In order that the integrals in each of the terms derived and the one in the Laplace transform represent the same value although their limits are different, the integrands are set to zero outside of the time intervals which the respective integrals have in common; this is realized with the Heaviside step functions. Equations (3.188) and (3.189) are valid for $0 < r < \infty$ and $0 \leq \theta < \frac{\pi}{2}$; however, the third term in both equations applies only in the case $\theta_{cr} \leq \theta < \frac{\pi}{2}$.

The time-domain solution to the displacements at the surface $\theta = \frac{\pi}{2}$ can easily be found by making use of the Laplace transformation pair

$$\delta(t - T) \xleftrightarrow{\mathcal{L}} e^{-pT} \quad (3.190)$$

where T is a positive constant. This yields

$$u_r^\delta(r, \frac{\pi}{2}, t) = \left[\begin{array}{l} \text{R.H.S. of Eq. (3.188)} \\ \text{evaluated at } \theta = \frac{\pi}{2} \end{array} \right] - \frac{Q}{4\mu} \frac{s_t^2 (2s_r^2 - s_t^2)^3}{8(s_t^2 - s_1^2) s_r^6 - 4s_t^6 s_r^2 + s_t^8} \delta\left(t - \frac{r}{c_r}\right) \quad (3.191)$$

$$u_\theta^\delta(r, \frac{\pi}{2}, t) = \left[\begin{array}{l} \text{R.H.S. of Eq. (3.189)} \\ \text{evaluated at } \theta = \frac{\pi}{2} \end{array} \right]. \quad (3.192)$$

As mentioned earlier, the solutions u_r^δ and u_θ^δ in Eqs. (3.188) - (3.192) to a unit impulse $F(t) = \delta(t)$ can be relatively easy extended to a more general input signal $F(t)$.

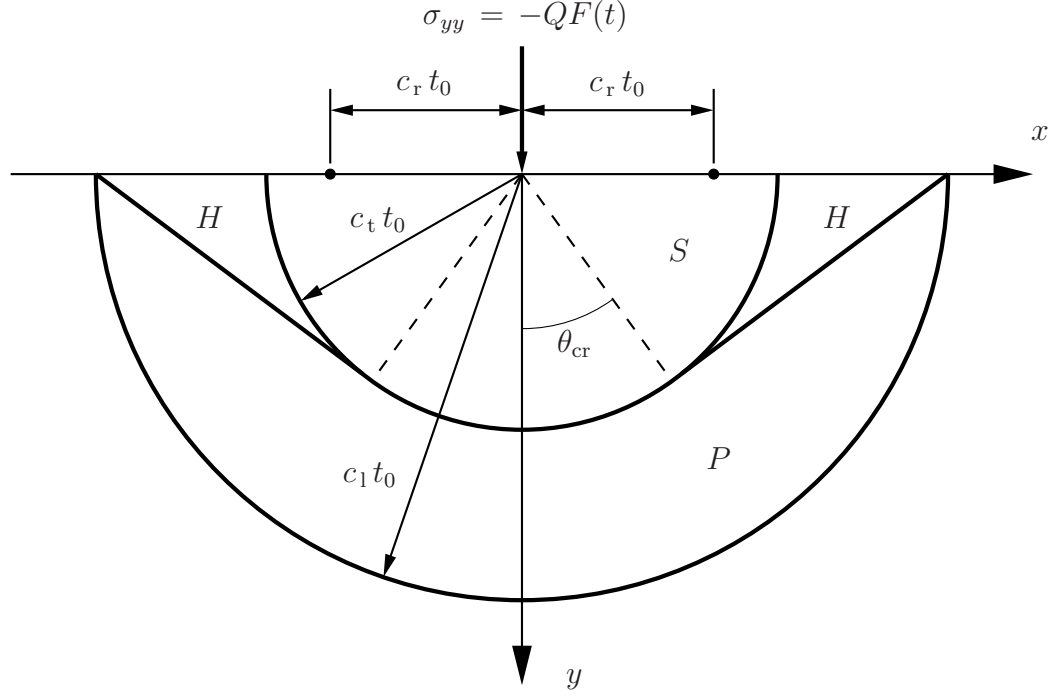


Figure 3.11: Nature of the arising displacement field in a half-space due to a line load $\sigma_{yy}(x, y = 0, t) = -QF(t)\delta(x)$ at a fixed time $t = t_0$.

Making use of the convolution theorem, which is given by

$$\int_0^t f_1(\tau) f_2(t - \tau) d\tau \xleftrightarrow{\mathcal{L}} \bar{f}_1(p) \bar{f}_2(p), \quad (3.193)$$

yields the final result of this derivation

$$\begin{bmatrix} u_r(r, \theta, t) \\ u_\theta(r, \theta, t) \end{bmatrix} = \int_0^t F(t - \tau) \begin{bmatrix} u_r^\delta(r, \theta, \tau) \\ u_\theta^\delta(r, \theta, \tau) \end{bmatrix} d\tau. \quad (3.194)$$

The displacement solution given by Eqs. (3.188), (3.189), (3.191) and (3.192) for the Lamb's problem arising due a unit impulse input signal shows that four different types of waves occur. Their essential nature is shown in Fig. 3.11 for a fixed time $t = t_0$ where the symmetry to the y -axis mentioned earlier in the derivation is used to illustrate the domain which is defined by $0 < r < \infty$ and $-\frac{\pi}{2} \leq \theta < 0$. The first wave occurring is a cylindrical wave traveling from the origin outwards with the propagation speed c_1 . It covers the domain $0 < r \leq c_1 t_0$ which is denoted P . A

second wave also spreading cylindrically from the origin travels with the propagation speed c_t and covers the region $0 < r \leq c_t t_0$ called S . The third wave arising is the so-called head wave which is also referred to as von Schmidt wave. It is not a cylindrical wave but it has two straight wavefronts on each side of the axis of symmetry as it is shown in Fig. 3.11. On the surface, these wavefronts arrive as soon as the first wave traveling with the propagation speed c_1 does. For smaller angles θ , this wave arrives later with respect to the first cylindrical wave. For $\theta = \theta_{cr}$, its wavefronts merge tangentially into the wavefront of the second cylindrical wave traveling with the propagation speed c_t . Obviously, the domains H of the head wave are given by

$$c_t t_0 \leq r \leq \frac{c_1 t_0}{\sin |\theta| + \sqrt{\left(\frac{c_1}{c_t}\right)^2 - 1} \cos |\theta|} \quad (3.195)$$

$$\theta_{cr} \leq |\theta| \leq \frac{\pi}{2}. \quad (3.196)$$

Its direction of propagation is normal to the straight wavefronts mentioned and its speed of propagation is c_t . The last wave occurring is the so-called Rayleigh surface wave which travels out from the origin in both directions at the surface. Its speed of propagation is c_r .

3.2.4 Stress-Strain Relationship Including a Quadratic Nonlinearity

In this section, an elastic half-space subjected to a line load at its surface is considered analog to Section 3.2.1; see Fig. 3.4. However, now, the stress-strain relationship of the half-space's material is assumed to include a quadratic nonlinearity. Thus, the only differences between this problem and the one described in the previous section are the constitutive equations, while the governing equations (3.91), the boundary conditions (3.87) and the initial conditions (3.89) are identical. Again, only small displacement and strains shall be considered. As explained in the previous section, the issue investigated is again a two-dimensional problem in plane strain for reasons of symmetry, meaning that there cannot arise any displacement in z -direction and that

all derivatives with respect to z have to vanish. In order to determine the nonlinear constitutive equations, Eq. (2.11) again has to be applied. The invariants of the strain tensor which are needed to find the internal elastic energy density Γ reduce, according to Eq. (2.13), to

$$\begin{aligned} I_1 &= \varepsilon_{xx} + \varepsilon_{yy} \\ I_2 &= \varepsilon_{xx}\varepsilon_{yy} - \varepsilon_{xy}^2 \\ I_3 &= 0 \end{aligned} \tag{3.197}$$

since it is $\varepsilon_{xz} = \varepsilon_{yz} = \varepsilon_{zz} = 0$. Plugging these and the displacement-strain relationships (2.15) applying into Eq. (2.12) yields

$$\begin{aligned} \Gamma &= \frac{\lambda + 2\mu}{2} (\varepsilon_{xx} + \varepsilon_{yy})^2 - 2\mu (\varepsilon_{xx}\varepsilon_{yy} - \varepsilon_{xy}^2) \\ &+ \frac{l + 2m}{3} (\varepsilon_{xx} + \varepsilon_{yy})^3 - 2m (\varepsilon_{xx} + \varepsilon_{yy}) (\varepsilon_{xx}\varepsilon_{yy} - \varepsilon_{xy}^2) \end{aligned} \tag{3.198}$$

$$\begin{aligned} &= \frac{\lambda + 2\mu}{2} \left(\frac{\partial u}{\partial x} + \frac{\partial v}{\partial y} \right)^2 - 2\mu \left(\frac{\partial u}{\partial x} \frac{\partial v}{\partial y} - \frac{1}{4} \left(\frac{\partial u}{\partial y} + \frac{\partial v}{\partial x} \right)^2 \right) \\ &+ \frac{l + 2m}{3} \left(\frac{\partial u}{\partial x} + \frac{\partial v}{\partial y} \right)^3 \\ &- 2m \left(\frac{\partial u}{\partial x} + \frac{\partial v}{\partial y} \right) \left(\frac{\partial u}{\partial x} \frac{\partial v}{\partial y} - \frac{1}{4} \left(\frac{\partial u}{\partial y} + \frac{\partial v}{\partial x} \right)^2 \right). \end{aligned} \tag{3.199}$$

The nonlinear constitutive equations are now derived from Eq. (2.11) as

$$\begin{aligned} \sigma_{xx} = \frac{\partial \Gamma}{\partial \left(\frac{\partial u}{\partial x} \right)} &= (\lambda + 2\mu) \frac{\partial u}{\partial x} + \lambda \frac{\partial v}{\partial y} + (l + 2m) \left(\frac{\partial u}{\partial x} \right)^2 \\ &+ l \frac{\partial v}{\partial y} \left(2 \frac{\partial u}{\partial x} + \frac{\partial v}{\partial y} \right) + \frac{m}{2} \left(\frac{\partial u}{\partial y} + \frac{\partial v}{\partial x} \right)^2 \end{aligned} \tag{3.200}$$

$$\begin{aligned} \sigma_{yy} = \frac{\partial \Gamma}{\partial \left(\frac{\partial v}{\partial y} \right)} &= (\lambda + 2\mu) \frac{\partial v}{\partial y} + \lambda \frac{\partial u}{\partial x} + (l + 2m) \left(\frac{\partial v}{\partial y} \right)^2 \\ &+ l \frac{\partial u}{\partial x} \left(2 \frac{\partial v}{\partial y} + \frac{\partial u}{\partial x} \right) + \frac{m}{2} \left(\frac{\partial u}{\partial y} + \frac{\partial v}{\partial x} \right)^2 \end{aligned} \tag{3.201}$$

$$\begin{aligned} \sigma_{xy} &= \frac{\partial \Gamma}{\partial \left(\frac{\partial u}{\partial y} \right)} \\ &= \frac{\partial \Gamma}{\partial \left(\frac{\partial v}{\partial x} \right)} = \left(\frac{\partial u}{\partial y} + \frac{\partial v}{\partial x} \right) \left[\mu + m \left(\frac{\partial u}{\partial x} + \frac{\partial v}{\partial y} \right) \right]. \end{aligned} \tag{3.202}$$

These nonlinear constitutive equations complete the current problem statement. Clearly, the linear problem can be obtained if the third-order elastic constants are chosen to vanish, that is $l = m = 0$. Plugging in the new stress-displacement relationships (3.200) - (3.202) in the governing equations (3.91) yields two coupled nonlinear second-order partial differential equations. However, the integral transforms used for the solution to the linear problem in the previous section are based on the assumption of linearity meaning that they are inappropriate for the derivation of the solution to the present nonlinear problem. For the boundary conditions (3.87) and initial conditions (3.89) mentioned, to the best knowledge of the author, no analytical solution is available at this point of time. Thus, only numerical solutions obtained by the application of a simulation code can be found for this problem as described in the subsequent chapters.

3.3 Normal Reflection of a Plane Wave Generated by a Uniform Surface Traction in a Plate

In this section, normal reflections of plane waves traveling in a plate consisting of an elastic material with quadratic nonlinearity in its stress-strain relationship are investigated. The motivation for this investigation is due to the fact that half-spaces which have been considered in the previous sections are relatively unrealistic in terms of the realization of a corresponding experimental measurement because it is not straightforward to create an experimental setup that represents a domain with semi-infinite dimensions. Another point that makes this derivation desirable is the question whether the effects of reflection may be used to measure a material's nonlinearity in a more convenient way. More specifically, since the nonlinear effects partly depend on the propagation distance of a wave as shown in Subsection 3.1.2, it may be possible to increase the distance covered by a wave by multiple reflections in the plate. Because

one of the nonlinear effects depends linearly on the propagation distance, this proceeding could provide a possibility to amplify this effect which is usually very small compared to the linear behavior. Thus, it could be easier to obtain better results in experimental measurements if the effects of reflection were exploited.

Note that the scenario presented in this section is similar to the wave propagation in a nonlinear half-space as it is described in Subsection 3.1.2. The main difference is, as already explained, that the domain considered has now a finite dimension in the direction of wave propagation in contrast to the half-space which has been used in the subsection mentioned. Another difference will be the traction input signal applied at one side of the plate. Here, only a pure pressure traction will be treated in order to keep the presentation as clear and simple as possible. Moreover, since reflection phenomena may be understood more clearly if the superposition of incident and reflected wave is avoided, a sinusoidal finite-length pres

In this derivation, the two special cases of a reflection at a perfectly rigid and at a perfectly stress-free boundary are treated. The two different scenarios are shown in Figures 3.12 and 3.13.

3.3.1 Incident Wave

At first, a solution to the incident wave arising due to the pure pressure boundary condition shall be presented. Because of the symmetry of this problem, displacements may only occur in y -direction. According to the constitutive equations (3.52) and (3.53), this means also that only normal stresses σ_{yy} in y -direction can develop. The boundary condition for the incident wave can be formulated as

$$\sigma_{yy}(x, y = 0, t) = -Q_1 F(t) \quad (3.203)$$

$$\sigma_{xy}(x, y = 0, t) = 0. \quad (3.204)$$

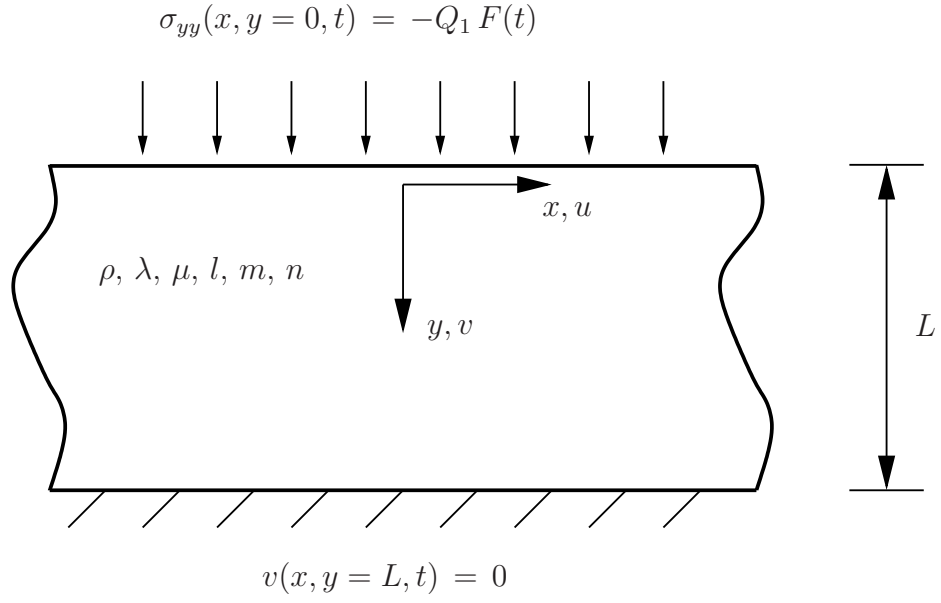


Figure 3.12: Plate subjected to a surface pressure at one side and clamped rigidly at the opposite side.

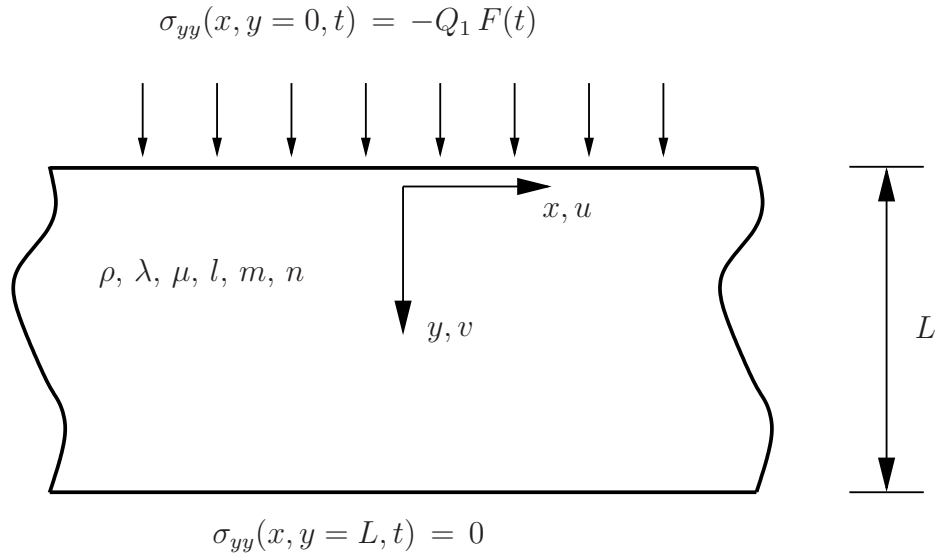


Figure 3.13: Plate subjected to a surface pressure at one side and a stress-free opposite side.

The dimensionless time function $F(t)$ is given by

$$F(t) = \begin{cases} \sin(\omega t) & \text{for } \Delta t \geq t \geq 0 \\ 0 & \text{otherwise} \end{cases} \quad (3.205)$$

where Δt is the length of time of the input pressure impulse. The initial condition is that the entire domain of the plate is at rest for $t < 0$. The linear solution $v_1^{(i)}$ to this problem was already derived in Subsection 3.1.1. According to Eqs. (3.18) and (3.19), the solution to the particle displacement $v_1^{(i)}$ becomes

$$v_1^{(i)}(y, t) = -\frac{Q_1}{k_1(\lambda + 2\mu)} \begin{cases} 0 & \text{for } t - \frac{y}{c_1} < 0 \\ (\cos(\omega t - k_1 y) - 1) & \text{for } \Delta t \geq t - \frac{y}{c_1} \geq 0 \\ (\cos(\omega \Delta t) - 1) & \text{for } t - \frac{y}{c_1} > \Delta t. \end{cases} \quad (3.206)$$

Obviously, the solution for the range $\Delta t \geq t - \frac{y}{c_1} \geq 0$ is identical to the steady-state solution (3.45) if its constant displacement term V_1 is adapted to the initial condition. The further investigation is limited to the range mentioned so that the derivation will be close to the one presented for the steady-state solution. Making again use of the perturbation theory, the partial differential equation for the displacement correction term $v_2^{(i)}$ in this range is given by Eq. (3.63). Thus, the solution to the displacement $v_2^{(i)}$ given by Eq. (3.69) is also valid for the present problem in the range $\Delta t \geq t - \frac{y}{c_1} \geq 0$ if the constant displacement term V_2 is chosen appropriately according to the initial condition. The total displacement $v^{(i)}$ in y -direction is then given by

$$\begin{aligned} v^{(i)}(y, t) = & -\frac{Q_1}{k_1(\lambda + 2\mu)} (\cos(\omega t - k_1 y) - 1) \\ & - C_7 \sin(2(\omega t - k_1 y)) + C_8 \left(t - \frac{y}{c_1} \right) \\ & + C_3 y \cos(2(\omega t - k_1 y)) \quad \text{for } \Delta t \geq t - \frac{y}{c_1} \geq 0 \end{aligned} \quad (3.207)$$

where the terms C_3 , C_7 and C_8 are defined as in Subsection 3.1.2. The corresponding particle velocity $\dot{v}^{(i)}$ is then

$$\begin{aligned} \dot{v}^{(i)}(y, t) = & \frac{c_1 Q_1}{\lambda + 2\mu} \sin(\omega t - k_1 y) - 2\omega C_7 \cos(2(\omega t - k_1 y)) + C_8 \\ & - 2\omega C_3 y \sin(2(\omega t - k_1 y)) \quad \text{for } \Delta t \geq t - \frac{y}{c_1} \geq 0. \end{aligned} \quad (3.208)$$

3.3.2 Reflection at a Rigid Boundary

In this subsection, the appearance of the reflection of the incident wave (3.207) at a rigid boundary shall be investigated. The situation has already been shown in Fig. 3.12. In order to keep this presentation clear, only those situations shall be considered where the incident wave impulse has already completely reached the boundary. Then, the wave field will consist only of the reflected wave.

The rigid boundary condition at the opposite side of the plate can be written as

$$u(x, y = L, t) = 0 \quad (3.209)$$

$$v(x, y = L, t) = 0. \quad (3.210)$$

Since only displacements v in y -direction appear in the case considered, the first boundary condition is automatically fulfilled. The reflection of the fundamental incident wave which would develop in a linear material is

$$\begin{aligned} v_1^{(r)}(y, t) = & \frac{Q_1}{k_1(\lambda + 2\mu)} (\cos(\omega t - k_1(2L - y)) - 1) \\ & \text{for } \Delta t \geq t - \frac{2L - y}{c_1} \geq 0 \end{aligned} \quad (3.211)$$

which fulfills the boundary condition (3.210).

Considering now the nonlinear case, the reflected wave has to include a correction term $v_2^{(r)}$ corresponding to the term $v_2^{(i)}$ in the incident wave. According to Eq. (3.207), this has been

$$\begin{aligned} v_2^{(i)}(y, t) = & -C_7 \sin(2\omega t - 2k_1 y) + C_8 \left(t - \frac{y}{c_1} \right) \\ & + C_3 y \cos(2\omega t - 2k_1 y) \quad \text{for } \Delta t \geq t - \frac{y}{c_1} \geq 0. \end{aligned} \quad (3.212)$$

In order to find a solution to $v_2^{(r)}$, the partial differential equation describing the appearance of the nonlinear correction term has to be resolved. This partial differential equation is Eq. (3.63) in which the displacement u_1 disappears and v_1 has to be chosen accordingly to the reflected fundamental wave in Eq. (3.211). More specifically, this yields

$$\frac{\partial^2 v_2^{(r)}}{\partial t^2} - c_1^2 \frac{\partial^2 v_2^{(r)}}{\partial y^2} = \frac{\beta}{2} \frac{\partial}{\partial y} \left(\frac{\partial v_1^{(r)}}{\partial y} \right)^2 \quad (3.213)$$

$$= \frac{\beta Q_1^2}{c_1^2 k_1 (\lambda + 2\mu)^2} \sin(\omega t + k_1 y - 2k_1 L) \cos(\omega t + k_1 y - 2k_1 L) \quad (3.214)$$

for $\Delta t \geq t - \frac{2L - y}{c_1} \geq 0$.

Note that this formulation does not account for some effects of interaction occurring when the incident impulse has exactly reached the boundary at $y = L$, i. e., when the front part of the impulse has already been reflected and the rear part is still traveling towards the boundary. The effects of this second part are neglected in Eq. (3.213) because only the fundamental wave traveling backwards is considered on the right side. However, in the frame of the assumptions and simplifications

The general solution to Eq. (3.213) is

$$\begin{aligned} v_2^{(r)}(y, t) &= f(\omega t - k_1 y) + g(\omega t + k_1 y) \\ &\quad + C_{10} (4\omega y \cos(2\omega t - 2k_1(2L - y)) \\ &\quad - c_1 \sin(2\omega t - 2k_1(2L - y))) \quad (3.215) \\ &\quad \text{for } \Delta t \geq t - \frac{2L - y}{c_1} \geq 0 \end{aligned}$$

where

$$C_{10} = \frac{\beta Q_1^2}{32 \omega c_1^2 (\lambda + 2\mu)^2}. \quad (3.216)$$

The term $f(\omega t - k_1 y)$ in Eq. (3.215) is discarded here a priori because the reflected wave is a disturbance traveling only in the negative y -direction, while the remaining term $g(\omega t + k_1 y)$ has to be determined from the boundary condition at $y = L$. In

terms of the incident and the reflected wave, the boundary condition (3.210) is written as

$$\begin{aligned} v(x, L, t) &= v^{(i)}(x, L, t) + v^{(r)}(x, L, t) = 0 \\ \Rightarrow v_2^{(r)}(x, L, t) &= -v_1^{(i)}(x, L, t) - v_2^{(i)}(x, L, t) - v_1^{(r)}(x, L, t). \end{aligned} \quad (3.217)$$

Since the right side of Eq. (3.217) is known, the actual appearance of the solution to the nonlinear correction term $v_2^{(r)}$ presented in Eq. (3.215) can be determined to be

$$\begin{aligned} v_2^{(r)}(y, t) &= C_7 \sin(2\omega t - 2k_1(2L - y)) \\ &\quad - C_8 \left(t - \frac{2L - y}{c_1} \right) \\ &\quad - C_3 (2L - y) \cos(2\omega t - 2k_1(2L - y)) \\ &\quad \text{for } \Delta t \geq t - \frac{2L - y}{c_1} \geq 0. \end{aligned} \quad (3.218)$$

Thus, the total solution to the reflected wave is given by

$$\begin{aligned} v^{(r)}(y, t) &= \frac{Q_1}{k_1(\lambda + 2\mu)} (\cos(\omega t - k_1(2L - y)) - 1) \\ &\quad + C_7 \sin(2\omega t - 2k_1(2L - y)) \\ &\quad - C_8 \left(t - \frac{2L - y}{c_1} \right) \\ &\quad - C_3 (2L - y) \cos(2\omega t - 2k_1(2L - y)), \end{aligned} \quad (3.219)$$

$$\begin{aligned} \dot{v}^{(r)}(y, t) &= -\frac{Q_1 c_1}{\lambda + 2\mu} \sin(\omega t - k_1(2L - y)) \\ &\quad + 2\omega C_7 \cos(2\omega t - 2k_1(2L - y)) - C_8 \\ &\quad + 2\omega C_3 (2L - y) \sin(2\omega t - 2k_1(2L - y)) \\ &\quad \text{for } \Delta t \geq t - \frac{2L - y}{c_1} \geq 0. \end{aligned} \quad (3.220)$$

As mentioned before, the solution presented is only valid for domains where incident and reflected wave are completely separated.

3.3.3 Reflection at a Stress-Free Boundary

Now, the same problem is considered but with a stress-free boundary at $y = L$. All other assumptions are identical to those in the previous subsection. Formally, the

boundary condition can be written as

$$\sigma_{yy}(x, y = L, t) = 0 \quad (3.221)$$

$$\sigma_{xy}(x, y = L, t) = 0 \quad (3.222)$$

whereas the second boundary condition is automatically fulfilled in the problem considered.

The subsequent derivation of the reflected wave will be close to the previous one for the rigid boundary, so only an abbreviated version is presented in the following. Beginning again with the linear case, it can easily be verified that

$$v_1^{(r)}(y, t) = -\frac{Q_1}{k_1(\lambda + 2\mu)} (\cos(\omega t - k_1(2L - y)) - 1) \quad (3.223)$$

for $\Delta t \geq t - \frac{2L - y}{c_1} \geq 0,$

together with the fundamental incident wave in Eq. (3.206), fulfills boundary condition (3.221). As above, the reflected fundamental wave is used on the right side of the partial differential equation that describes the correction term $v_2^{(r)}$ in the nonlinear case. However, by inspection of Eq. (3.213), it can be recognized that inserting Eq. (3.223) yields the same partial differential equation and thus, also the same general solution as in the case for the rigid boundary. This means that Eq. (3.215) also applies for the situation of a stress-free boundary at the opposite side of the plate. Again, the term $f(\omega t - k_1 y)$ is disregarded a priori for the same reasons as above while the term $g(\omega t + k_1 y)$ has to be determined from boundary condition (3.221). It is rewritten as

$$\sigma_{yy}(x, L, t) = \sigma_{yy}^{(i)}(x, L, t) + \sigma_{yy}^{(r)}(x, L, t) = 0. \quad (3.224)$$

Therefore, both the incident wave (3.207) and the general form of the reflected wave (3.215) have to be formulated as stress waves. This can easily be accomplished

by making use of the nonlinear constitutive equation (3.65). Then, after some mathematical manipulation, it is found that the desired term is

$$g(\omega t + k_1 y) = \frac{3}{2} C_7 \sin(2\omega t - 2k_1(2L - y)) - C_8 \left(t + \frac{y}{c_1} \right) + G. \quad (3.225)$$

The undetermined constant term G arises because Eq. (3.224) actually represents a boundary condition on the derivative of $g(\omega t + k_1 y)$ meaning that the boundary condition is fulfilled for every constant G . It has to be determined from other considerations later on.

Now, inserting the result found into Eq. (3.215) yields the correction term $v_2^{(r)}$. Adding this to the solution to the fundamental wave (3.223) provides the total solution to the displacement $v^{(r)}$. The only task remaining is the determination of the constant G . The condition applied here is that all of the terms occurring in the total solution must have a common wavefront since all parts of the wave field arising have to travel with the wave speed c_1 . This means that the static displacement term has also to be a function of the argument $t - \frac{2L-y}{c_1}$. If this additional constraint is applied to the solution, the total displacement field $v^{(r)}$ of the reflected wave becomes

$$\begin{aligned} v^{(r)}(y, t) = & -\frac{Q_1}{k_1(\lambda + 2\mu)} (\cos(\omega t - k_1(2L - y)) - 1) \\ & + C_7 \sin(2\omega t - 2k_1(2L - y)) \\ & + C_3 y \cos(2\omega t - 2k_1(2L - y)) \\ & - C_8 \left(t - \frac{2L - y}{c_1} \right) \end{aligned} \quad (3.226)$$

for $\Delta t \geq t - \frac{2L - y}{c_1} \geq 0$.

The respective particle velocity field $\dot{v}^{(r)}$ is then given by

$$\begin{aligned}
\dot{v}^{(r)}(y, t) = & \frac{Q_1 c_1}{\lambda + 2\mu} \sin(\omega t - k_1(2L - y)) \\
& + 2\omega C_7 \cos(2\omega t - 2k_1(2L - y)) \\
& - 2\omega C_3 y \sin(2\omega t - 2k_1(2L - y)) \\
& - C_8
\end{aligned} \tag{3.227}$$

$$\text{for } \Delta t \geq t - \frac{2L - y}{c_1} \geq 0.$$

CHAPTER IV

NUMERICAL SIMULATION OF NONLINEAR WAVE PROPAGATION

A major goal of this research is the numerical investigation of wave propagation developing in an elastic material with a quadratic nonlinearity in its stress-strain relationship. Therefore, a simulation code that is based on the numerical solver CentPack [2] is applied. This solver was adapted to handle two-dimensional nonlinear wave propagation problems in plane strain by Küchler [12], [13]. In this chapter, a brief description of the simulation model applied and the simulation procedure is presented.

4.1 Description of the Simulation Model

4.1.1 Numerical Scheme

The numerical scheme that is applied in the simulations of this research is a high-resolution semi-discrete central scheme for a two-dimensional domain as presented in [14]. “Semi-discrete” means here that only the spatial domain is discretized while the evolution in time has to be solved with any ODE solver (here, an explicit second-order Runge-Kutta method is used). The meaning of the term “central scheme” in contrast to an “upwind scheme” is given in [12] but an important point is that such schemes are independent on the eigenstructure of a system considered. The package CentPack includes such a scheme for hyperbolic systems of conservation laws. A conservation law is a system of first-order partial differential equations and has in the

two-dimensional case the general form

$$\frac{\partial \mathbf{v}}{\partial t} + \frac{\partial}{\partial x} \mathbf{f}(\mathbf{v}) + \frac{\partial}{\partial y} \mathbf{g}(\mathbf{v}) = \mathbf{0}, \quad [x, y] \in \mathbb{R}^2, t > 0 \quad (4.1)$$

where the vector of state \mathbf{v} is a function of x , y and t . The functions \mathbf{f} and \mathbf{g} are vector-valued and called flux functions. This conservation law is called hyperbolic if the matrix \mathbf{H} which is given by

$$\mathbf{H}(\mathbf{v}, \boldsymbol{\omega}) = \mathbf{B} \cdot \omega_x + \mathbf{C} \cdot \omega_y \quad (4.2)$$

has only real eigenvalues with a complete family of eigenvectors for any \mathbf{v} and any real unit vector $\boldsymbol{\omega} = [\omega_x, \omega_y]^T$. The terms \mathbf{B} and \mathbf{C} are the Jacobian matrices of the flux functions \mathbf{f} and \mathbf{g} , respectively. A detailed description of the numerical scheme applied is presented in [12]. A comprehensive disquisition on hyperbolic conservation laws and their numerical treatment is given in [4].

4.1.2 Implementation

In order to simulate two-dimensional nonlinear wave propagation with the scheme described above, the problem statement that has already been presented in Chapter 3 has to be transformed into the form of a conservation law. The complete problem statement consists of the two-dimensional wave equations (3.91) and (3.92) and the appropriate constitutive equations presented in Eqs. (3.200) - (3.202); initial and boundary conditions will be used later on. At first, the state vector \mathbf{q} which represents the numerical approximation of \mathbf{v} is defined here as

$$\mathbf{q} = \begin{bmatrix} q^1 \\ q^2 \\ q^3 \\ q^4 \\ q^5 \end{bmatrix} = \begin{bmatrix} \dot{u} \\ \dot{v} \\ u_x \\ v_y \\ u_y + v_x \end{bmatrix}. \quad (4.3)$$

This definition is used to rewrite the two wave equations so that the problem statement can be expressed as a conservation law in terms of \mathbf{q} as

$$\begin{bmatrix} q^1 \\ q^2 \\ q^3 \\ q^4 \\ q^5 \end{bmatrix}_{,t} + \begin{bmatrix} -\frac{1}{\rho}\sigma_{xx}(q^3, q^4, q^5) \\ -\frac{1}{\rho}\sigma_{xy}(q^3, q^4, q^5) \\ -q^1 \\ 0 \\ -q^2 \end{bmatrix}_{,x} + \begin{bmatrix} -\frac{1}{\rho}\sigma_{xy}(q^3, q^4, q^5) \\ -\frac{1}{\rho}\sigma_{yy}(q^3, q^4, q^5) \\ 0 \\ -q^2 \\ -q^1 \end{bmatrix}_{,y} = \mathbf{0}. \quad (4.4)$$

Clearly, it is $q^i = q^i(x, y, t)$. The initial condition that has to be specified in order to complete the problem statement is always given by Eqs. (3.89) and (3.90) while the boundary conditions applied in the simulations depend on the specific problem considered. Before these boundary are discussed in more detail, a brief remark on the hyperbolicity of the conservation law (4.4) is given. It shall be pointed out that this hyperbolicity is not assured in general but it can be shown that it is guaranteed in the case of the linear constitutive equations. However, since the numerical scheme applied is only valid for conservation laws which are always hyperbolic at every point of the domain it has to be made sure that, according to the above description of hyperbolicity, the matrix \mathbf{H} has only real eigenvalues. In [12], it is shown that this can be established if the values of the spatial derivatives of the displacements, that is q^3 , q^4 and q^5 , are limited. Since these spatial derivatives always correlate with the amplitude of the input signal that excites the wave propagation in the domain, the hyperbolicity of the conservation law can be guaranteed if the input signal is chosen small enough. Note that this is no additional constraint to the simulation model because small strain has been assumed in the derivation of the constitutive equations (3.200) - (3.202).

The last point that has to be mentioned is the definition of appropriate boundary conditions. In this research, two basic situations are considered. Most of the time, a two-dimensional half-space is considered as domain at whose surface, a traction

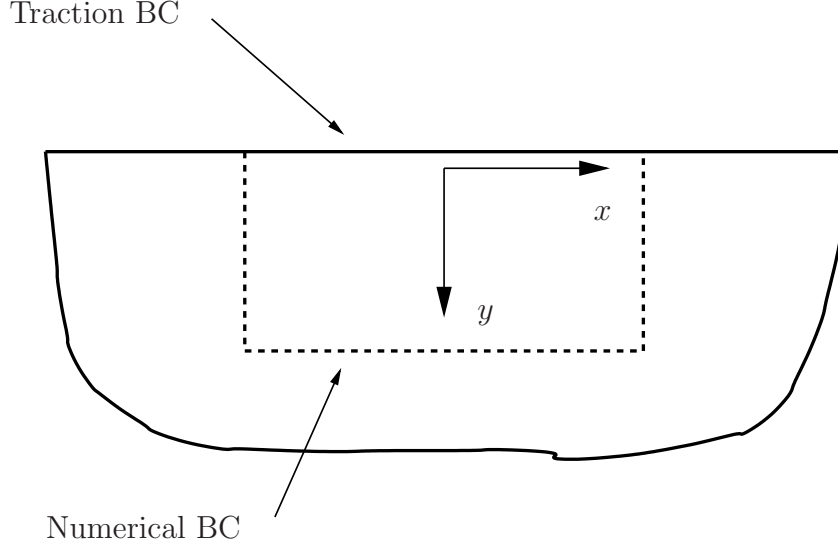


Figure 4.1: Numerical domain representing a half-space with a traction boundary condition at its surface.

boundary condition is applied. The other situation is the simulation of a plate with a finite thickness. Here, either a traction or a displacement boundary condition is applied at each side. Note that, using the package CentPack, only rectangular domains can be realized. This means that every domain simulated has always to have four borders which have all to be expressed as an appropriate boundary condition. Because it is obviously impossible to simulate half-infinite domains, some of the four borders are realized as numerical boundary conditions that absorb any incident wave. At these boundaries, no reflections into the domain under consideration occur and thus, the same wave field arises in this domain as in the respective part of a domain with half-infinite dimensions. The two situations are depicted in Figs. 4.1 and 4.2. The domains shown have to be completely discretized with cells having appropriate spatial dimensions Δx and Δy . How these values have to be chosen is explained in the next subsection. At this point, it is pointed out that the (different) boundary conditions are always realized by the so-called ghost cells method. This method is based on the introduction of additional layers of cells surrounding the actual domain that is to be simulated. These additional cells are called ghost cells and are used to

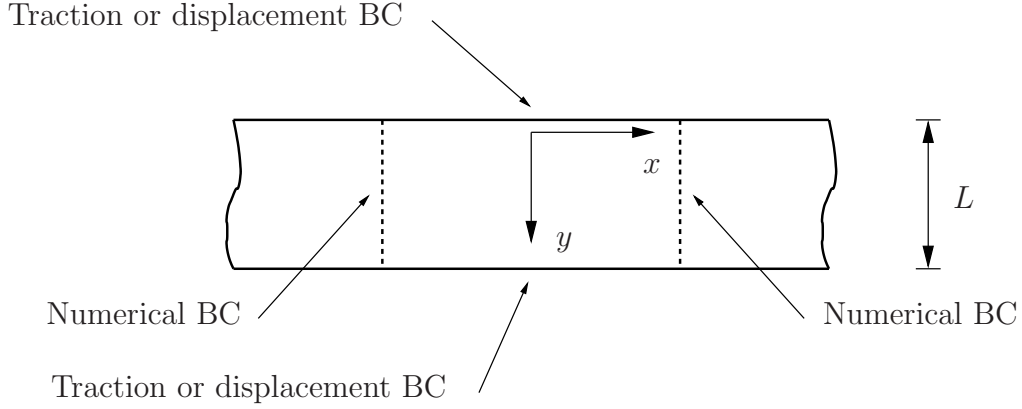


Figure 4.2: Numerical domain representing a plate with different boundary conditions applied at its surfaces.

realize the boundary condition that belongs to the respective border. For a detailed description, the interested reader is again referred to [12], but the basic procedure is as follows: the values of the state q^i in the ghost cells are chosen in a way that the specific boundary condition prescribed is fulfilled. For example, if the traction is prescribed, the states q^3 , q^4 and q^5 which represent the spatial derivatives of the displacements are set in the ghost cells in such a way that, according to the constitutive equations (3.200) - (3.202), the average stresses between the outer cells of the domain and the ghost cells fulfill the boundary condition. On the other hand, if the displacement at a boundary is specified, the states q^1 and q^2 which denote the particle velocities are determined in the ghost cells in a way so that the average displacements between the outer cells and the ghost cells obey to the values prescribed. The respective components of the vector of state not involved in the boundary condition are extrapolated symmetrically

4.1.3 Evaluation

An important factor for the numerical simulation of wave propagation is the determination of an appropriate discretization of the domain. Since ultrasonics are considered in this research, it can be easily imagined that the grid will have to be very fine in

order to resolve the short-wave appearance of the wave field arising. However, the fineness of the discretization has an extremely strong influence on the computational efforts needed. For example, reducing the cell length $\Delta x = \Delta y$ (only squarish cells are used for the simulations) by factor of 2 approximately increases the calculation time by factor of 8. The reason is that not only the number of cells grows by factor of 4 but also that the numerical scheme, according to the spatial discretization, applies a smaller time step in the calculation of the results. Thus, an acceptable compromise for the discretization must be found. In [12], a sufficiently fine discretization was determined by the numerical solution of the linear Lamb's problem and comparing this solution to the analytical solution that has been presented in Section 3.2. It was shown that one wavelength should be discretized with at least about 60 cells in order to reach an acceptable convergence to the analytical solution in both the time and the frequency domain. This reference value is the basis for the simulations done in the frame of this research. However, the exact discretization used for each simulation will be always presented together with the numerical results presented in Chapter 5.

4.2 Description of the Simulation Procedure

In this section, a short remark on the general procedure of running a simulation with the simulation code described is presented.

The starting point for the simulations performed in the frame of this research has been the source code which Küchler had used in his research [12], [13]. It has been written in C++. Clearly, in order to adapt the code to the problems investigated here and to increase its performance regarding convenience of usage and the reduction of calculation time, numerous changes and enhancements have been implemented. The two most important changes are explained in the following.

First, a convenient way of defining different boundary conditions at the borders of the simulation domain has been introduced. On the one hand, this includes that different

types of boundary conditions (traction BC, displacement BC or absorbing BC) can be realized at the four borders of the domain. Therefore, the code has become able to simulate a couple of different problems. However, only the situations shown in Figs. (4.1) and (4.2) are discussed in this thesis. On the other hand, spatially more complex boundary conditions can be defined with the enhancements made. While the original version of the code was mainly used to model a point source (corresponding to a line source applied to a three-dimensional half-space) at a stress-free boundary (Lamb's problem), the current version is able to realize boundary conditions with an arbitrary shape along the boundary. One example is the transducer model with a finite size which shall provide insight into the actual wave field excited by a transducer in a real experiment. It is presented in the Chapter 5.

The second major enhancement is the parallelization of the source code in order to increase the performance of computation. This action has become necessary because the calculation times for some of the simulations would have become unrealistically long without such a parallelization. Since a computer cluster whose nodes have been equipped with multi-core processors (described in more detail later on) has been available, the application programming interface OpenMP (Open Multi-Processing) has been applied which is intended to be used together with shared memory systems. Because the original source code had featured a relatively high level of parallelizability, an effective speedup $S_4 \approx 3$ could be achieved on the computer nodes used which are equipped with four cores each.

The computer system used for this research is a computer cluster consisting of 16 independent nodes. These nodes are DELL PowerEdge 1950 servers which are equipped with two Dual-Core Intel Xeon processors with a clock rate of 3.00 GHz and a memory of 8 GB.

Lastly, the single steps of the simulation procedure are described schematically in order to illustrate the course of action:

1. Definition of the simulation parameters in four input text files. There is one input file for the definition of the simulation domain, simulation length and certain numerical parameters, one for the description of the material parameters and the appearance of the input signal (duration, frequency, amplitude), another one defines a map of positions in the domain where the time signal simulated is to be saved to the output files and the last one includes the spatial distribution of an amplitude prefactor which controls the appearance of the boundary condition.
2. Compilation of the source code. The source code is compiled using an OpenMP-capable compiler.
3. Simulation. Output text files are generated which include the time domain data of particle displacements, particle velocities, strains and stresses according to the definitions made in the input files. The calculation time depends mainly on the size of the domain, the discretization and the length of the simulation. In this research, it has varied for the different problems simulated between a couple of minutes and several weeks.
4. Generation of the data desired. In this step, the data actually needed are selected from the raw data saved in the output files. This is important because the output files obtained from the simulation are typically too big to be handled efficiently on a standard computer so that the data desired have to be saved to smaller files. Optionally, a coordinate transformation to polar coordinates can be executed in this step.
5. Postprocessing. In the last step, signal processing and evaluation of the data are performed with MATLAB. Results from different simulations are compared and presented in figures.

CHAPTER V

NUMERICAL RESULTS

This chapter applies the numerical code developed in the previous chapter to investigate problems affiliated with the determination of the nonlinearity present in a half-space's material. As discussed earlier, the amount of nonlinearity present in the stress-strain relationship of a component's material is related directly to the amount of microplasticity induced damage. Since changes in the nonlinearity of a material are much more reflected in changes in the third-order elastic constants than in changes in the second-order elastic constants, it is desired to find possibilities to measure changes in these third-order elastic components of a real component's material. Thus, wave propagation in a component due to a transducer applied at a plane stress-free surface is simulated. This research considers a half-space subjected to different boundary conditions at its surface which model a transducer source. The half-space is chosen as the "component" examined because its geometry is close to many plate-like structural components whose investigation is of considerable practical interest, while it is still providing a relatively simple wave field compared to more complex structures. However, the focus of this research is only on the investigation of one- and two-dimensional problems since the simulation code applied is not capable of handling real three-dimensional problems. This means that only special wave propagation problems depending only on two spatial directions can be reproduced. More specifically, this means that the boundary condition applied to a three-dimensional half-space's surface must be constant at least over one spatial direction. Therefore, the simulations performed here have to be seen as approximations to actual experimental setups including the application of a transducer to a stress-free plane surface.

The validity of these approximations clearly depends on the respective situation. At the beginning of this chapter, one-dimensional problems which are due to a boundary condition being a spatially constant traction over the whole surface are considered. At large distances from the transducer that excites the wave field arising, these problems are reasonable approximations to the situation of a real transducer emitting waves into a plate. The results obtained are compared to the analytical solutions which were presented in Chapter 3.

Subsequently, two-dimensional problems are simulated that provide more realistic results concerning a real experimental setup. They are modeled by the application of a line source at the surface of the half-space. However, in the case of a nonlinear-elastic material, no analytical solutions describing the wave fields arising are available. Clearly, this fact makes a quantitative analysis of the data obtained difficult but similarities to the one-dimensional problems are discussed.

Another objective of this research is the investigation of the effects appearing due to a more realistic modeling of an actual transducer and possible limitations to the practical measurement of a material's nonlinearity. Therefore, the transducer is modeled as realistically as possible in the frame of the restriction that only two-dimensional wave propagation can be simulated here. This means that the transducer model gets a finite size and the spatial distribution of the surface traction is shaped like a Gaussian.

At the end of this chapter, reflections of a one-dimensional incident plane wave at both a rigid and a stress-free boundary are examined. The results obtained by the simulations are compared to the analytical approximate solutions given in Chapter 3. It is suggested how these reflection effects can be used in an experimental measuring of the third-order elastic constants.

Table 5.1: Material parameters of Aluminum D54S.

ρ [$\frac{\text{kg}}{\text{m}^3}$]	λ [$\frac{\text{N}}{\text{m}^2}$]	μ [$\frac{\text{N}}{\text{m}^2}$]	l [$\frac{\text{N}}{\text{m}^2}$]	m [$\frac{\text{N}}{\text{m}^2}$]
2719	4.91×10^{10}	2.6×10^{10}	-38.75×10^{10}	-35.8×10^{10}

5.1 *Half-Space Subjected to a Uniform Surface Traction*

In this section, the situation of a half-space whose surface is subjected to a harmonic uniform load is investigated. The half-space is initially at rest. Three different problems are considered that vary in the load applied. The first load is a pure pressure traction, the second one a pure shear traction and the third one a combination of pressure and shear traction.

The material used in the simulations throughout this thesis is Aluminum D54S. Its third-order elastic constants (TOEC) l and m can be found in [23] and are presented together with its other relevant material parameters, the density ρ and the Lamé constants λ and μ , in Table 5.1. The third TOEC n is not listed there because it does not appear in the constitutive equations (3.200) - (3.202) that apply. However, note that the values for the TOEC have been varied systematically in the subsequent simulations in order to illustrate how the nonlinearity of the material influences the wave field arising. The way in which the TOEC are changed will be presented in the legends of the figures that show the results of the simulations. The simulation parameters that have been used for the subsequent simulations are presented in Table 5.2: the frequency f_f of the harmonic input signal, the reference stress Q that is used to describe the traction boundary condition in the following and the lengths of the grid cells Δx and Δy which express the fineness of the domain's discretization.

Table 5.2: Simulation parameters used for the one-dimensional problems.

f_f [MHz]	Q [$\frac{\text{N}}{\text{mm}^2}$]	Δx [m]	Δy [m]
5.0	2.22	4.5×10^{-6}	4.5×10^{-6}

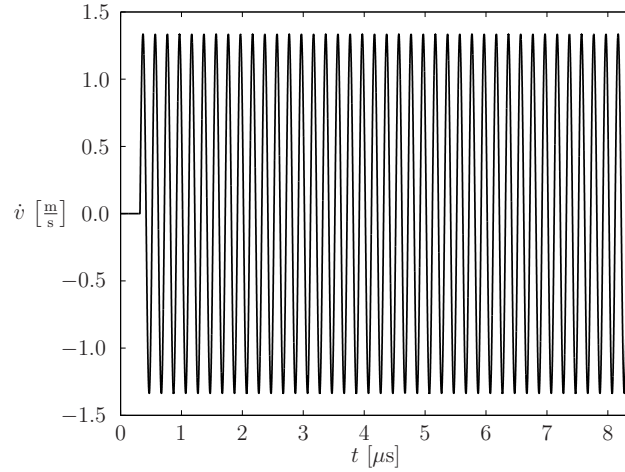


Figure 5.1: Particle velocity in y -direction at $\bar{y} = 2$ mm.

5.1.1 Pure Pressure Traction

In this subsection, the situation of a half-space subjected to a pure pressure boundary condition is considered. Clearly, this is the simplest boundary condition that can be applied and will generate only a one-dimensional wave field without any dependency on the spatial coordinate x . Furthermore, for reasons of symmetry, it is obvious that there cannot be any particle motion in x -direction. The coordinate system that is used here is shown in Fig. 4.1. According to the notation of Chapter 3, the boundary condition applied in this simulation can be formulated as $Q_1 = 10Q$ and $Q_2 = 0$.

In Fig. 5.1, the time signal of the particle velocity in the direction of wave propagation (here, the y -direction) at $\bar{y} = 2$ mm is shown. It is recognizable that the wave front arrives at the time $\bar{t} = \frac{\bar{y}}{c_1} = 0.33 \mu\text{s}$. Afterwards, a purely sinusoidal oscillation with periodic time $T = 0.2 \mu\text{s}$ seems to develop; clearly, this periodic time is due to

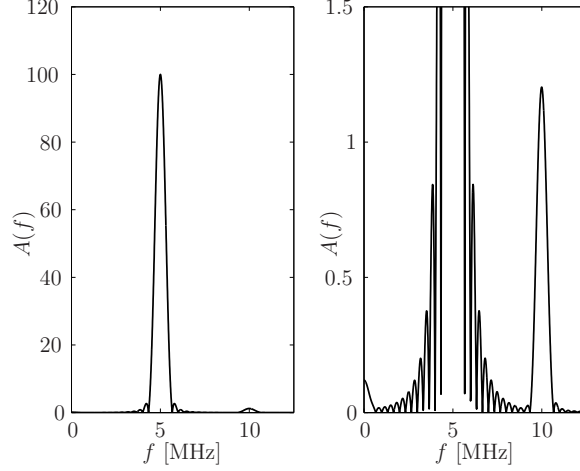


Figure 5.2: FFT of the particle velocity in y -direction at $\bar{y} = 2$ mm. The magnitude is normalized to its peak value.

the excitation frequency $f_f = 5$ MHz. This fact shows a general issue of nonlinear wave propagation problems – the nonlinear effects are typically small compared to the dominating linear behavior and thus, the time domain is relatively inappropriate for a detailed investigation of such effects. Therefore, throughout this research, the time signals obtained from the simulations are transformed to the frequency domain in order to analyze these effects. This procedure is realized by the application of an FFT to a sufficiently long part of the signal when a steady state has been reached. Note that a Hanning window [21] is used in order to avoid the disturbing influence of fringe effects. The frequency domain representation of the time signal in Fig. 5.1 is shown in Fig. 5.2. The range of frequency is limited there to 12.5 MHz. The reason for this limit is the fact that effects correlated to even higher frequencies cannot be expected to be resolved correctly because of the discretization used in the simulations. Note that higher frequencies correspond to shorter wavelengths and that shorter wavelengths require a finer discretization. However, as described in Chapter 4, the fineness of the discretization cannot be increased arbitrarily because of the computational efforts. Thus, this research is restricted to the frequency range mentioned, meaning that second-harmonic effects at $f_2 = 2f_f = 10$ MHz are the highest-harmonic

effects considered in this research.

Figure 5.2 presents the magnitude of the signal and shows clearly what has been concluded from the time signal – the peak belonging to the fundamental frequency $f_1 = f_f$ is dominant. However, it can also be seen that there are parts of the wave field related to $f_0 = 0$ MHz and $f_2 = 10$ MHz. Note that the magnitude is scaled to its maximum value because the absolute value does not have a physical meaning.

In the following, the signals will only be analyzed in the frequency domain. The procedure will always be as described above – the explicit presentation of time domain results is set aside here in order to keep as much clarity as possible. Additionally, the following notation is introduced: the peak magnitudes of the particle velocity in the direction of wave propagation (the y -direction for the one-dimensional problems presented here) at the harmonic frequencies f_0 , f_1 , f_2 will be called A_0 , A_1 and A_2 . Accordingly, the terms B_0 , B_1 and B_2 are introduced for the peak magnitudes of the particle velocity in the direction normal to the direction of wave propagation. The latter ones will be needed later on for more complex wave fields. With this new terminology, it is possible to present the results from the simulations in a more compact fashion. Then, the outcome of an FFT as shown in Fig. 5.2 can be summarized for different positions in the domain in one plot. This will be the way the results obtained are presented in the following.

5.1.1.1 *Second-Harmonic Effects*

In this paragraph, the appearance of A_2 over propagation distance y is presented. Note that A_2 is normalized to A_1^2 in the following because this has been the way comparable results have been presented previously, for example in [5] or [7]. Furthermore, no absolute values for this ratio are provided because those would reflect an inherent influence of the FFT applied. Instead, the ratio has been normalized to the maximum value that occurs in the respective figure.

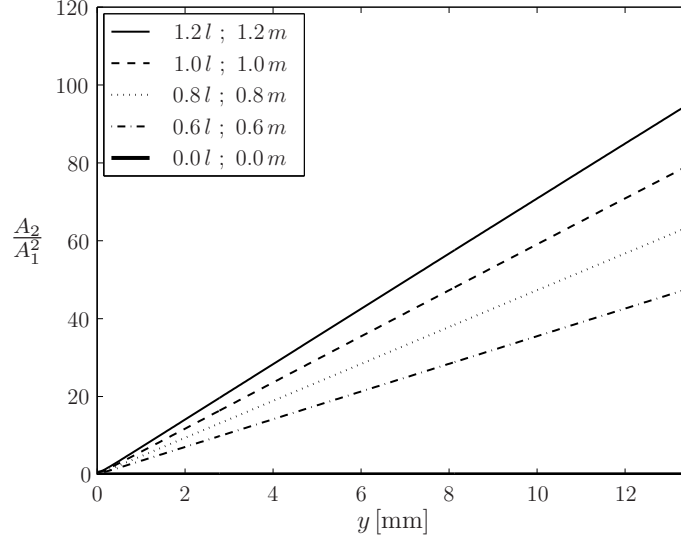


Figure 5.3: Normalized ratio $\frac{A_2}{A_1^2}$ over the propagation distance y for different values of the third-order elastic constants.

Figure 5.3 presents the ratio $\frac{A_2}{A_1^2}$ over the propagation distance y for different combinations of the TOEC. It is shown in the legend that the TOEC used are varied by multiplying the TOEC of Aluminum D54S according to Table 5.1 with different factors. In this figure, l and m are always multiplied by the same factor. One can recognize a linear growth of the ratio with the propagation distance where the slope depends on the TOEC. Generally, it can be remarked that the slope increases for higher TOEC. In order to investigate how the graphs exactly change, the ratio $\frac{A_2}{A_1^2}$ for each combination of TOEC is divided by the specific ratio obtained for the combination with the original TOEC values of Aluminum D54S. The result is shown in Fig. 5.4. It can be concluded that the ratio $\frac{A_2}{A_1^2}$ has to depend linearly on a specific linear combination of l and m because the factors they have been multiplied with can be directly recognized as scaling factors.

The numerical data are now compared to the analytical solution provided in Chapter 3. Making use of the fact that $Q_2 = 0$, Eq. (eq:4723) can be used to find analytical

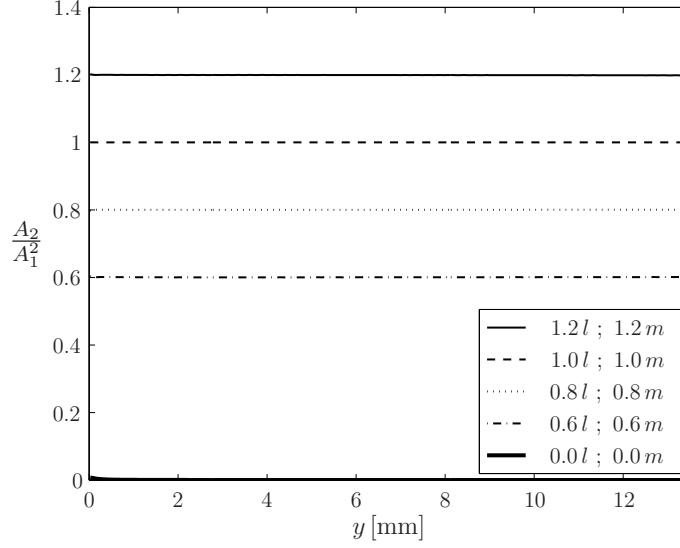


Figure 5.4: Ratio $\frac{A_2}{A_1^2}$ over the propagation distance y for different values of the third-order elastic constants, normalized to the specific ratio obtained for the TOEC of Aluminum D54S.

expressions for A_1 and A_2 . This yields

$$A_1 = \frac{c_1 Q_1}{\lambda + 2\mu} \quad (5.1)$$

$$A_2 = \frac{\omega |l + 2m| Q_1^2}{2(\lambda + 2\mu)^3} \sqrt{y^2 + \frac{1}{4k_1^2}} \quad (5.2)$$

$$\frac{A_2}{A_1^2} = \frac{\omega |l + 2m|}{2(\lambda + 2\mu) c_1^2} \sqrt{y^2 + \frac{1}{4k_1^2}}. \quad (5.3)$$

This shows that the ratio is actually proportional to a linear combination of the TOEC. Note that the absolute value of this combination occurs above because the TOEC can be (and here, actually are) negative. Furthermore, one can recognize that the value of the ratio depends more sensitively on m than on l . Thus, a change of m will result in a stronger change in the slope of the graph. Another interesting point is the spatial dependency; one can see that the behavior is only linear for $y \gg \frac{1}{2k_1}$. In Fig. 5.5, a closer look at Fig. 5.3 for small y is provided. It shows the behavior predicted by Eq. (5.3). In order to conclude this paragraph, it shall be remarked that, for the traction presently applied at the half-space's surface ($Q_2 = 0$), no particle

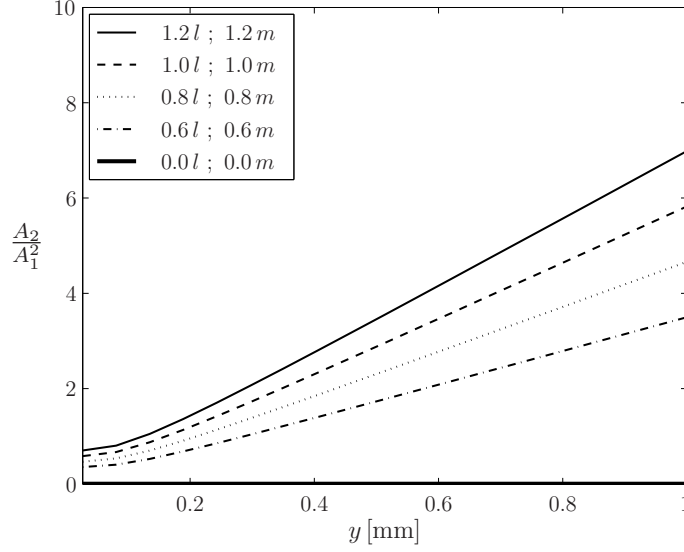


Figure 5.5: Normalized ratio $\frac{A_2}{A_1^2}$ over the propagation distance y for different values of the third-order elastic constants, focused on small y .

displacement in x -direction arises. Lastly, several figures (Figs. 5.6 - 5.9) showing the higher sensitivity of $\frac{A_2}{A_1^2}$ on changes in m than on l as explained above are presented.

5.1.1.2 Static Effects

Now, the appearance of static effects in the particle velocity at $f_0 = 0$ MHz shall be investigated. Therefore, the ratio $\frac{A_0}{A_1^2}$ is defined in analogy to the one used in the previous paragraph. The subsequent proceeding is absolutely identical to that for the second-harmonic effects. The behavior of $\frac{A_0}{A_1^2}$ over the propagation distance is shown in Figs. 5.10 and 5.11, the normalization used is exactly the same as for the investigation of the second-harmonic effects. Figure 5.10 shows two basic facts. First, there does not seem to be any spatial dependency of $\frac{A_0}{A_1^2}$, its value is constant for every position y . Second, there has to be a similar dependency on the TOEC as for $\frac{A_2}{A_1^2}$ if they are varied. This can be seen in more detail in Fig. 5.11 where one can recognize that the ratio $\frac{A_0}{A_1^2}$ has again to depend linearly on a linear combination of the TOEC because the factors used to vary the TOEC appear as scaling factors of

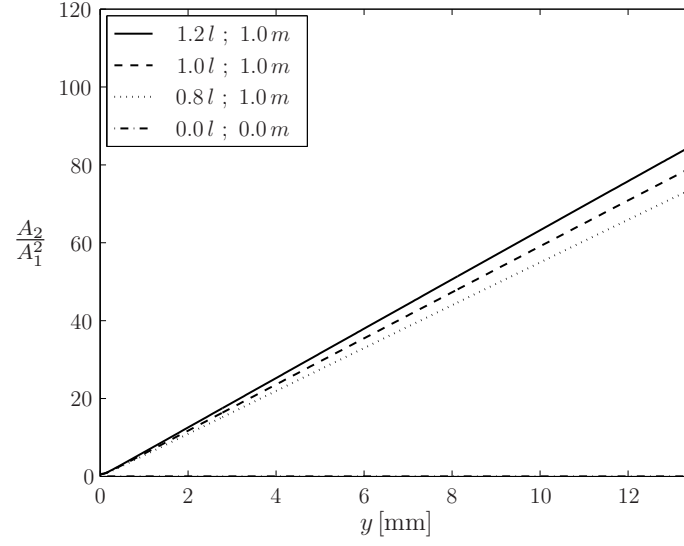


Figure 5.6: Normalized ratio $\frac{A_2}{A_1^2}$ over the propagation distance y for different values of the third-order elastic constants.

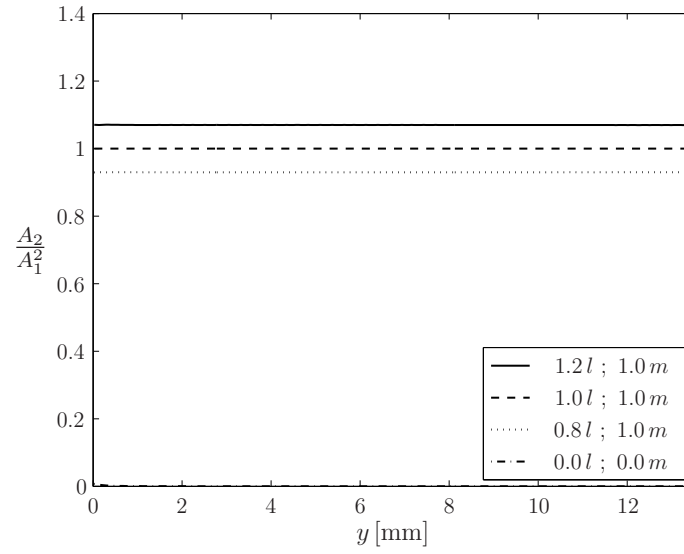


Figure 5.7: Ratio $\frac{A_2}{A_1^2}$ over the propagation distance y for different values of the third-order elastic constants, normalized to the specific ratio obtained for the TOEC of Aluminum D54S.

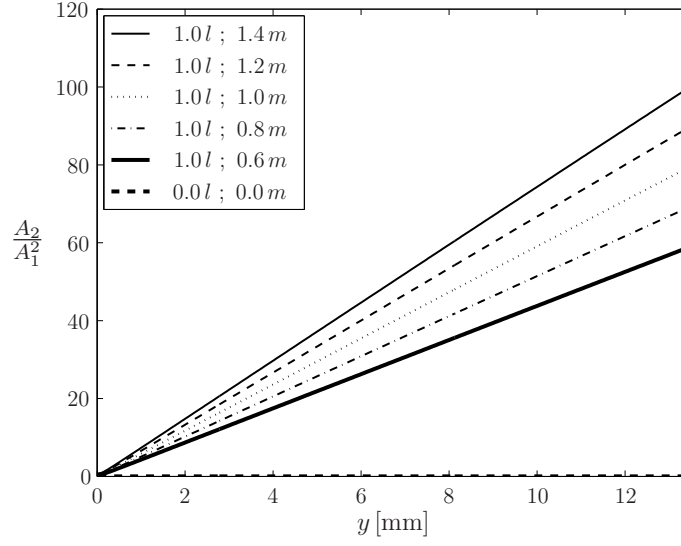


Figure 5.8: Normalized ratio $\frac{A_2}{A_1^2}$ over the propagation distance y for different values of the third-order elastic constants.

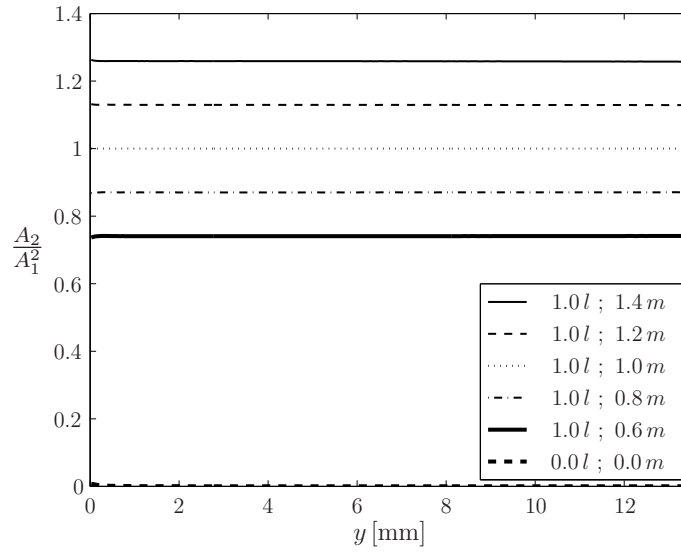


Figure 5.9: Ratio $\frac{A_2}{A_1^2}$ over the propagation distance y for different values of the third-order elastic constants, normalized to the specific ratio obtained for the TOEC of Aluminum D54S.

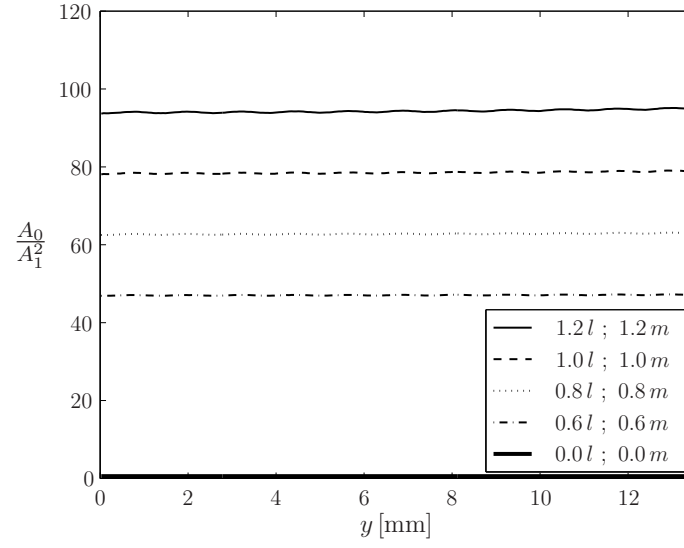


Figure 5.10: Normalized ratio $\frac{A_0}{A_1^2}$ over the propagation distance y for different values of the third-order elastic constants.

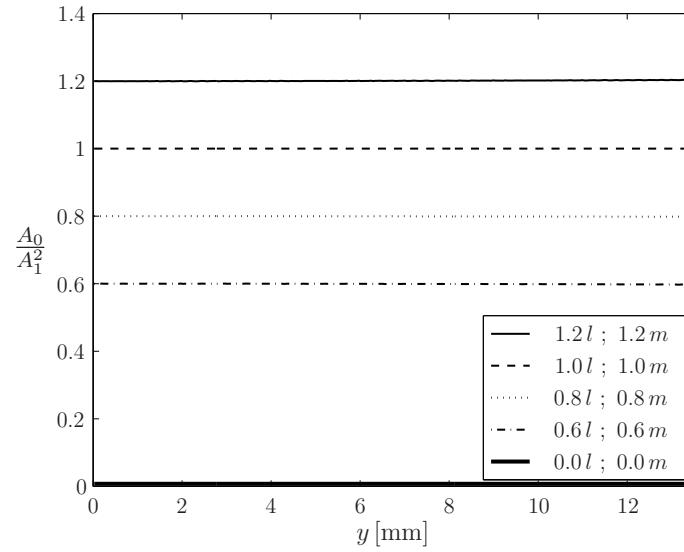


Figure 5.11: Ratio $\frac{A_0}{A_1^2}$ over the propagation distance y for different values of the third-order elastic constants, normalized to the specific ratio obtained for the TOEC of Aluminum D54S.

the ratio.

Having again a look at Eq. (3.86), one can find the analytical expressions

$$A_0 = \frac{|l + 2m| Q_1^2}{2 \rho c_1 (\lambda + 2\mu)^2} \quad (5.4)$$

$$A_1 = \frac{c_1 Q_1}{\lambda + 2\mu} \quad (5.5)$$

$$\frac{A_0}{A_1^2} = \frac{|l + 2m|}{2 c_1 (\lambda + 2\mu)}. \quad (5.6)$$

Equation (5.6) confirms that there is neither a spatial dependency of the magnitude A_0 nor of the ratio $\frac{A_0}{A_1^2}$. Moreover, it shows that the ratio is proportional to $|l + 2m|$, just as the ratio $\frac{A_2}{A_1^2}$ describing the second-harmonic effect. This dependency is again illustrated in Figs. 5.12 - 5.15 by varying only one TOEC systematically while the other one is kept constant. It is again recognizable that a change in m has a more significant impact on the ratio $\frac{A_0}{A_1^2}$ than the same change in l .

Finally, a remark on the practical importance of the second-harmonic and the static effect shall be given. Clearly, both can be used to investigate the current appearance of the term $|l + 2m|$ in a nonlinear material by determining either A_2 and A_1 or A_0 and A_1 from a measurement. However, if these values cannot be obtained in an absolute way because of the FFT which has to be applied, it is only possible to determine changes between two different states of a material. More specifically, this means that one has to have one measurement in an “initial” state of the material and to find the peak values mentioned with an appropriate FFT. Then, one can repeat the measurement in a “current” state of the material and determine the new peak values with the same signal processing. The change of $\frac{A_2}{A_1^2}$ or $\frac{A_0}{A_1^2}$ has to be the same change as in the parameter $|l + 2m|$.

5.1.2 Pure Shear Traction

The second scenario that may be useful for the determination of the TOEC is the model of a half-space subjected to a pure shear boundary condition. Like the pure

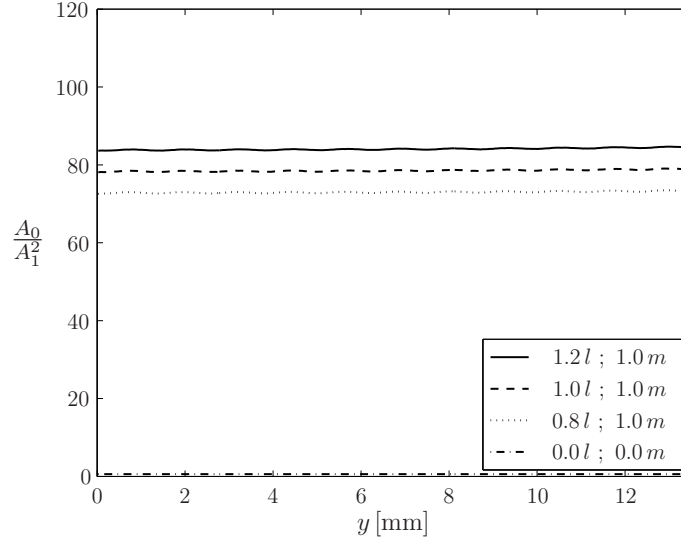


Figure 5.12: Normalized ratio $\frac{A_0}{A_1^2}$ over the propagation distance y for different values of the third-order elastic constants.

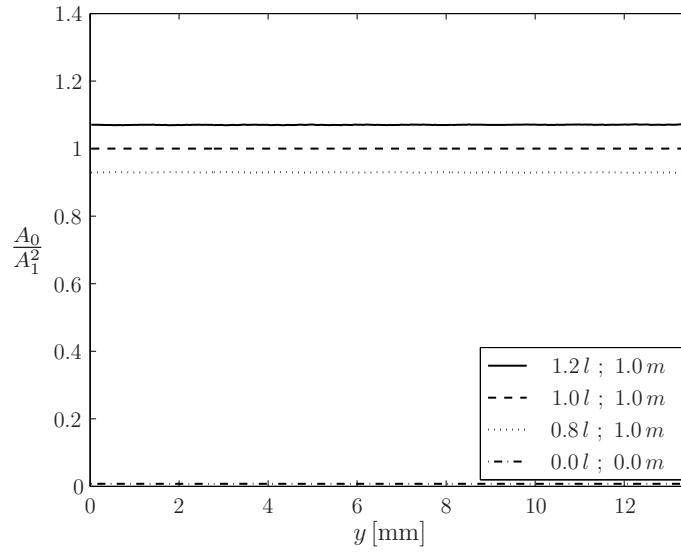


Figure 5.13: Ratio $\frac{A_0}{A_1^2}$ over the propagation distance y for different values of the third-order elastic constants, normalized to the specific ratio obtained for the TOEC of Aluminum D54S.

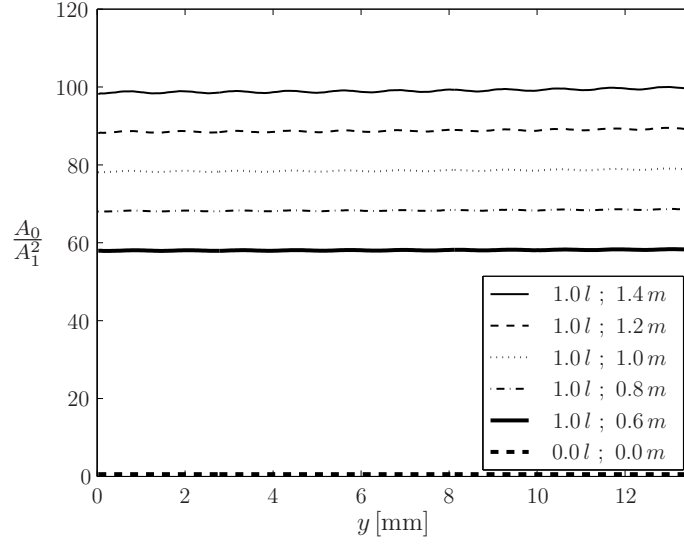


Figure 5.14: Normalized ratio $\frac{A_0}{A_1^2}$ over the propagation distance y for different values of the third-order elastic constants.

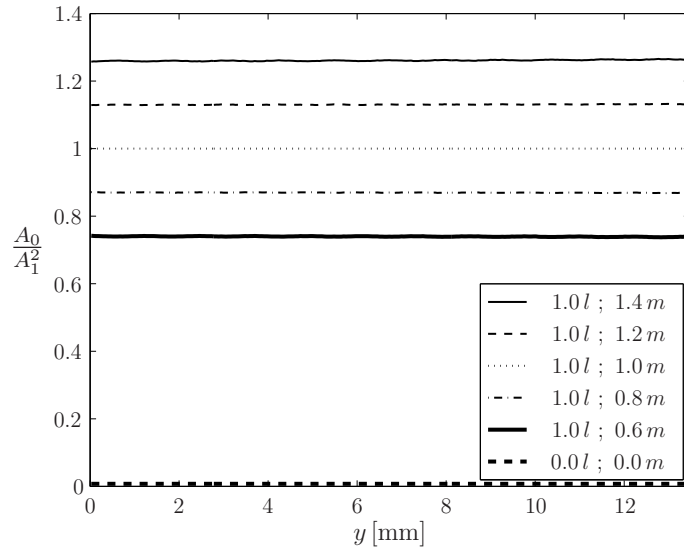


Figure 5.15: Ratio $\frac{A_0}{A_1^2}$ over the propagation distance y for different values of the third-order elastic constants, normalized to the specific ratio obtained for the TOEC of Aluminum D54S.

pressure traction, this will generate a one-dimensional wave field without any dependency on the spatial coordinate x . However, it will be shown that there develops particle motion both in the x - and in the y -directions. The boundary condition applied in this simulation is formulated in terms of Chapter 3 as $Q_1 = 0$ and $Q_2 = Q$. The proceeding will be very similar to the one for the pressure boundary condition. However, since the wave field developing is now due to Q_2 , the ratio $\frac{A_2}{B_1^2}$ will be used to analyze the second-harmonic effect, while the ratio $\frac{A_0}{B_1^2}$ will be applied for the corresponding static effect that arises.

5.1.2.1 Second-Harmonic Effects

In this paragraph, the second-harmonic particle velocity in the direction of wave propagation due to a shear traction at the surface is applied to gain information on the TOEC. Note that there will not arise any fundamental particle velocity term in this direction; this particle motion in the direction of propagation is a purely nonlinear effect.

Here, analytical expressions are derived first from Eqs. (3.83) and (3.84) for the case $Q_1 = 0$. This yields, after some mathematical manipulation,

$$B_1 = \frac{c_t Q_2}{\mu} \quad (5.7)$$

$$A_2 = \frac{c_t |m| Q_2^2}{2 \mu^3 \left[1 - \left(\frac{c_t}{c_1} \right)^2 \right]} \sqrt{\left(\frac{k'}{2} \right)^2 + \sin^2((k_t - k_1) y) [1 - k']} \quad (5.8)$$

$$\frac{A_2}{B_1^2} = \frac{|m|}{2 c_t \mu \left[1 - \left(\frac{c_t}{c_1} \right)^2 \right]} \sqrt{\left(\frac{k'}{2} \right)^2 + \sin^2((k_t - k_1) y) [1 - k']} \quad (5.9)$$

where $k' = \frac{k_t - k_1}{k_t}$. Note that it can also be found that $A_1 = 0$ and $B_2 = 0$. Equation (5.9) shows an important result: the ratio $\frac{A_2}{B_1^2}$ depends only on one TOEC, that is $|m|$. Thus, this scenario provides a direct means of determining changes of one TOEC, while the situation of the pure pressure traction presented in the previous

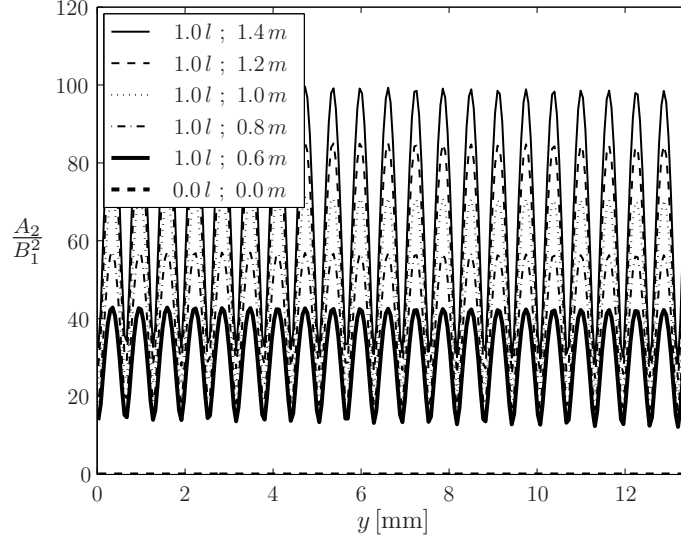


Figure 5.16: Normalized ratio $\frac{A_2}{B_1^2}$ over the propagation distance y for different values of the third-order elastic constants.

subsection offers an opportunity of measuring a change in a combination of both TOEC. However, the spatial dependency is relatively complicated here, but there is one special point that is different from the case of the pure pressure traction – although the ratio $\frac{A_2}{B_1^2}$ oscillates with the propagation distance, it does not “grow” from a more global point of view meaning that it is not cumulative. A characteristic feature of the ratio’s spatial behavior is the distance Δy of one period. It can be derived using the approach

$$(k_t - k_l) \Delta y = \pi$$

$$\Rightarrow \Delta y = \frac{1}{2 f_f \left(\frac{1}{c_t} - \frac{1}{c_l} \right)} \approx 0.63 \text{ mm.} \quad (5.10)$$

Since Eq. (5.9) suggests that the ratio $\frac{A_2}{B_1^2}$ depends only on m , only this TOEC is varied in the simulations at first. Figures 5.16 and 5.17 show the results where the same normalization as usual is applied. There, one can recognize a relatively complicated spatial behavior that is in agreement with Eq. (5.9). The graphs begin at a local minimum and show then a periodic behavior with a period length as predicted by Eq. (5.10). Furthermore, it is recognizable that there is a significant dependency on

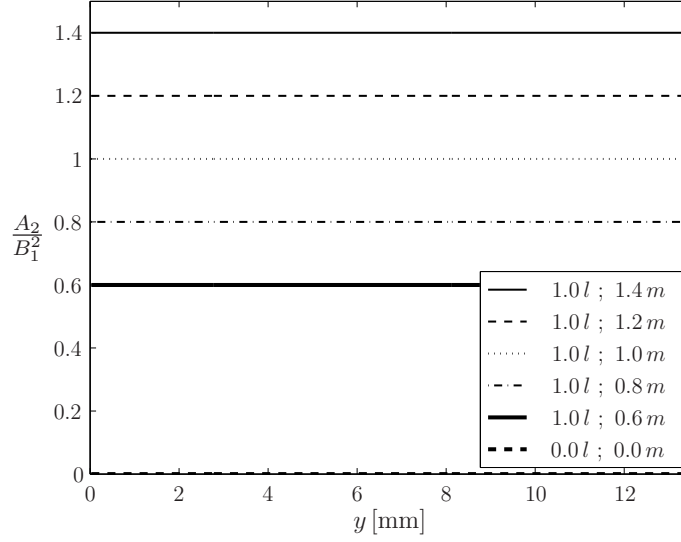


Figure 5.17: Ratio $\frac{A_2}{B_1^2}$ over the propagation distance y for different values of the third-order elastic constants, normalized to the specific ratio obtained for the TOEC of Aluminum D54S.

the value of m which can be seen best in Fig. 5.17. There, the linear dependency of ratio $\frac{A_2}{B_1^2}$ on $|m|$ can be seen because the prefactors which m has been multiplied with appear as scaling factors of the graphs presented.

Now, the influence of the TOEC l on $\frac{A_2}{B_1^2}$ shall be analyzed in the numerical results. Therefore, m is kept constant while l is changed systematically in Figs. 5.18 and 5.19. The outcome is very clear – the graph does not change at all if the material parameter l is varied. This fact confirms what Eq. (5.9) suggests – the ratio $\frac{A_2}{B_1^2}$ is not a function of l . In order to conclude this paragraph, both TOEC are varied in the same fashion in Figs. 5.20 and 5.21. Noting that the outcome is the same as in the case when only m has been varied in Figs. 5.16 and 5.17, one can again see that a variation of l has no influence on the appearance of ratio $\frac{A_2}{B_1^2}$.

5.1.2.2 Static Effects

Now, the static effects appearing in the nonlinear wave field due to a pure shear traction at the surface are inspected. Again, Eqs. (3.83) and (3.84) are used at first

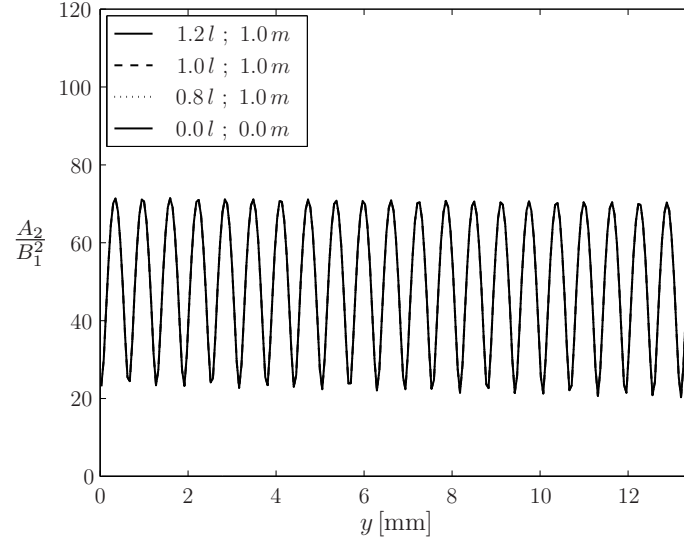


Figure 5.18: Normalized ratio $\frac{A_2}{B_1^2}$ over the propagation distance y for different values of the third-order elastic constants.

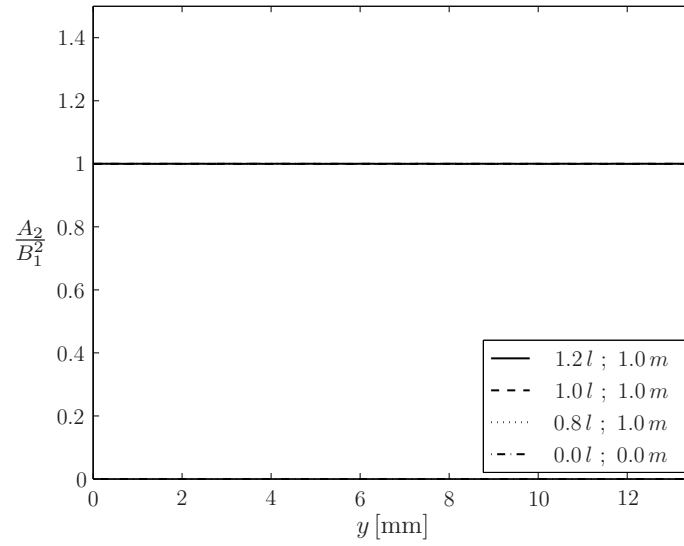


Figure 5.19: Ratio $\frac{A_2}{B_1^2}$ over the propagation distance y for different values of the third-order elastic constants, normalized to the specific ratio obtained for the TOEC of Aluminum D54S.

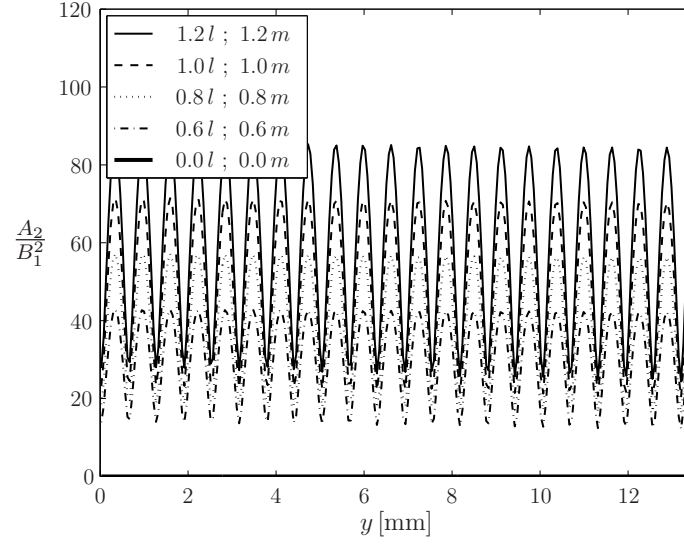


Figure 5.20: Normalized ratio $\frac{A_2}{B_1^2}$ over the propagation distance y for different values of the third-order elastic constants.

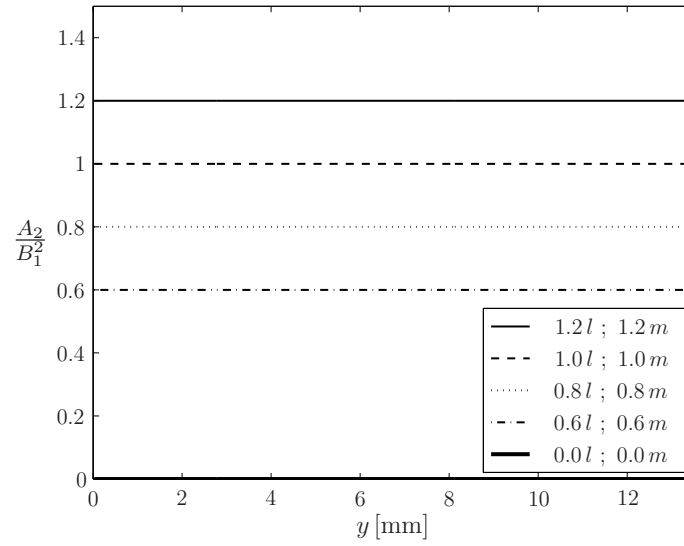


Figure 5.21: Ratio $\frac{A_2}{B_1^2}$ over the propagation distance y for different values of the third-order elastic constants, normalized to the specific ratio obtained for the TOEC of Aluminum D54S.

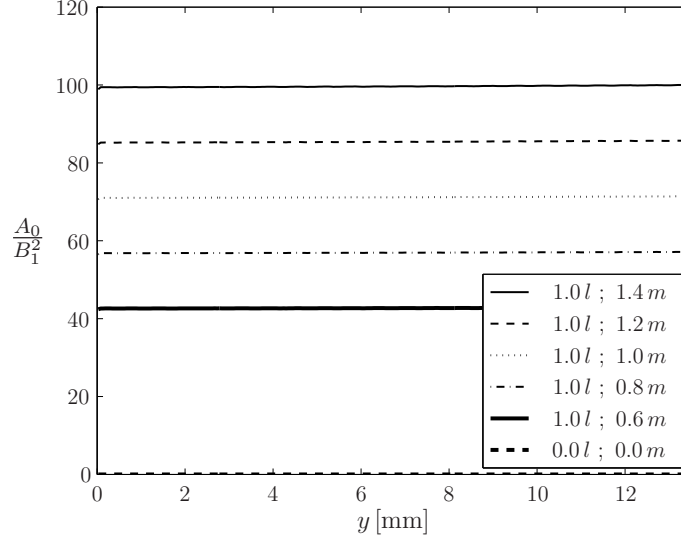


Figure 5.22: Normalized ratio $\frac{A_0}{B_1^2}$ over the propagation distance y for different values of the third-order elastic constants.

to derive analytical expressions for the amplitudes of the harmonics. One can directly find

$$A_0 = \frac{|\gamma|Q_2^2}{4c_1\mu^2} \quad (5.11)$$

$$B_1 = \frac{c_t Q_2}{\mu} \quad (5.12)$$

$$\frac{A_0}{B_1^2} = \frac{|m|}{4c_1\mu}. \quad (5.13)$$

Similar as in the case of a pure pressure traction, the dependency of the static effect on the TOEC is identical to the dependency of the second-harmonic effect on the TOEC. More specifically, the ratio $\frac{A_0}{B_1^2}$ is proportional to $|m|$. However, this ratio has no spatial dependency, exactly as the static effect arising in the case of the pressure boundary condition. The behavior is described can be found in the following figures. Figures 5.22 and 5.23 show the variation of m with a constant l while Figs. 5.24 and 5.25 present the result of changing l with a constant m . All figures show the behavior that has been expected. To conclude this paragraph, equal changes in both TOEC are presented in Figs. 5.26 and 5.27. At the end of this subsection,

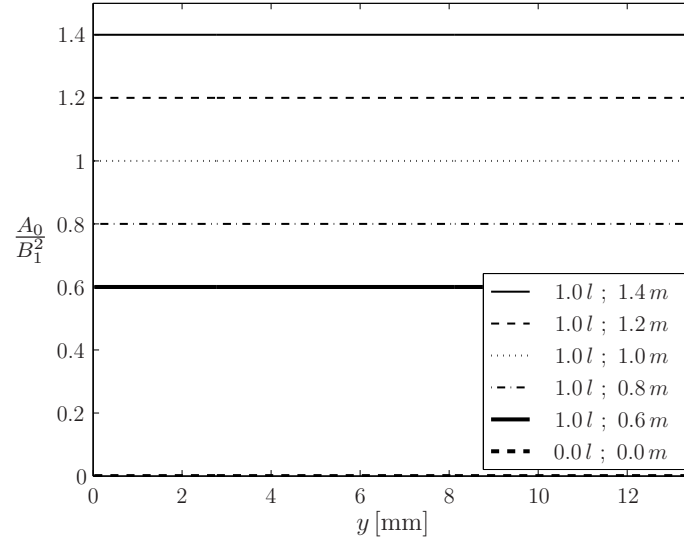


Figure 5.23: Ratio $\frac{A_0}{B_1^2}$ over the propagation distance y for different values of the third-order elastic constants, normalized to the specific ratio obtained for the TOEC of Aluminum D54S.

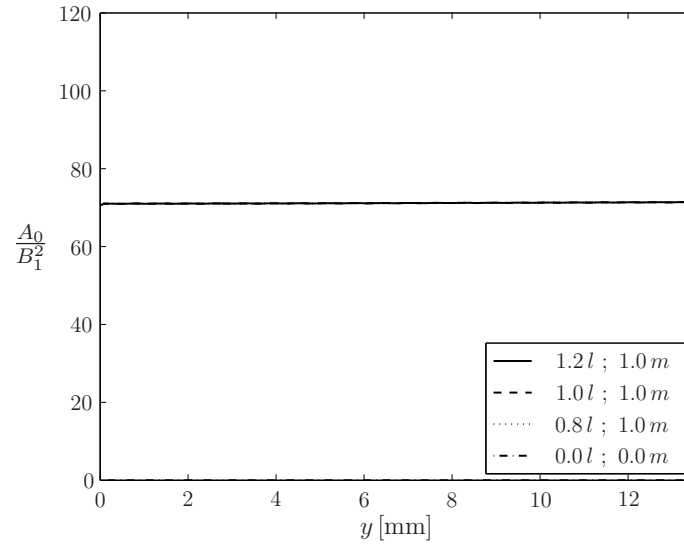


Figure 5.24: Normalized ratio $\frac{A_0}{B_1^2}$ over the propagation distance y for different values of the third-order elastic constants.

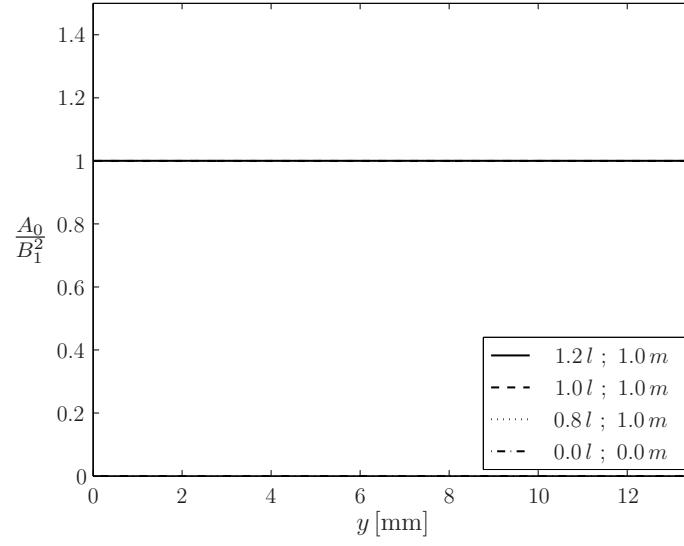


Figure 5.25: Ratio $\frac{A_0}{B_1^2}$ over the propagation distance y for different values of the third-order elastic constants, normalized to the specific ratio obtained for the TOEC of Aluminum D54S.

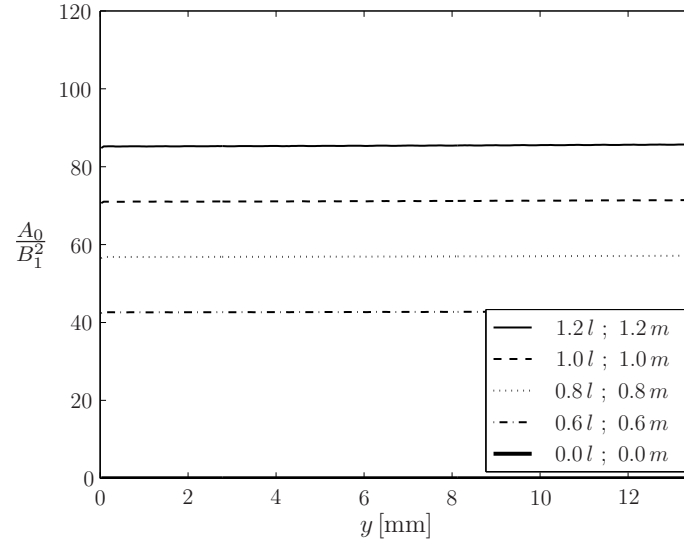


Figure 5.26: Normalized ratio $\frac{A_0}{B_1^2}$ over the propagation distance y for different values of the third-order elastic constants.

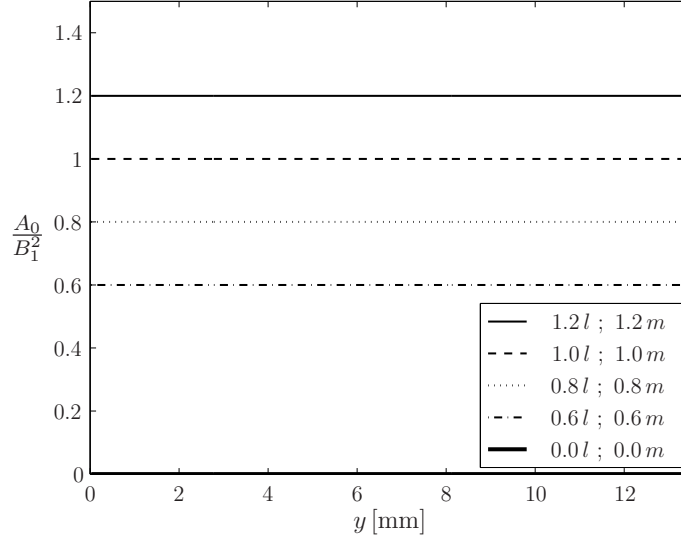


Figure 5.27: Ratio $\frac{A_0}{B_1^2}$ over the propagation distance y for different values of the third-order elastic constants, normalized to the specific ratio obtained for the TOEC of Aluminum D54S.

a conclusion on a possible practical meaning of the second-harmonic and the static effect discussed above shall be provided. Both of them can be used to determine changes in $|m|$ by measuring either A_2 and B_1 or A_0 and B_1 . Again, note that only relative changes can be obtained, no absolute values (as long as an FFT is applied). One possible advantage of using the static effect $\frac{A_0}{B_1^2}$ instead of the second-harmonic effect $\frac{A_2}{B_1^2}$ may be the fact that it does not have a spatial dependency while the second-harmonic effect has a relatively complicated spatial behavior.

5.1.3 Mixed Traction

The last uniform load case considered in this thesis is the more general mixed scenario $Q_1 = Q$ and $Q_2 = Q$. This boundary condition will still generate a one-dimensional wave field but with particle motion both in x - and in y -direction. Note that the nonlinear effects arising in the particle velocity \dot{v} in the direction of wave propagation will be very complex (see Eq. (3.84)). Thus, only nonlinear effects appearing in the particle velocity \dot{u} normal to the direction of propagation are considered

in this subsection.

Since the wave field developing is now due to both Q_1 and Q_2 , the ratios $\frac{B_2}{A_1 B_1}$ and $\frac{B_0}{A_1 B_1}$ are used for the subsequent analysis. Doing so will cancel out the input stress amplitudes Q_1 and Q_2 applied, exactly as for the two load cases already analyzed.

5.1.3.1 Second-Harmonic Effects

Here, the second-harmonic term of the particle velocity along the direction normal to the direction of wave propagation is investigated. Note that this effect only occurs if $Q_1 \neq 0$ and $Q_2 \neq 0$. Again, an analytical expression describing this second-harmonic effect is derived first from Eqs. (3.83) and (3.84). The result is

$$A_1 = \frac{c_1 Q_1}{\lambda + 2\mu} \quad (5.14)$$

$$B_1 = \frac{c_t Q_2}{\mu} \quad (5.15)$$

$$B_2 = \frac{|\gamma| Q_1 Q_2 \omega}{k_1^2 \mu (\lambda + 2\mu) (c_t + 3c_1) (c_1 - c_t)} h(y) \quad (5.16)$$

$$\frac{B_2}{A_1 B_1} = \frac{|m|}{k_t \mu \left(\frac{c_t}{c_1} + 3 \right) (c_1 - c_t)} h(y) \quad (5.17)$$

$$h(y) = \sqrt{(k_t - k_1)^2 + 8 k_t (k_1 + k_t) \sin^2 \left(\frac{k_t - k_1}{2} y \right)}. \quad (5.18)$$

The appearance of Eq. (5.17) is very close to the one of the corresponding term $\frac{A_2}{B_1^2}$ in Eq. (5.9) presented for the previous load case. The dependency on the TOEC is equal – both ratios are proportional to $|m|$ and do not depend on l . Furthermore, the spatial behavior is also a periodic oscillation that is very similar to that of $\frac{A_2}{B_1^2}$ in a qualitative way. Its periodic length can be computed in the same way as it was done above using

$$\begin{aligned} \frac{k_t - k_1}{2} \Delta y &= \pi \\ \Rightarrow \Delta y &= \frac{1}{f_f \left(\frac{1}{c_t} - \frac{1}{c_1} \right)} \approx 1.3 \text{ mm.} \end{aligned} \quad (5.19)$$

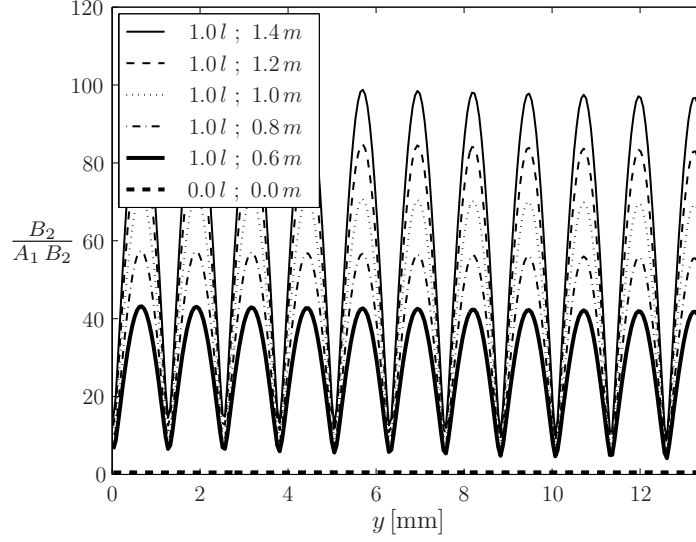


Figure 5.28: Normalized ratio $\frac{B_2}{A_1 B_1}$ over the propagation distance y for different values of the third-order elastic constants.

The results of the simulations are shown in the same order as for the pure shear traction boundary condition since the same dependency on the TOEC is expected here, according to Eq. (5.17). First, one can see in Figs. 5.28 and 5.29 that the graphs are actually proportional to $|m|$ because the prefactor which is used to vary m can be directly recognized as a scaling factor of the ratio $\frac{A_2}{B_1^2}$. Moreover, the spatial behavior suggested by Eq. (5.17) is confirmed; for example, the periodic length is in good agreement with the value given in Eq. (5.19). Figures 5.30 and 5.31 show that there is no dependency on l since the ratio $\frac{B_2}{A_1 B_1}$ is invariant to changes in l . Lastly, Figs. 5.32 and 5.33 conclude this paragraph. The TOEC are changed equally there but the same result as in Figs. 5.28 and 5.29 occurs – again, a clear evidence of the independency on l and a confirmation of the analytical description in Eq. (5.17).

5.1.3.2 Static Effects

The last part needed in order to completely conclude the one-dimensional problems would be the consideration of static effects in the particle velocity \dot{u} generated by the mixed traction applied at the half-space's surface. However, a closer look at

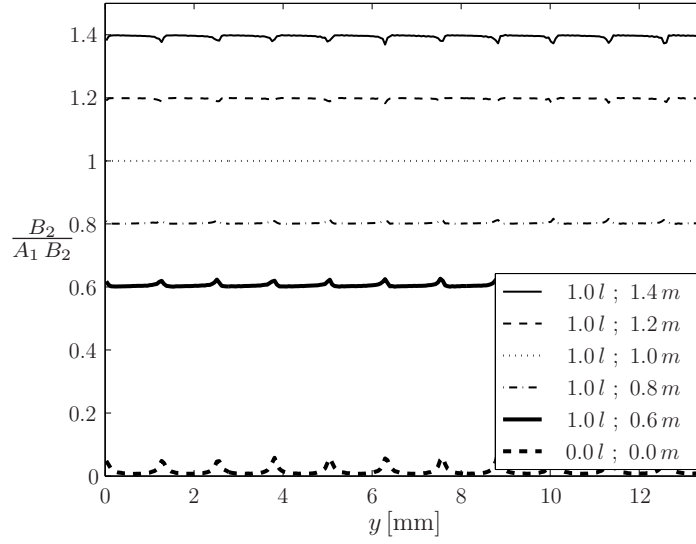


Figure 5.29: Ratio $\frac{B_2}{A_1 B_1}$ over the propagation distance y for different values of the third-order elastic constants, normalized to the specific ratio obtained for the TOEC of Aluminum D54S.

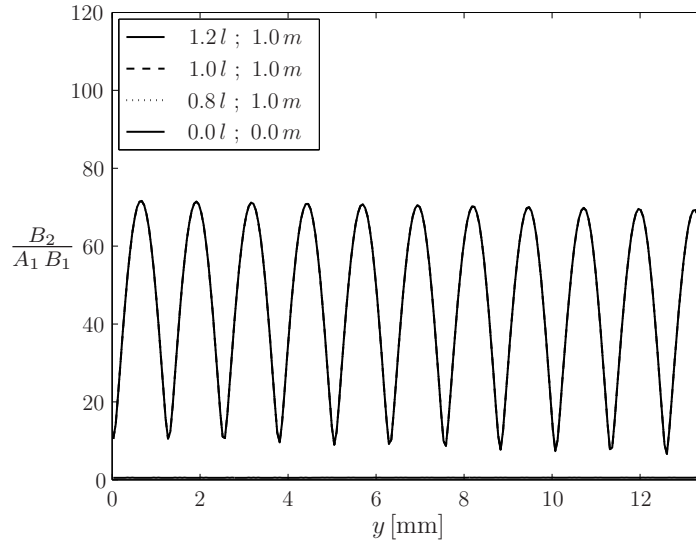


Figure 5.30: Normalized ratio $\frac{B_2}{A_1 B_1}$ over the propagation distance y for different values of the third-order elastic constants.

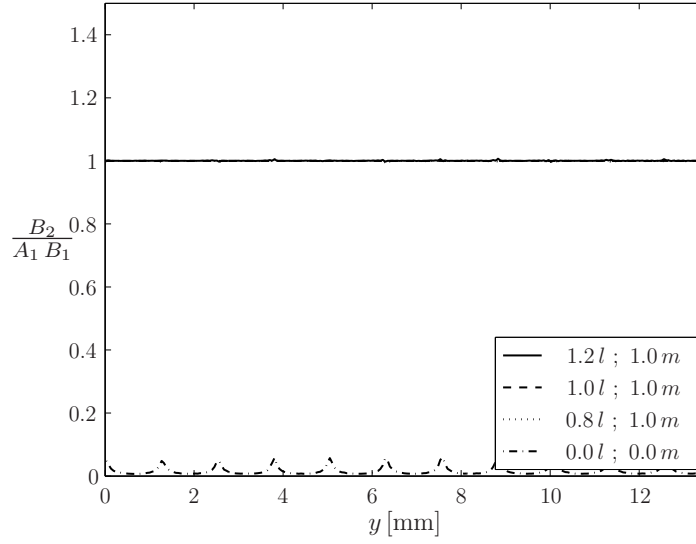


Figure 5.31: Ratio $\frac{B_2}{A_1 B_1}$ over the propagation distance y for different values of the third-order elastic constants, normalized to the specific ratio obtained for the TOEC of Aluminum D54S.

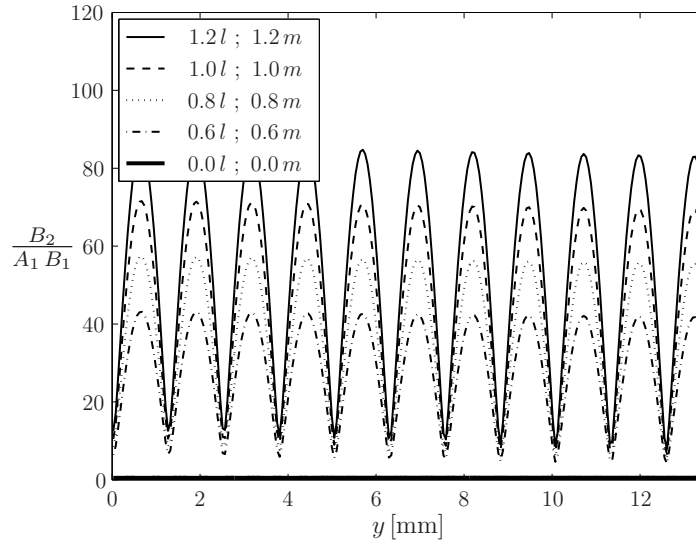


Figure 5.32: Normalized ratio $\frac{B_2}{A_1 B_1}$ over the propagation distance y for different values of the third-order elastic constants.

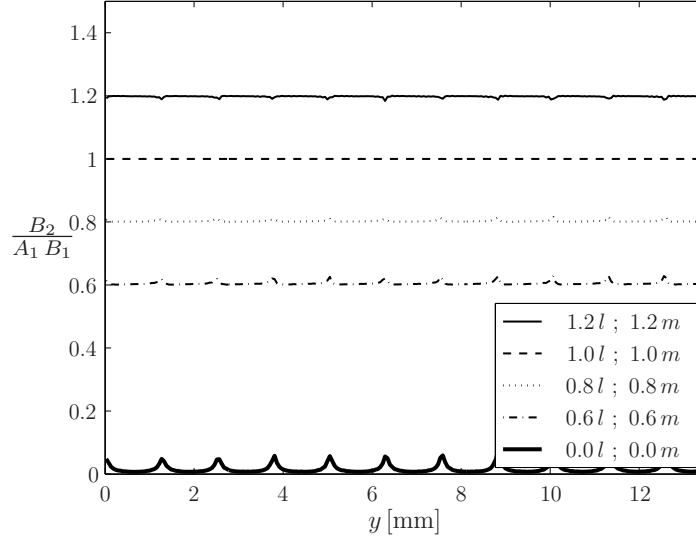


Figure 5.33: Ratio $\frac{B_2}{A_1 B_1}$ over the propagation distance y for different values of the third-order elastic constants, normalized to the specific ratio obtained for the TOEC of Aluminum D54S.

Eq. (3.85) shows that there is no static contribution to the particle velocity in the direction normal to the direction of wave propagation. This is quite obvious because it would not make sense if the material would move statically either in the positive or in the negative x -direction because the boundary condition does not “prefer” one of those. Thus, the absence of a static particle velocity term in \dot{u} can also be justified with the symmetry of the problem. This means that the static effects cannot be used for the determination of the TOEC with the present load case.

Thus, in order to conclude the treatment of the mixed traction boundary condition, a remark is given on how it may be used for the actual determination of a material’s nonlinearity. Clearly, the second-harmonic effects can be used in the same way as the second-harmonic effects of the scenario with the pure shear traction in order to find a change in $|m|$. However, the complicated spatial appearance of the ratio $\frac{B_2}{A_1 B_1}$ may make this methodology difficult. Nevertheless, it is an additional way to determine a change in m .

5.1.4 Conclusion

Three different traction boundary conditions have been applied to the half-space's surface. It was found that a pure pressure load can be used to determine a change in $|l + 2m|$ where one could make use of either the second-harmonic effect or the static effect. Note that the second-harmonic effect has a cumulative nature meaning that the effect increases linearly with propagation distance. This fact may be important if one is interested in a good signal-to-noise ratio. On the other hand, the static effect is independent of the position of the measuring device what would make the determination of the actual position unnecessary. This would become significant if the peak values in the particle velocity could be directly determined from the time signal since then, one could use absolute values in order to compute the absolute value of $|l + 2m|$. The second scenario considered has been the application of a pure shear traction. Here, it was possible to find changes in $|m|$ by making use of either the second-harmonic or the static effect. Their main difference is their spatial dependency on the propagation distance which could be an issue in an actual measurement. Lastly, a mixed traction boundary condition has been applied and the particle velocity \dot{u} has been made use of – in contrast to the two previous load cases where the nonlinear effects in \dot{v} had been analyzed. Here, only the second-harmonic effect is appropriate to measure a change in $|m|$.

Thus, it can be concluded that two different measurements are needed to determine changes in both TOEC – or to find their absolute values, if no FFT is involved in the determination of the different harmonic amplitudes.

At last, a remark on the validity of the analytical expressions derived in Chapter 3 is given. Since it is not possible to find the absolute values of the harmonic amplitudes in this research because of the FFT applied, it is not possible to just compare analytical and numerical results. But one may compare the relative sizes of certain harmonic amplitudes as long as the signal processing needed for their determination

is identical. This is done exemplarily here for the second-harmonic effect and the static effect appearing in the wave field arising due to the pure pressure traction because there, the existence of second-harmonic effects has been confirmed (for other boundary conditions) by previous research [22], [26], [24].

Thus, in order to verify the theory presented, the specific distance y_p where the magnitude of the second-harmonic magnitude which is dependent on the distance of propagation reaches the p -fold value of the static effect's magnitude which is independent on the position considered shall be determined both analytically and from the simulations. The analytical value can easily be obtained by equating the expressions for A_0 and A_2

$$\begin{aligned} A_2 &= p A_0 \\ \Rightarrow y_p &= \frac{1}{k_1} \sqrt{p^2 - \frac{1}{4}}. \end{aligned} \tag{5.20}$$

For $p = 10$, for example, this yields $y_{10} = 1.94 \text{ mm}$. Figure 5.34 shows the two magnitudes over the propagation distance for the original material values of Aluminum D54S. The point of intersection is approximately at $y_{10} = 1.97 \text{ mm}$ which is in good agreement with the analytically computed value. Therefore, this can be considered as an exemplary confirmation of the analytically derived static effect by the corresponding numerically computed static effect.

5.2 Half-Space Subjected to a Uniform Line Load

In this section, a half-space subjected to a harmonic line load which is applied as shown in Fig. 3.4 is analyzed. The half-space is again assumed to be initially at rest. However, not only a pressure line load as depicted in the figure but also a shear load will be investigated – similarly to the previous section. The remaining surface adjacent to the line where the load is applied is always stress-free.

The material of the half-space is again Aluminum D54S whose material parameters

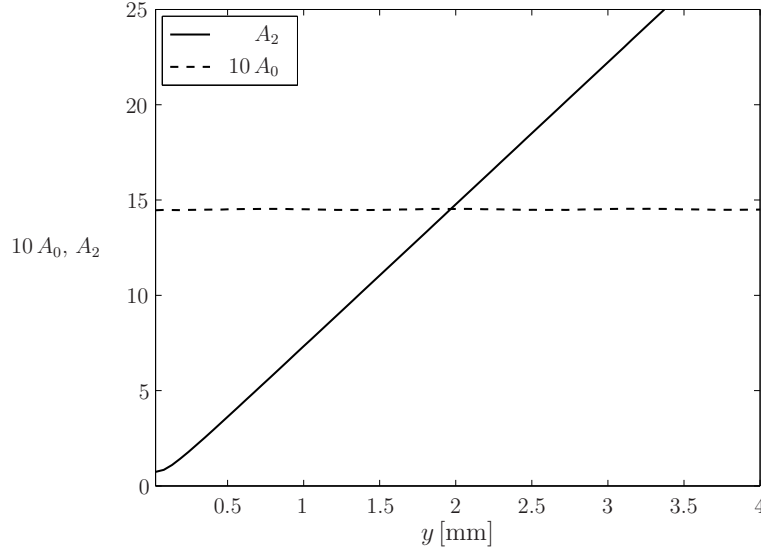


Figure 5.34: Normalized amplitudes A_2 and $10A_0$ over the propagation distance y for the TOEC of Aluminum D54S. The point of intersection is approximately at $y_{10} = 1.97$ mm.

Table 5.3: Simulation parameters used for the two-dimensional problems.

f_f [MHz]	Q [$\frac{N}{mm}$]	Δx [m]	Δy [m]
5.0	10	9.0×10^{-6}	9.0×10^{-6}

have been presented in Table 5.1. Note that the TOEC will be varied systematically again in order to illustrate their impact on the wave field arising. The further parameters used for the following simulations are stated in Table 5.3. The spatial discretization chosen is not as fine as the one for the simulations of the one-dimensional problems in the previous chapter. Clearly, this will result in less reliable data but a higher discretization would have led to unrealizable computational efforts. The reason is that for the line load applied a two-dimensional wave field will arise and thus, a much bigger domain has to be simulated in order to unravel the properties of this wave field. Additionally, a reference line load is introduced in Table 5.3 that will be used to express the pressure load Q_1 and the shear load Q_2 applied in the different

load cases.

The motivation for the analysis of these complex problems is that actual wave fields generated by ultrasonic transducers in experimental measurements are not one-dimensional in general because of the finite size of the transducers. Thus, it is not straightforward to draw conclusions from one-dimensional analytical solutions to these wave fields; instead, the dependency of the two-dimensional wave fields arising on the material's nonlinearity has to be investigated in detail first. However, to the author's best knowledge, such solutions to the nonlinear problem are currently not available so that it is tried to numerically gain information on how the material's nonlinearity influences the appearance of wave propagation in a nonlinear material.

5.2.1 Pure Pressure Traction Line Load

At first, the scenario of a pure pressure line load is investigated which is given by $Q_1 = Q$ and $Q_2 = 0$. An analytical solution to this problem has been presented in Section 3.2 for a linear material. Here, the material is nonlinear but it is expected that the nonlinear effects will be small as they have been in the one-dimensional problems. Therefore, the results obtained from the two-dimensional simulations will be analyzed in the frequency domain in order to quantitatively detect these nonlinear phenomena. However, in order to exemplarily show the agreement of the analytical solution and the numerical results, the particle velocity field simulated is shown in Figs. 5.35 and 5.36 at a fixed time. Note that the components of the particle velocity are described in polar coordinates (see Fig. 3.6) because of the problem's cylindrical nature. All of the wave phenomena predicted by the analytical solution in Fig. 3.11 are recognizable but, as for the one-dimensional problems, additional nonlinear effects cannot be detected. Considering the linear solution given by Eqs. (3.188) and (3.189), one may expect that the wave field arising at the plane of symmetry $x = 0$ has some

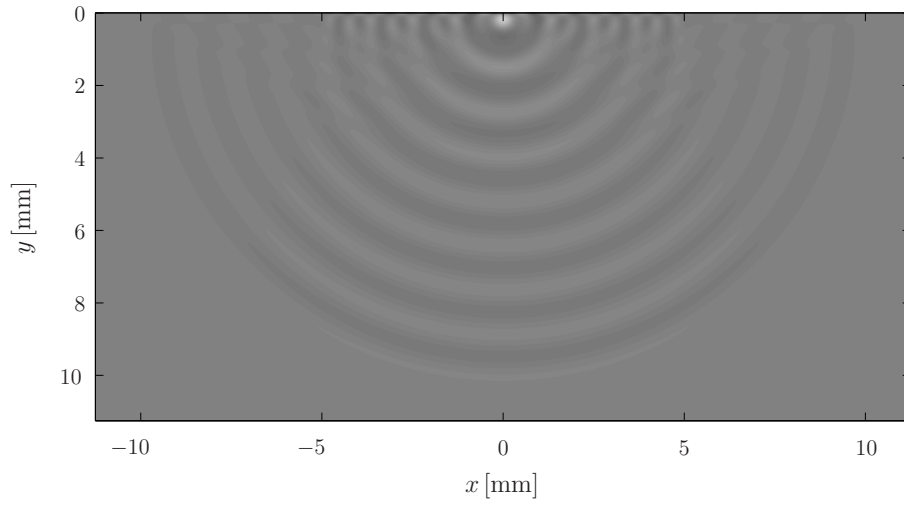


Figure 5.35: Particle velocity field \dot{u}_r over the entire domain at $t = 1.68 \mu s$.

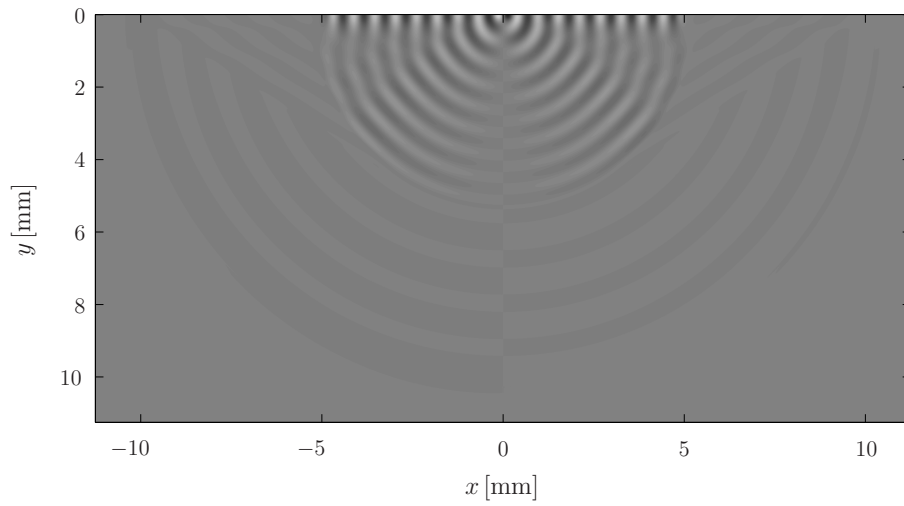


Figure 5.36: Particle velocity field \dot{u}_θ over the entire domain at $t = 1.68 \mu s$.

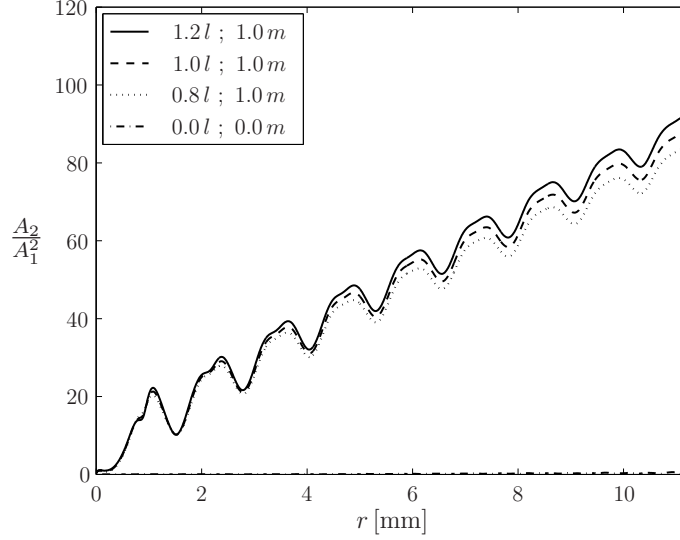


Figure 5.37: Normalized ratio $\frac{A_2}{A_1^2}$ over the propagation distance r at $\theta = 0^\circ$ for different values of the third-order elastic constants.

similarities with a corresponding one-dimensional problem. For example, there, particle motion can only appear in the direction of the excitation. Thus, the nonlinear behavior is analyzed in more detail at the plane of symmetry described by $x = 0$ (or $\theta = 0^\circ$) in the following.

Figures 5.37 and 5.39 present the normalized ratio $\frac{A_2}{A_1^2}$ over the propagation distance where the terms A_1 and A_2 are defined as the amplitudes of the first and the second harmonic of the particle velocity along the direction of wave propagation, just as in the previous section. After the near field in the vicinity of $r = 0$ mm has been left, this second-harmonic effect shows a relatively linear dependency on the propagation distance what means that it actually behaves similar as in the one-dimensional case (compare to Figs. 5.6 and 5.8). Furthermore, it can be recognized that a change in the TOEC m has a more significant influence on the ratio than a change in l what also corresponds to the one-dimensional case where a dependency on the combination $|l + 2m|$ was found. This influence of the TOEC can be seen in more detail in Figs. 5.38 and 5.40.

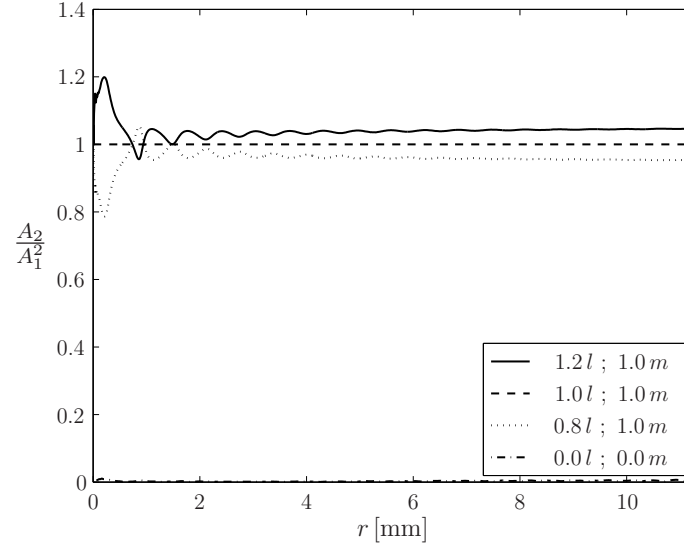


Figure 5.38: Ratio $\frac{A_2}{A_1^2}$ over the propagation distance r at $\theta = 0^\circ$ for different values of the third-order elastic constants, normalized to the specific ratio obtained for the TOEC of Aluminum D54S.

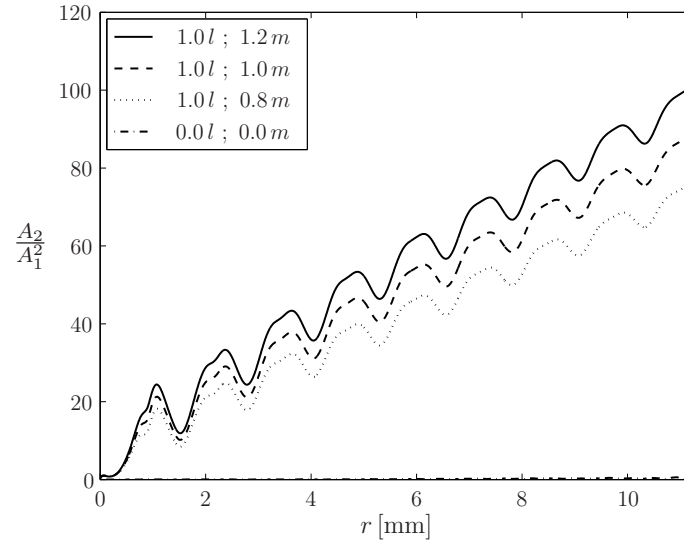


Figure 5.39: Normalized ratio $\frac{A_2}{A_1^2}$ over the propagation distance r at $\theta = 0^\circ$ for different values of the third-order elastic constants.

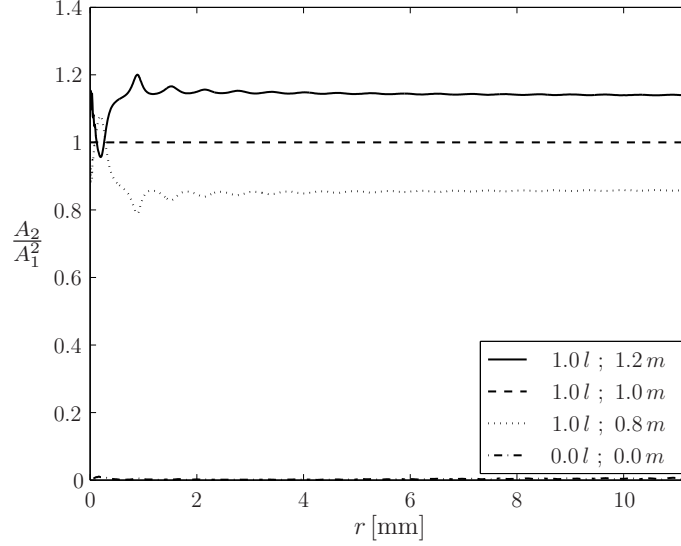


Figure 5.40: Ratio $\frac{A_2}{A_1^2}$ over the propagation distance r at $\theta = 0^\circ$ for different values of the third-order elastic constants, normalized to the specific ratio obtained for the TOEC of Aluminum D54S.

5.2.2 Pure Shear Traction Line Load

In this subsection, a shear traction line load is applied to the half-space's surface which is given by $Q_1 = 0$ and $Q_2 = 0.1 Q$. Again, the evaluation of the data simulated is restricted to the plane of symmetry. Here, both second-harmonic and static effects are analyzed.

5.2.2.1 Second-Harmonic Effects

In order to describe the second-harmonic effect for this load case, the ratio $\frac{A_2}{B_1^2}$ is used again, in analogy to the one-dimensional case. It is shown in Fig. 5.41 for different values of m . Its spatial behavior features the same periodicity as it was found analytically in Eq. (5.10) for the corresponding one-dimensional problem. In Fig. 5.42, the graphs of Fig. 5.41 are related to the graph obtained for the original TOEC of Aluminum D54S. Note that only the local maxima are visualized there because considering values too close to zero would give numerical errors too much weight. The plot shows relatively clearly that ratio $\frac{A_2}{B_1^2}$ is proportional to $|m|$. On the other

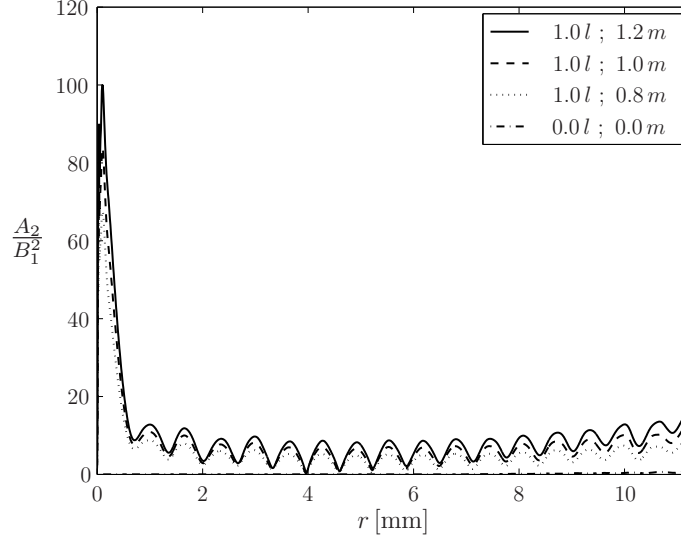


Figure 5.41: Normalized ratio $\frac{A_2}{B_1^2}$ over the propagation distance r at $\theta = 0^\circ$ for different values of the third-order elastic constants.

hand, Figs. 5.43 and 5.44 show that it is independent on the second TOEC l . This dependency on the TOEC is absolutely identical to the corresponding one-dimensional case.

5.2.2.2 Static Effects

Analogously, the ratio $\frac{A_0}{B_1^2}$ is now applied to investigate static effects. In Figs. 5.45 and 5.47, one can recognize that the static effect is not constant over the propagation distance as the static effects in the one-dimensional problems have always been. But Figs. 5.46 and 5.48 show clearly that $\frac{A_0}{B_1^2}$ is proportional to $|m|$ and that it is invariant to changes in l , exactly as in the one-dimensional case.

5.2.3 Conclusion

The investigations have shown that there actually are several similarities between one-dimensional wave fields and two-dimensional wave fields analyzed at their plane of symmetry. On the one hand, the dependency on the propagation distance is partly similar – for the pressure line load, a linear behavior was found while, for the shear

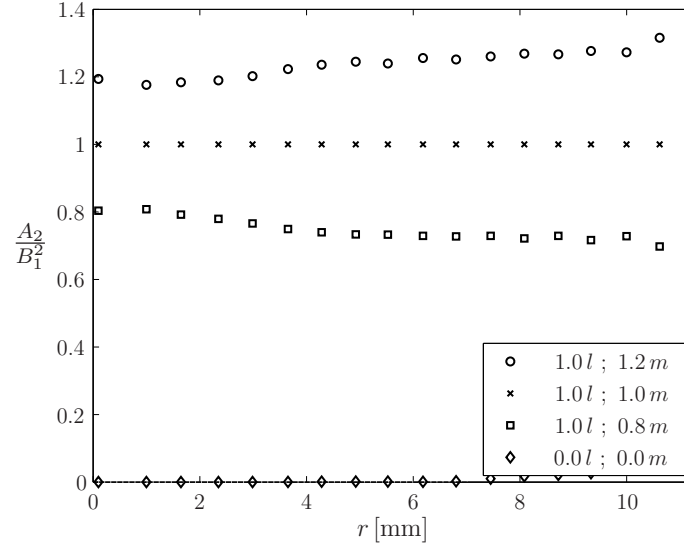


Figure 5.42: Ratio $\frac{A_2}{B_1^2}$ over the propagation distance r at $\theta = 0^\circ$ for different values of the third-order elastic constants, normalized to the specific ratio obtained for the TOEC of Aluminum D54S.

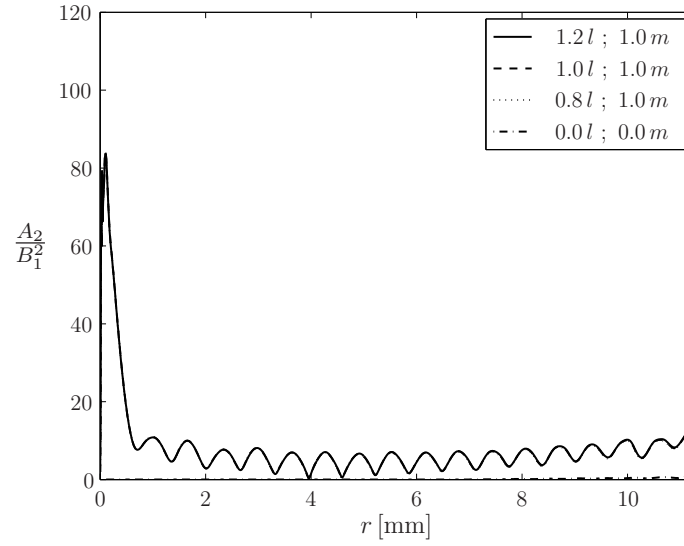


Figure 5.43: Normalized ratio $\frac{A_2}{B_1^2}$ over the propagation distance r at $\theta = 0^\circ$ for different values of the third-order elastic constants.

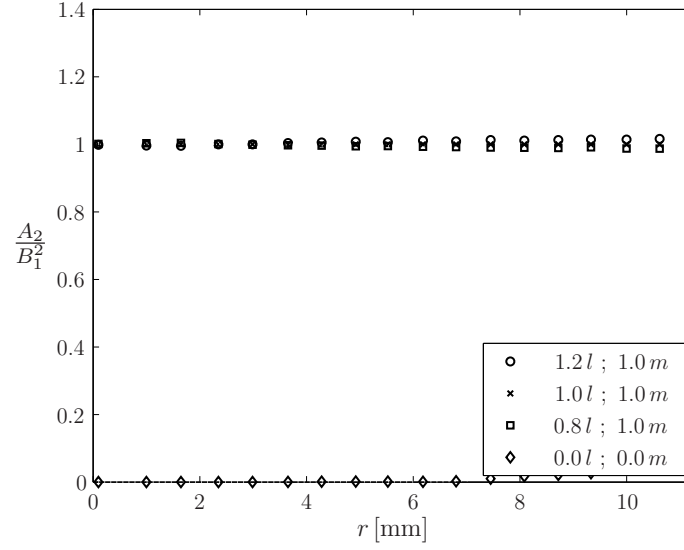


Figure 5.44: Ratio $\frac{A_2}{B_1^2}$ over the propagation distance r at $\theta = 0^\circ$ for different values of the third-order elastic constants, normalized to the specific ratio obtained for the TOEC of Aluminum D54S.

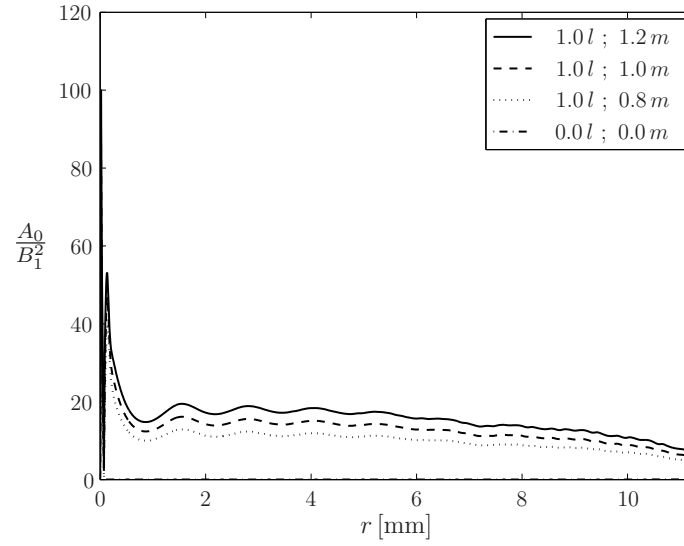


Figure 5.45: Normalized ratio $\frac{A_0}{B_1^2}$ over the propagation distance r at $\theta = 0^\circ$ for different values of the third-order elastic constants.

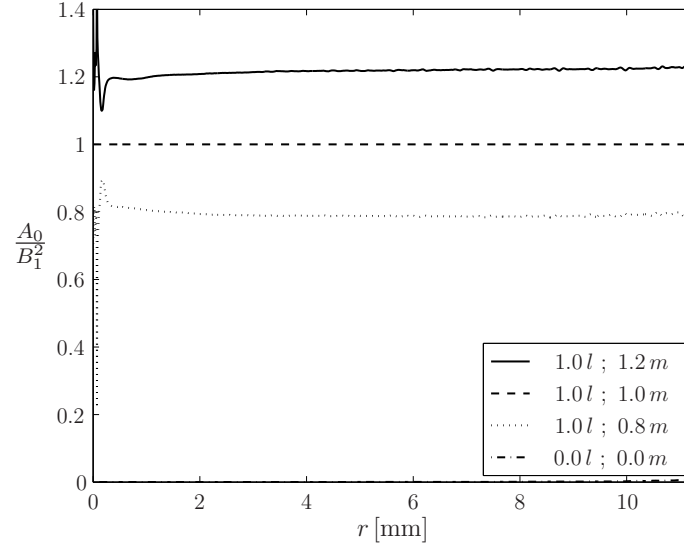


Figure 5.46: Ratio $\frac{A_0}{B_1^2}$ over the propagation distance r at $\theta = 0^\circ$ for different values of the third-order elastic constants, normalized to the specific ratio obtained for the TOEC of Aluminum D54S.

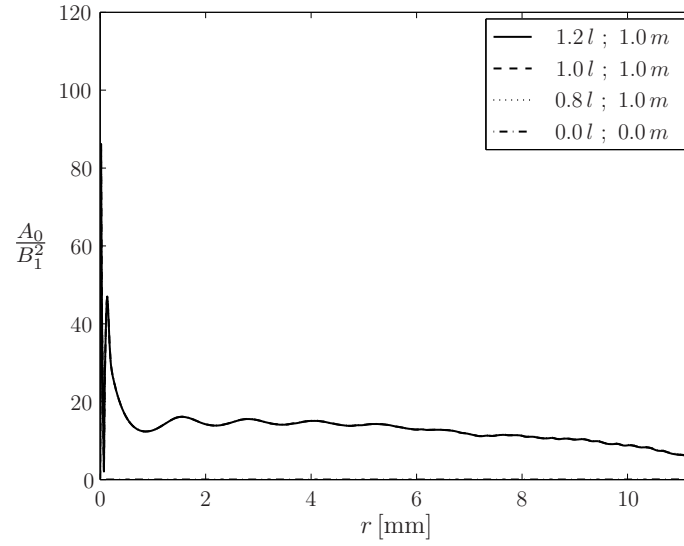


Figure 5.47: Normalized ratio $\frac{A_0}{B_1^2}$ over the propagation distance r at $\theta = 0^\circ$ for different values of the third-order elastic constants.

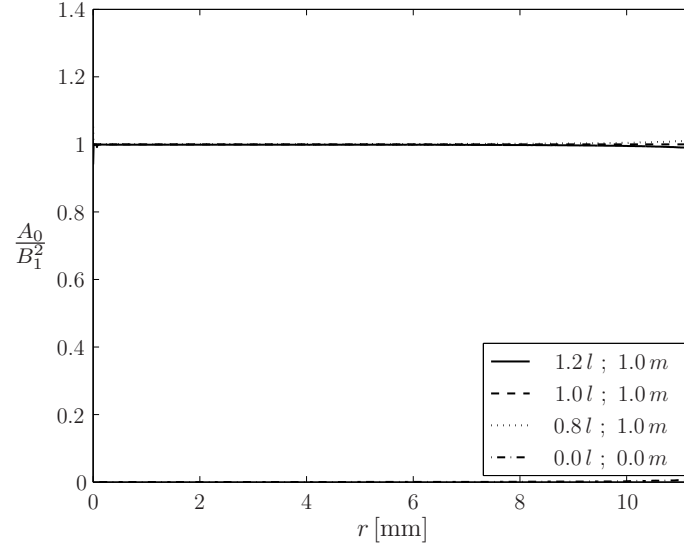


Figure 5.48: Ratio $\frac{A_0}{B_1^2}$ over the propagation distance r at $\theta = 0^\circ$ for different values of the third-order elastic constants, normalized to the specific ratio obtained for the TOEC of Aluminum D54S.

line load, the same periodicity appeared in the graph as in the one for the one-dimensional wave field due to a uniform shear load. However, the more important point is probably the dependency on the TOEC. At the plane of symmetry, all of the two-dimensional problems examined above feature the same dependency on the TOEC as the corresponding one-dimensional problems. This knowledge may allow the determination of changes in the TOEC if measurements are performed at a fixed position at the symmetry plane since changes in the particle velocity field arising can then be directly related to changes in the TOEC.

However, it has also to be mentioned that the quality of the results is not as good here as in Section 5.1 what is due to the worse discretization.

5.3 *Simulation of a Finite-Size Transducer*

The goal of this section is to investigate how the wave field generated by a real transducer with finite dimensions differs from the one that arises due to the line load that was applied in the previous section. Therefore, the spatial traction distribution that

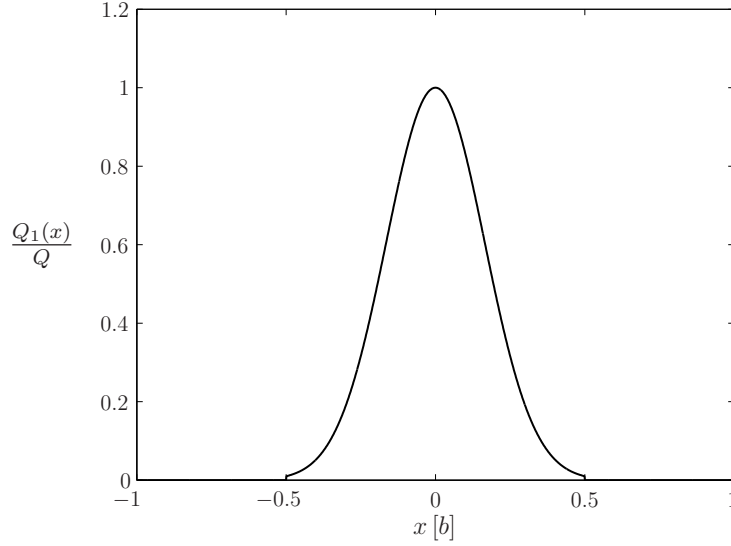


Figure 5.49: Spatial distribution of the pressure traction Q_1 applied at the half-space's surface which is used to model a transducer with length b .

a real transducer applies at the surface of a component is tried to be modeled in the following. Therefore, again a half-space is considered that is subjected to a boundary condition that is a function of the coordinate x (see Fig. 3.4, for example). Note that, since only two-dimensional problems in plane strain can be simulated with the available simulation code, it is not possible to model a circular transducer. Instead, a transducer with one finite length b in x -direction is considered. Implicitly, the boundary condition can only be constant in z -direction so that the model actually represents a transducer with a rectangular surface whose one dimension is large compared to the other one with length b .

The spatial distribution of the transducer model is based on a Gaussian function; in Fig. 5.49, the pressure amplitude applied is shown in dependency on the spatial coordinate x in terms of the reference stress amplitude Q . Note that the Gaussian was cut on both sides at positions where its value went below a limit of one percent of its maximum value.

In order to analyze the influence of this transducer shape in comparison to the line

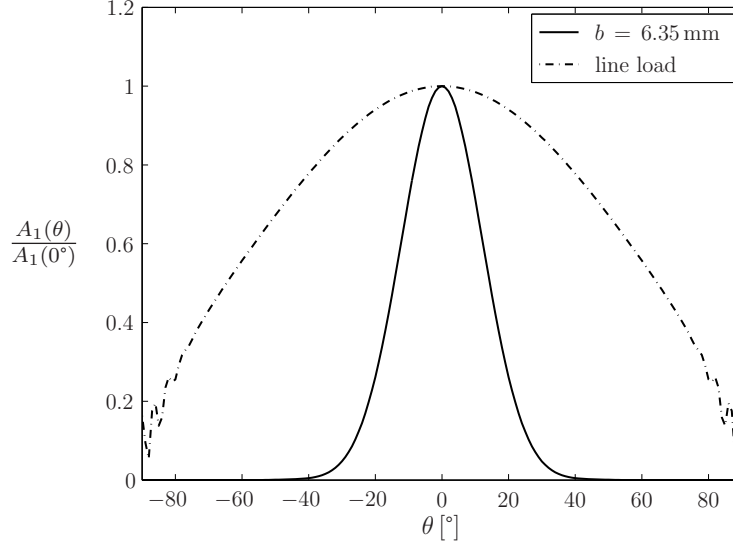


Figure 5.50: Directivity pattern at a propagation distance $r_0 = 1.6b$ obtained for the transducer model and for a line load, expressed by the ratio $\frac{A_1(\theta)}{A_1(0^\circ)}$ over the angle θ .

load, a linear material is chosen in order to separate the influence of the new shape from the one of the nonlinearity. Thus, it is $l = m = 0$ while all other material parameters are the same as in Table 5.3. The simulation parameters used here are the same as used for the previous two-dimensional problems and are presented in Table 5.3.

Figure 5.50 shows the appearance of the directivity pattern arising. There, the normalized fundamental amplitude A_1 of the particle velocity \dot{u}_r in radial direction is plotted over the angle θ at a fixed distance r_0 . The amplitude is normalized to its maximum value occurring at $\theta = 0^\circ$. Additionally, the directivity pattern that appears for the corresponding simulation with a line load is shown. Figure 5.51 presents the same data in a semi-logarithmic scale.

It is clearly recognizable that the transducer model generates a more directive wave field than the line load meaning that a main lobe occurs at $\theta = 0^\circ$. For angles $|\theta| > 30^\circ$, the transducer does not generate a particle motion in radial direction while the line load does so at every angle θ of the range considered.

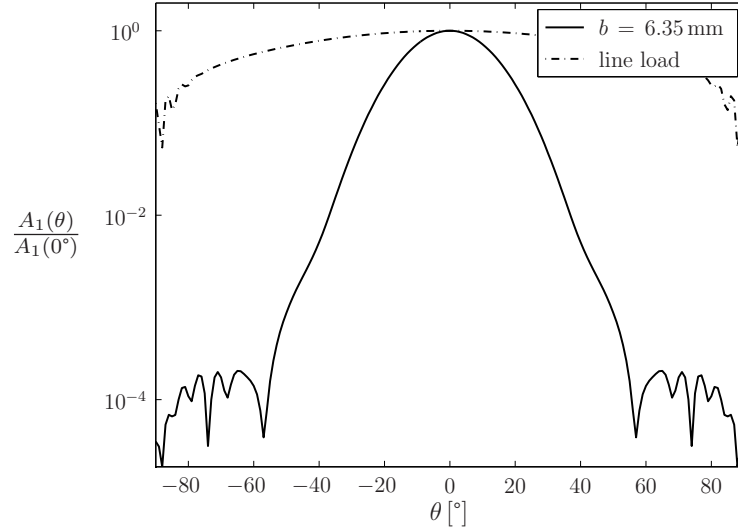


Figure 5.51: Directivity pattern of Fig. 5.50 expressed in a semi-logarithmic scale.

5.3.1 Conclusion

The simulations confirm that the finite size of real transducers has a significant influence on the appearance of the wave field developing. Therefore, this fact has to be kept in mind if experimental data are compared to analytical two-dimensional solutions as, for example, provided in Section 3.2. The results indicate that the measuring device in an experiment should be located at or close to the plane of symmetry described by $\theta = 0^\circ$ in order to achieve an ideal signal-to-ratio, for example. Note that this circumstance also justifies the more detailed analysis of the two-dimensional wave fields presented in Section 5.2 at their plane of symmetry.

5.4 *Simulation of Reflection Effects*

In this section, reflection effects in a nonlinear material are simulated and compared to the analytical expressions derived in Section 3.3. The material analyzed is again Aluminum D54S whose material parameters are provided in Table 5.1. The simulation parameters used for the subsequent simulations are stated in Table 5.4. The goal of this section is the investigation of how the nonlinear effects behave after reflections at

Table 5.4: Simulation parameters used for the reflection problems.

f_f [MHz]	Q [$\frac{\text{N}}{\text{mm}^2}$]	Δx [m]	Δy [m]	Δt [μs]	L [mm]
5.0	2.22	4.5×10^{-6}	4.5×10^{-6}	1.0	24.75

different boundaries. The main difference between the simulations presented here and those of the previous sections is the geometry considered. Here, a plate with infinite side lengths but a finite thickness L (in the y -direction) is investigated. This means that the simulation domain has now two physical and two numerical boundaries as shown in Fig. 4.2. Initially, the plate is at rest but another difference from former simulations is the fact that the time in which the harmonic input signal is applied is now limited to the duration Δt . This means that a wave with finite length will travel through the plate. The wave will be excited by a pure pressure traction $Q_1 = 0.1 Q$ that is applied at one side of the plate. It will travel through the plate, be reflected at the boundary at $y = L$, travel back, be reflected again at $y = 0$, and so on. For the reflections, the boundaries are considered as either stress-free or rigidly clamped. Three different scenarios are investigated in the following. Note that – similar to the problem in Subsection 5.1.1 – a one-dimensional wave field with particle motion only in the direction of wave propagation (y -direction) will arise.

5.4.1 Plate with Two Stress-Free Sides

In this subsection, both of the physical boundaries are modeled to be stress-free (of course, except for the time when the pressure traction is applied at one side). The focus is again on the nonlinear effects so that an appropriate signal processing is applied to determine the harmonic amplitudes A_1 , A_2 and A_0 in dependency on the position in the plate. As in Subsection 5.1.1, the ratio $\frac{A_2}{A_1^2}$ is used to analyze the second-harmonic effect while the ratio $\frac{A_0}{A_1^2}$ is applied to describe the static effect.

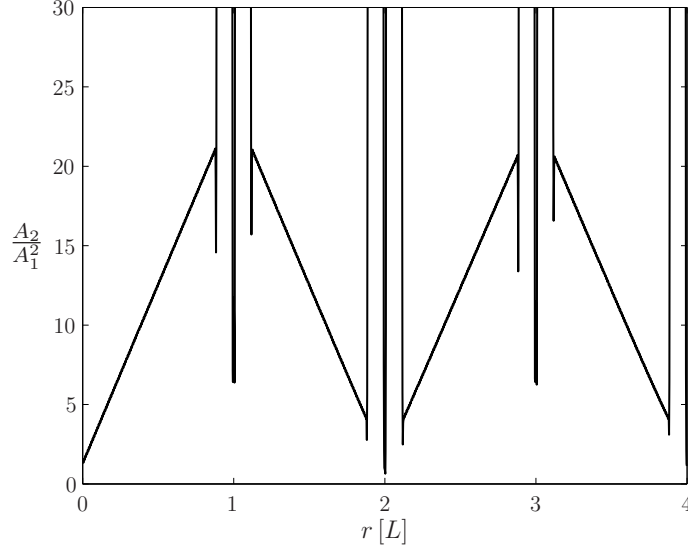


Figure 5.52: Normalized ratio $\frac{A_2}{A_1^2}$ over the accumulated propagation distance r which is expressed in multiples of the plate's thickness L . Both sides of the plate are stress-free.

In the subsequent simulations, the duration of the simulation is chosen in such a way that the wave travels through the plate twice in positive y -direction and twice in negative y -direction. The results are shown in Figs. 5.52 and 5.53. Note that the spatial dependency is not expressed in terms of the coordinate y but in terms of the accumulated propagation distance r . In Fig. 5.52, one can recognize that the ratio $\frac{A_2}{A_1^2}$ behaves as usual as long as the wave travels towards the opposite boundary. However, after the reflection, it shows a linear decreasing what means that the term A_2 is not proportional to the accumulated distance of propagation r as one could have expected. When the wave arrives again at $y = 0$ and is reflected there, the ratio $\frac{A_2}{A_1^2}$ starts increasing linearly again, and the action is repeated exactly as in the first cycle. Note that the signal processing that has been applied is not capable of handling situations where an incident and a reflected wave interfere. Unfortunately, this results in the peaks occurring around the positions where the wave is reflected.

At this point, the behavior at $y = L$ is explained exemplarily with the analytical expressions for a reflected wave presented in Section 3.3. From Eq. (3.227) that

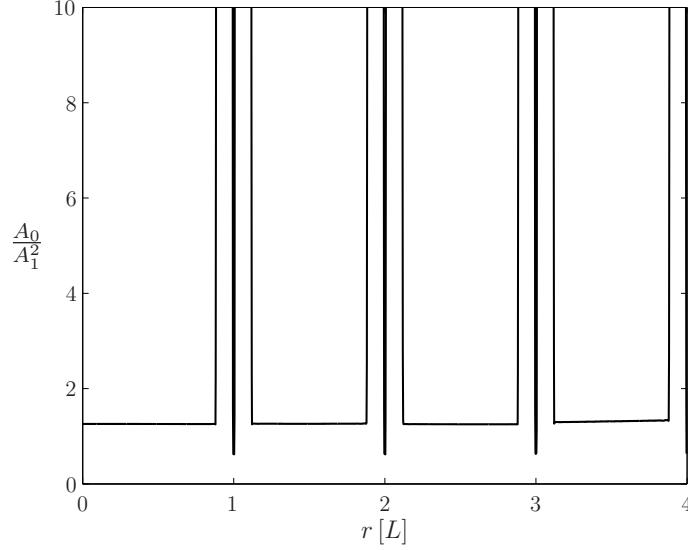


Figure 5.53: Normalized ratio $\frac{A_0}{A_1^2}$ over the accumulated propagation distance r which is expressed in multiples of the plate's thickness L . Both sides of the plate are stress-free.

describes the particle velocity field $\dot{v}^{(r)}$ of a wave reflected at a stress-free boundary, one can derive the expressions for the harmonic amplitudes as

$$A_1 = \frac{c_1 Q_1}{\lambda + 2\mu} \quad (5.21)$$

$$A_0 = \frac{|l + 2m| Q_1^2}{2 \rho c_1 (\lambda + 2\mu)^2} \quad (5.22)$$

$$A_2 = \frac{\omega |l + 2m| Q_1^2}{2 (\lambda + 2\mu)^3} \sqrt{y^2 + \frac{1}{4 k_1^2}} \quad (5.23)$$

$$\frac{A_0}{A_1^2} = \frac{|l + 2m|}{2 c_1 (\lambda + 2\mu)} \quad (5.24)$$

$$\frac{A_2}{A_1^2} = \frac{\omega |l + 2m|}{2 (\lambda + 2\mu) c_1^2} \sqrt{y^2 + \frac{1}{4 k_1^2}}. \quad (5.25)$$

Remember that the reflected wave travels in negative y -direction from $y = L$ back to $y = 0$. Therefore, Eq. (5.25) explains the decreasing nature of the ratio $\frac{A_2}{A_1^2}$ in Fig. 5.52 between $r = L$ and $r = 2L$. Further reflections can be easily explained in an absolutely analogous way. It can be concluded that the second-harmonic effect always changes the sign of its slope when it is reflected at a stress-free boundary.

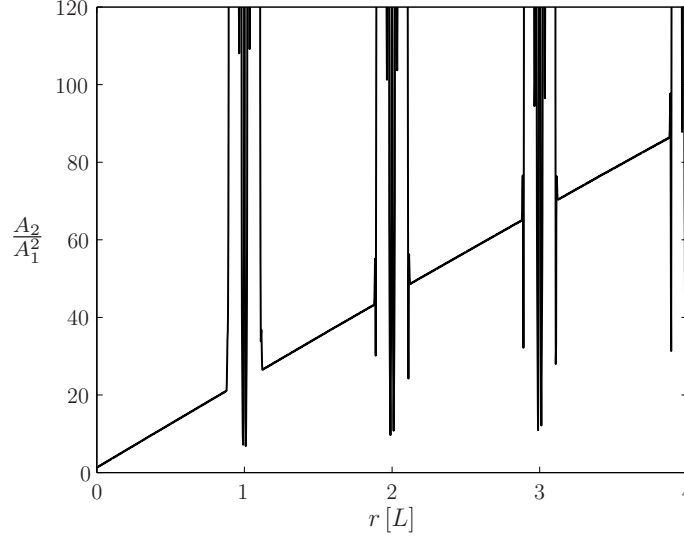


Figure 5.54: Normalized ratio $\frac{A_2}{A_1^2}$ over the accumulated propagation distance r which is expressed in multiples of the plate's thickness L . Both sides of the plate are rigidly clamped.

Accordingly, Eq. (5.24) shows that the ratio $\frac{A_0}{A_1^2}$ for the reflected wave is a constant with the same value as the incident wave had before its reflection (see Eq. (5.6)).

5.4.2 Plate with Two Rigidly Clamped Sides

The next scenario considered here includes two rigidly clamped boundaries. Clearly, this is a more theoretical investigation because it may be hard to realize a wave due to a pressure traction at one side that turns to a rigid boundary during the time when the wave travels through the plate and back. However, it may be realized with a more complex experimental setup and its realization is not critical within a simulation.

The results are shown in Figs. 5.54 and 5.55. Figure 5.54 reveals a different behavior of ratio $\frac{A_2}{A_1^2}$ after the reflection at the rigid boundary compared to Figure 5.52. Now, it keeps on increasing linearly after every reflection at a rigid boundary. Again, this behavior can be explained if the analytical expression (3.220) for the particle velocity field arising in the reflected wave is used to determine expressions for the harmonic

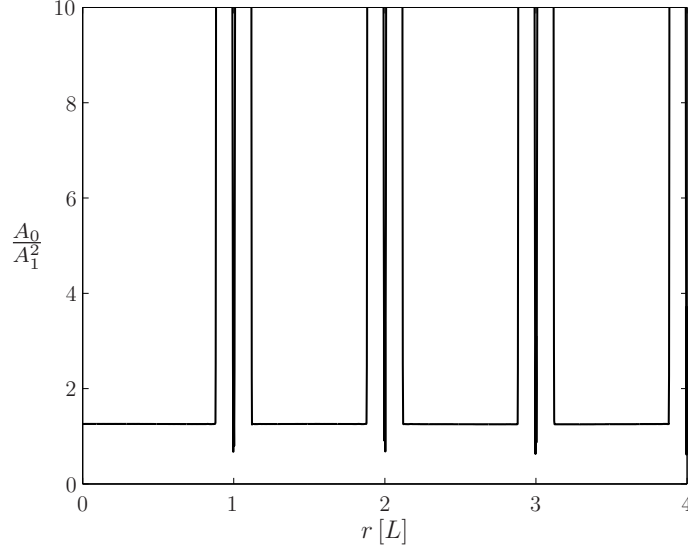


Figure 5.55: Normalized ratio $\frac{A_0}{A_1^2}$ over the accumulated propagation distance r which is expressed in multiples of the plate's thickness L . Both sides of the plate are rigidly clamped.

amplitudes

$$A_1 = \frac{c_1 Q_1}{\lambda + 2\mu} \quad (5.26)$$

$$A_0 = \frac{|l + 2m| Q_1^2}{2 \rho c_1 (\lambda + 2\mu)^2} \quad (5.27)$$

$$A_2 = \frac{\omega |l + 2m| Q_1^2}{2 (\lambda + 2\mu)^3} \sqrt{(2L - y)^2 + \frac{1}{4 k_1^2}} \quad (5.28)$$

$$\frac{A_0}{A_1^2} = \frac{|l + 2m|}{2 c_1 (\lambda + 2\mu)} \quad (5.29)$$

$$\frac{A_2}{A_1^2} = \frac{\omega |l + 2m|}{2 (\lambda + 2\mu) c_1^2} \sqrt{(2L - y)^2 + \frac{1}{4 k_1^2}}. \quad (5.30)$$

Equation (5.30) explains the behavior of $\frac{A_2}{A_1^2}$ between $r = L$ and $r = 2L$. Since the wave travels from $y = L$ to $y = 0$, ratio $\frac{A_2}{A_1^2}$ grows with increasing r in the range considered. The same behavior is recognized at the other reflections in Fig. 5.54. Thus, one can conclude that the second-harmonic effect keeps the sign of its slope if it is reflected at a rigid boundary what is in contrast to its behavior at a stress-free boundary.

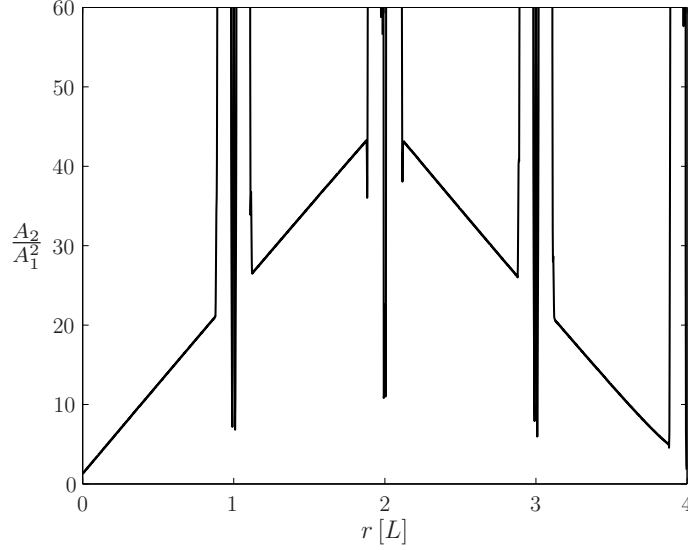


Figure 5.56: Normalized ratio $\frac{A_2}{A_1^2}$ over the accumulated propagation distance r which is expressed in multiples of the plate's thickness L .

Furthermore, Eq. (5.29) shows that the ratio $\frac{A_0}{A_1^2}$ is not changed in any way if the wave is reflected at a rigid boundary. It remains constant, exactly as for the stress-free boundary in Subsection 5.4.1.

5.4.3 Plate with One Stress-Free and One Rigidly Clamped Side

This last scenario applies a stress-free boundary at $y = 0$ and a rigid boundary at $y = L$. The numerical results are shown in Figs. 5.56 and 5.57. Figure 5.56 confirms the conclusions that were found from the previous scenarios. It shows that the ratio $\frac{A_2}{A_1^2}$ keeps increasing at $r = L$ where a rigid boundary is hit by the wave. In other words, it maintains the sign of its slope there. At $r = 2L$, a stress-free boundary is reached, and the second-harmonic effect changes the sign of its slope. Finally, at $r = 3L$, the wave reaches the rigid boundary again, and keeps the negative sign of its slope.

Ratio $\frac{A_0}{A_1^2}$ in Fig. 5.57 shows also the behavior expected – it is invariant to reflections at both rigid and stress-free boundaries.

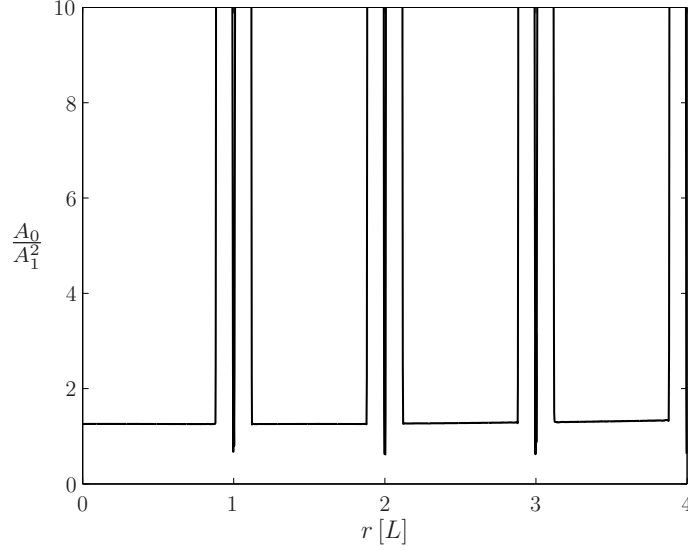


Figure 5.57: Normalized ratio $\frac{A_0}{A_1^2}$ over the accumulated propagation distance r which is expressed in multiples of the plate's thickness L . The side of the transducer is stress-free, the opposite side is rigidly clamped.

5.4.4 Conclusion

The simulations have shown how the second-harmonic and the static effect behave if the wave is reflected at either stress-free or rigid boundaries. The results agree with the analytical solutions to the reflected waves derived in Section 3.3. It shall be pointed out that these reflection effects may be used in experiments in order to increase the signals to be measured because the typically small nonlinear effects may be hard to detect in a quantitative sense. Thus, one could think of an experimental setup that enables multiple reflections at rigidly clamped boundaries so that the signal-to-noise ratio of the measurement is improved. On the other hand, it has to be kept in mind that reflections at stress-free boundaries are inappropriate to enhance the signal strength of the second-harmonic effect. Lastly, it was shown that the static effect is not influenced by reflections and that its signal-to-noise ratio cannot be improved with this methodology.

CHAPTER VI

CONCLUSION AND OUTLOOK

This research provides some basic insights into certain effects of nonlinear wave propagation and illustrates how these effects can be used to determine the nonlinearity present in a certain material.

One-dimensional wave propagation in an elastic half-space was considered first. This problem has been analyzed analytically and experimentally by many researchers in the past because it provides a convenient opportunity to measure changes in a material's nonlinearity. More specifically, the second-harmonic amplitude of the particle displacement or the particle velocity field can be measured and used to compute a nonlinearity parameter which is a specific function of the TOEC. However, it should be noted that there is a considerable disadvantage in the application of this method because the determination of the second-harmonic amplitude usually includes the usage of an FFT algorithm which is applied to the time signal measured. Thus, the absolute values cannot be determined – only relative changes can be monitored.

The analytical derivations of [22] or [24] present a boundary condition formulated in terms of the particle displacement prescribed at the half-space's surface; in contrast, this research considers a traction boundary condition at the surface. The reason for this approach is that real transducers in an actual measurement prescribe the stress at the surface instead of the displacement or velocity. Therefore, it is expected that the results obtained for the traction boundary condition of this research will be a better approximation of actual experimental results. It is found that the analytical approximate solution to the traction boundary condition problem in terms of the particle velocity has some significant differences from those presented in both [22]

and [24]. While the behavior of the second-harmonic terms are relatively similar in a qualitative way, it can be seen that a static term appears in the particle velocity field. It is like the second-harmonic effect proportional to a combination of the TOEC. Experimental measurements in the past have shown the actual existence of such static effects [25], [9], [20]. Furthermore, in [7], an analytical derivation explaining such effects is provided. However, both the derivation which is based on a displacement boundary condition and the results are different from those presented in this thesis. The investigation of static effects is also interesting because it may provide an additional means of measuring a material's nonlinearity, and can be used to verify the results found from the second-harmonic amplitude results. Since the static effect described in this research is a constant term in the particle velocity field, it may be possible to find a procedure to determine this static nonlinearity term without the application of an FFT. Then, the disadvantage of the FFT described above would be eliminated. Such a procedure, which is relatively simple has been presented in [20]. At this point, it should be mentioned that the TOEC (or changes in the TOEC) cannot be determined individually from one measurement. Therefore, at least two measurements are necessary in order to measure the values for the two TOEC which are involved in the problems considered in this research. The third TOEC does not appear here because it only plays a role if three-dimensional problems or two-dimensional problems in plane-stress are analyzed. For the first measurement of these TOEC, a pure pressure boundary condition can be applied, while a shear or a mixed traction may be used for the second measurement.

The results predicted by the analytical solution can be confirmed with the results of the simulations. It is shown in detail how the second-order and the static effects change, if the TOEC are varied for the three different traction boundary conditions mentioned above.

The next step of this research is the investigation of two-dimensional problems. Here,

no analytical solutions are available but an attempt was made to find similarities with the one-dimensional problems. Thus, the wave field arising at the plane of symmetry has been analyzed, because it is expected that its appearance there would be closest to the one-dimensional problems. It was shown that both second-order and static terms in the particle velocity develop there, too. Furthermore, although the spatial dependency of the wave field is completely different from the one-dimensional case, it could be recognized that the dependency on the TOEC is very similar. This means that the TOEC can basically be measured with a similar procedure as in the one-dimensional case, as long as the position of the measuring device is opposite to the emitting transducer. However, the numerical results obtained are not as clear as there. This is due to the fact that the discretization used was not as fine as that possible for the one-dimensional problems because the same discretization would have led to calculation times that would have exceeded the frame of time set for this research by far.

A further aspect treated in this thesis is the influence of a transducer's finite size on the wave field developing. As expected, it is shown that a specific directivity pattern occurs with a main lobe at the plane of symmetry. This behavior suggests that, in an experiment, the measuring device applied should be placed there in order to achieve a good signal-to-noise ratio.

The last topic investigated in the frame of this research was the reflection of an incident plane wave due to a pure pressure traction at the surface traveling in a nonlinear material. Here, both a perfectly rigid and a perfectly stress-free boundary were analyzed. The main focus was on the second-harmonic term with linear dependency on the propagation distance. It is analytically and numerically shown that the amplitude of the particle velocity is linearly proportional to the accumulated propagation distance in the case of a rigid boundary, while it starts decreasing linearly after the reflection at a stress-free boundary. This effect may be interesting for experimental

measurements if the value of the amplitude mentioned is too small to be measured accurately – for example if the component under consideration is very thin. Then, one could think of an experimental setup where the incident wave is reflected several times at rigid boundaries so that the amplitude of this second-harmonic term is increased accordingly. Doing so would increase the signal-to-noise ratio and improve the quality of the measurement.

All investigations presented in this thesis were purely theoretical. Thus, it would be interesting to compare the results provided here to measured data obtained from appropriate experiments. However, this would clearly exceed the scope of this thesis; the corresponding experimental measurements are left for future work.

REFERENCES

- [1] ACHENBACH, J. D., *Wave Propagation in Elastic Solids*, vol. 16 of *Applied Mathematics and Mechanics*. Elsevier Science Publishers B.V., 1975.
- [2] BALBÁS, J. and TADMOR, E., “CENTPACK.” online at <http://www.cscamm.umd.edu/centpack/software>, July 2006. Available at: <http://www.cscamm.umd.edu/centpack/software>.
- [3] BUCK, O. and THOMPSON, D. O., “Relation of finite amplitude waves to third order elastic constants,” *Materials Science and Engineering*, vol. 1, pp. 117–140, 1966.
- [4] GODLEWSKI, E. and RAVIART, P. A., *Numerical Approximation of Hyperbolic Systems of Conservation Laws*, vol. 118 of *Applied Mathematical Sciences*. Springer, 1996.
- [5] HAMILTON, M. F. and BLACKSTOCK, D. T., *Nonlinear Acoustics*. Academic Press, 1998.
- [6] HERRMANN, J., KIM, J. Y., JACOBS, L. J., QU, J., LITTLES, J. W., and SAVAGE, M. F., “Assessment of material damage in a nickel-base superalloy using nonlinear rayleigh surface waves,” *Journal of Applied Physics*, vol. 99, p. 124913, 2006.
- [7] J. H. CANTRELL, J., “Acoustic-radiation stress in solids. i. theory,” *Physical Review B*, vol. 30, pp. 3214–3220, 1984.

- [8] J. H. CANTRELL, J. and YOST, W. T., “Nonlinear ultrasonic characterization of fatigue microstructures,” *International Journal of Fatigue*, vol. 23, pp. 487–490, 2001.
- [9] JACOB, X., TAKATSU, R., BARRIÈRE, C., and ROYER, D., “Experimental study of the acoustic radiation strain in solids,” *Applied Physics Letters*, vol. 88, p. 134111, 2006.
- [10] KIM, J. Y., JACOBS, L. J., QU, J., and LITTLES, J. W., “Experimental characterization of fatigue damage in a nickel-base superalloy using nonlinear ultrasonic waves,” *Journal of the Acoustical Society of America*, vol. 120, pp. 1266–1273, 2006.
- [11] KIM, J. Y., QU, J., JACOBS, L. J., LITTLES, J. W., and SAVAGE, M. F., “Acoustic nonlinearity parameter due to microplasticity,” *Journal of Nondestructive Evaluation*, vol. 25, pp. 29–36, 2006.
- [12] KÜCHLER, S., “Wave propagation in an elastic half-space with quadratic nonlinearity,” 2007.
- [13] KÜCHLER, S., “Two-dimensional wave propagation in an elastic half-space with quadratic nonlinearity - a numerical study,” *Journal of the Acoustical Society of America*, submitted.
- [14] KURGANOV, A. and TADMOR, E., “New high-resolution central schemes for nonlinear conservation laws and convection-diffusion equations,” *Journal of Computational Physics*, vol. 160, pp. 241–282, May 2000.
- [15] LAMB, H., “On the propagation of tremors over the surface of an elastic solid,” *Philosophical Transactions of the Royal Society of London*, vol. A 203, pp. 1–42, 1904.

- [16] MALVERN, L. E., *Introduction to the Mechanics of a Continuous Medium*. Series in Engineering of the Physical Sciences, Prentice-Hall, Inc., 1969.
- [17] MCCALL, K. R., "Theoretical study of nonlinear elastic wave propagation," *Journal of Geophysical Research*, vol. 99, pp. 2591–2600, 1994.
- [18] MEURER, T., QU, J., and JACOBS, L. J., "Wave propagation in nonlinear and hysteretic media - a numerical study," *International Journal of Solids and Structures*, vol. 39, pp. 5585–5614, 2002.
- [19] MIKLOWITZ, J., *The Theory of Elastic Waves and Waveguides*, vol. 22 of *Applied Mathematics and Mechanics*. Elsevier Science Publishers B.V., 1978.
- [20] NARASIMHA, K. T., KANNAN, E., and BALASUBRAMANIAM, K., "Simplified experimental technique to extract the acoustic radiation induced static strain in solids," *Applied Physics Letters*, vol. 91, p. 134103, 2007.
- [21] OPPENHEIM, A. V., SCHAFER, R. W., and BUCK, J. R., *Discrete-Time Signal Processing*. Prentice Hall International, Inc., 1999.
- [22] POLYAKOVA, A. L., "Nonlinear effects in a solid," *Soviet Physics - Solid State*, vol. 6, pp. 65–70, 1964.
- [23] SMITH, R. T., STERN, R., and STEPHENS, R. W. B., "Third-order elastic moduli of polycrystalline metals from ultrasonic velocity measurements," *Journal of the Acoustical Society of America*, vol. 40, pp. 1002–1008, 1966.
- [24] THURSTON, R. N. and SHAPIRO, M. J., "Interpretation of ultrasonic experiments on finite-amplitude waves," *Journal of the Acoustical Society of America*, vol. 41, pp. 1112–1125, 1966.
- [25] YOST, W. T. and J. H. CANTRELL, J., "Acoustic-radiation stress in solids. ii. experiment," *Physical Review B*, vol. 30, pp. 3221–3227, 1984.

- [26] ZAREMBO, L. K. and KRASILNIKOV, V. A., “Nonlinear phenomena in the propagation of elastic waves in solids,” *Soviet Physics Uspekhi*, vol. 13, pp. 778–797, 1971.